CONTROLLED FABRICATION OF 3D CARBON NANOTUBE ARCHITECTURES WITH IMPROVED FUNCTIONALITIES

SHARON LIM XIAODAI

(B. Sc. (Hons), NUS)

A THESIS SUBMITTED

FOR THE DEGREE OF MASTERS OF SCIENCE

DEPARTMENT OF PHYSICS

NATIONAL UNIVERSITY OF SINGAPORE

2009

CONTROLLED FABRICATION OF 3D CARBON NANOTUBE ARCHITECTURES WITH IMPROVED FUNCTIONALITIES

SHARON LIM XIAODAI

NATIONAL UNIVERSITY OF SINGAPORE

2009

Acknowledgements

For the past two years, life in the Nanomaterials Research Lab at the National University of Singapore had been extremely fun filling and exciting. Special thanks had to be given to my ever patient supervisor, Associate Professor Sow Chorng-Haur for his ample supply of crazy ideas and endless pool of optimism whenever I faced some bottlenecks in the area of research that I worked on. No matter where I would be in the future, I will be sure to take along with me this enriching and unforgettable experience.

Heartfelt gratitude must be given to Dr. Cheong Fook Chiong and Dr. Zhu Yanwu, for all their interesting suggestions, despite both being physically in the states. I would also like to thank my fellow lab mates, Dr. Binni Varghese, for all the advices given and for helping to take the TEM images. Sincere appreciation must also be given to Ms. Lena Lui, Ms. Foo Eng Tin, Mr. Xie Yilin, Mr. Chang Sheh Lit, Ms. Tao Ye, Mr. Zheng Minrui, Ms. Loh Pui Yee, Mr. Lee Kian Keat, Mr. Lim ZhiHan, Mr. Rajesh and Mr. Rajiv for all the help given and for making the lab a warm and homely place to work in. Appreciations must also be shown to all the lab technicians, from the Physics E-Lab, to the First, Second and Third Year Lab, and for all the help that I had received from the Physics Department workshop.

Last but not least, I would like to thank my husband, Guo Hao for his endless support and for always being there for me. I hereby dedicate this piece of work to you and my family.

Table of Contents

Chapter 2: Theoretical Background

Table of Contents

Chapter 3: Experimental Procedures

Chapter 4: Versatile Transfer of Aligned Carbon Nanotubes with Polydimethylsiloxane as the Intermediate

---

Chapter 5: Re-growth Aligned MWNTs with Improved Field Emission

Table of Contents

Chapter 6: Capillarity Assisted Assembly of CNTs Microstructures with Organized Initiations

Table of Contents

Abstract

In this work, a few techniques were developed. Among these techniques, a simple method to transfer aligned multi-walled carbon nanotubes (MWNTs) is demonstrated. With polydimethylsiloxane (PDMS) as the transfer medium, as-grown/patterned MWNT arrays are directly transferred onto a wide variety of platinum (Pt)-coated substrates at low temperatures. The transferred MWNTs show strong adhesion and good electric contact with the target substrates together with improved field emission performance. In addition, the substrates on which the initial batch of MWNTs was transferred from were used to re-grow another batch of MWNTs. These 2nd generations of MWNTs show ~ 2.6 times improvement in field enhancement factor and more uniform emissions. Such significant improvements are attributed to new emission sites comprising sharp carbonaceous impurities encompassing both tip and upper portion of the 2nd generation of MWNTs.

Using the transfer technique, studies on the effect of hydrostatic dilation stress to the formation of MWNT microstructures were investigated. By preventing interactions between the assembly solvent and the substrate; and embedding the MWNTs in the PDMS, no formations of MWNT polygons were observed on the pre-pattened MWNTs array. Using three different capillarity assisted techniques, large scale formations of non-transferred MWNT based micro-structures are created. Firstly, laser induced artificial vacancies in MWNT arrays served as initiation sites during water-driven formation of MWNT polygon network. The dependence of the structures formed on the size of the vacancies, the densities of the MWNTs and the surface properties of the MWNTs arrays are investigated. Secondly, organized

Abstract

MWNT pillars are crafted out of MWNT arrays and a small droplet of water was found to produce sufficient force to bring about deflections of the pillars towards each other, thereby allowing the formations of three-dimensional top-gathering MWNTs pillars. Lastly, a dip-dry method is introduced for large scale orienting and densification of MWNT micro-walls into micro-belts along the substrate. A 3.5 fold reduction in resistivity of the MWNT micro-walls was achieved. In addition to capillarity induced formations of large scale MWNT micro-structures, micro-structures, specifically micro-walls, were also found to bring about improvements in the hydrophobic nature of the MWNT surfaces.

List of Publications

[1] **Xiaodai Lim**, Hee Wei Gary Foo, Guo Hao Chia, Chorng-Haur Sow Capillarity Assisted Assembly of Carbon Nanotube Microstructures with Organized Initiations. Submitted to Advanced Functional Materials for publication. (2009)

[2] **Xiaodai Lim**, Yanwu Zhu, Binni Varghese, XingYu Gao, Andrew Thye Shen Wee, Chorng-Haur Sow. Re-Grown Aligned Carbon Nanotubes with Improved Field Emission. Submitted to Diamond and Related Materials for publication. (2009)

[3] Si Hong Lu, Ni Tun Ma Han, Zhiwei Joshua Mei, Guo Hao Chia, **Xiaodai Lim** and Chorng-Haur Sow. Improved Hydrophobicity of Carbon Nanotube Arrays with Micro-patterning. Accepted for publication in Langmuir. (2009)

[4] Raghavan Baby Rakhi, **Xiaodai Lim**, Xingyu Gao, Yuzhan Wang, Andrew Thye Shen Wee, Kanikrishnan Sethupathi, Sundara Ramaprabhu, Chorng Haur Sow. Electron field emission from magnetic nanowire materials encapsulated multi-walled carbon nanotubes. Accepted for publication in Applied Physics A. (2009)

[5] Yanwu Zhu, **Xiaodai Lim**, Mong Chea Sim, Chwee Teck Lim, Chorng Haur Sow. Versatile Transfer of Aligned Carbon Nanotubes with Polydimethylsiloxane as the Intermediate. Nanotechnology, 19, 325304 (2008)

List of Papers Presented at Conferences

[1] **X. Lim**, C. H. Sow *et al.* ICMAT & IUMRS-ICA 2009. Singapore. (28 June – 3 July 2009) – Oral presentation

[2] **X. Lim**, C. H. Sow *et al.* New Diamond and Nano Carbons Conference 2009. Traverse City, Michigan, USA. (7-11 June 2009) – Oral presentation

[3] **X. Lim**, C. H. Sow *et al.* The 2008 Asian Conference on Nanoscience and Nanotechnology. Singapore. (3-7 Nov 2008) – Poster presentation

[4] **X. Lim**, C. H. Sow *et al.* 3rd Mathematics and Physical Science Graduate Congress. Kuala Lumpur, Malaysia. (12-14 Dec 2007) – Poster presentation

[5] **X. Lim**, C. H. Sow *et al.* International Conference on Materials for Advanced Technologies. Singapore. (1-6 July 2007) – Oral presentation

[6] **X. Lim**, C. H. Sow *et al.* International Conference on Nanoscience and Technology. Beijing, China. (June 4-6 2007) – Oral presentation

List of Figures

List of Figures

List of Figures

List of Figures

List of Figures

List of Figures

Chapter 1: Introduction

Quasi-one dimensional carbon nanotubes (CNTs) discovered by Sumio Iijima[1] in 1991 opened the passage way into a new area in the regime of carbon research. Since its discovery, many researchers have been captivated by their outstanding unique optical, electrical and mechanical properties.[2-5] Among these properties, the hydrophobic nature of the CNT surfaces, together with its potential applications in electronic devices and effective field emitting properties captured our attention.

Being an ideal candidate for field emitting and nanoelectronic devices,[6] CNTs have been readily synthesized via laser ablation, arc discharge and chemical vapor deposition (CVD).[7] Amongst them, CVD is the favored method for the large scale fabrication of aligned CNT arrays. The catalytic based CVD growth of CNTs mainly involves a three-step process: nucleation, growth and termination. During nucleation, the heated (700 ^{o}C – 800 ^{o}C) transition-metal thin film coalesces into nanoparticles[12] which seed the subsequent growth process. At the same time, gaseous hydrocarbons are dissociated and absorbed into the catalyst nanoparticles. Once the catalyst nanoparticle becomes saturated with carbon, CNT growth begins. As the fullerene cap extends from the nanoclusters, the side walls starts to form, leading to the formation of CNTs. The final termination of CNT growth is attributed to two causes, namely, termination of carbon source or formation of amorphous carbon barrier around the catalysts. Thus, good control of the CNT growth is determined by the "activity" of the catalysts.[13] With large scale production of aligned CNTs becoming feasible through the CVD synthesis method, opportunities to study the use of CNTs in field emission displays and vertical interconnects were created.

However, because conventional CVD growth involves high temperatures (600-1200°C), and a buffer layer usually needed to ensure the function of the catalyst, the substrates have for years been limited to high-melting point semiconductors (e.g. Si) or insulators (e.g. quartz). It was not until recently, that growth of aligned CNTs on metallic substrates via CVD was reported[8] and solution-based CNTs synthesized at low temperature on plastic substrates.[9, 10] To fabricate CNTs on other desired substrates, printing techniques such as screen printing,[11, 12] dip coating,[13] and inkjet printing[14-16] have shown potential in fabricating CNT based flexible devices. However, CNTs fabricated from these printing methods usually exhibit randomly aligned morphology. In order to maintain the alignment of CNT arrays, a few methods have been developed to transfer CNTs onto desired substrates. For example, Zhang *et al.*[17] and Chai *et al.*[18] reported transfer of free-standing CNT films onto Cu substrates after a lift-up of SiO_2/Si by HF etching. Utilizing eutectic metals (Sn/Pb or Sn/Au) with low-melting points as solders, aligned CNTs were transferred onto metal substrates by Zhu *et al.*[19] and Kumar *et al.*[20] In this technique, open-ended CNTs showed better efficiency due to their proper wetting with metals.[19] Using similar principles, a hot embossing technique was used to transfer patterned CNTs onto polymer substrates.[21] To improve the conductivity, a conductive polymer composite was used to transfer CNT films onto a Cu surface.[22] In order to create a wide range of CNT based devices, the development of a versatile transfer technique with many attributes is desirable. These attributes include simple and low temperature processes, substrate friendliness, strong adhesion and satisfactory electrical contact.

Upon removal of the initial batch of CNTs from the initial substrate on which they were synthesized, recent report by Chiu *et al.*[23] shows that they were able to grow high-purity single walled carbon nanotubes (SWNTs) after a few cycles of repeated growth process using the same catalytic layer on SiO_2/Si substrate. Their work was a result of the separation of catalytic particles into two parts during growth: one at the tip, while the other remained at the base of the CNTs. Upon removal of CNTs, the remaining smaller sized catalytic particles would be able to facilitate growth of CNTs without additional catalytic particles. Since it is well known that the diameter of CNTs is dependent on the size of the catalytic particles, having smaller catalytic particles remaining on the substrates would naturally yield CNTs with smaller diameters that eventually lead to the growth of SWNTs after a few cycles of repeated growth process. In order to achieve their aim, Chiu *et al.*[23] annealed the CNTs in an attempt to remove the original batch of CNTs and free up the catalytic particles for the next cycle of growth. The thermal annealing process would also remove any amorphous carbon surrounding the catalytic particles and activate the catalyst. Using a similar idea of re-growing CNTs but without removal of the original batch of CNTs, Crouse *et al.*[24] reported that catalysts, which were inactive toward nucleation of CNTs during the initial growth of CNTs, were capable of becoming active when subjected to re-growth under identical growth conditions. As such, it would be both interesting and economically desirable to determine if CNTs with improved quality could be re-grown on the same substrate using the same catalysts after undergoing the transfer process.

In addition to the development of new techniques to facilitate the implementations of CNTs for electronic applications, while ensuring the economic viability of implementing these techniques, material fabrications are progressing into a phase, where well-defined structures created using nanoscale materials becomes a key technology. To facilitate such progress, self-assembly is an efficient and often preferred process to build micro- and nanoparticles into ordered macroscopic structures. As such, it is essential to be able to control the architecture of the CNTs on the substrates since such controlled assembly is crucial for applications in electrode, micromechanical actuators and composites.[7] The structures at which the CNTs are defined can be divided into negative (CNTs are removed to form the pattern) and positive (where CNTs remained as the building block of the pattern) structures.

Chakrapani *et al.*[25] and Liu *et al.*[26] reported on the use of long range capillary effect of water to assist the assembly of CNTs into desired negative structures. To do so, both groups introduced artificial vacant sites into as-grown vertically aligned CNT arrays. Once water was introduced to the system, it would be guided into the spaces between the CNTs. The resulting capillary action forces the water to reach and spreads across the hydrophilic substrates (silicon/quartz), creating a hydrostatic dilation stress. The presence of the hydrostatic stress caused the CNTs to be flattened in the lower density regions while allowing the CNTs to become tightly packed along the high density regions.[26]

While both groups used similar water assisted-assembly technique, different treatments were carried out on the CNT samples before the assembly process. During their sample preparation process, Chakrapani *et al.*[25] reported the use of pre-process technique of patterning the substrate on which the vertically aligned CNTs were synthesized to create the vacant sites. Due to the hydrophobic nature of the CNT surfaces, the CNTs were oxidized before the introduction of water. For the case of Liu *et al.*[26], post synthesis treatment of using pulse laser to create vacant sites on the CNTs was carried out and no oxidization of the CNT arrays was carried out.

In the case of positive CNT structures, a method of pre-patterning the substrate[25, 27] was implemented. Work published by Wei *et al.*[27] reported on the ability to arrange CNTs in an organized manner through patterning SiO_2 on Si substrate. In doing so, they are able to produce simultaneous and multidirectional nanotube growth. With well-defined three dimensional (3D) CNT structures having great potential as packing systems and CNT based electronics, it would thus be useful to have a technique that facilitates well defined creations of 3D CNT structures and large scale creation of such structures in a cost efficient manner. In addition, large scale assembly of CNTs into well packed and organized strips along the surfaces of the substrates could potentially be used in the creation of suspended and stretched nanotubes. In turn, these CNTs could potentially be implemented as nanoscale electro-mechanical sensing components.[28]

Over and above, CNTs not only exhibit potential in electronic applications, they also possess an interesting intrinsic superhydrophobic property. Motivated by nature's ability to create super-hydrophobic surfaces such as the lotus leaf[29] and the water strider,[30] many researches have been conducted with the aim of re-creating such surfaces for use in areas such as anti-sticking of snow on various surfaces[31] to antibiofouling paints for boats[32]. Using contact angle (CA, α), the angle between the surface and the water meniscus near the line of contact (measured through a droplet), as an indicator of the wettability of the surface, a surface is deemed to be hydrophobic if α has a value $90^o \leq \alpha < 150^o$ [33]or super-hydrophobic if $\alpha > 150^o$.[34]

While the basic idea of superhydrophobicity had been developed by Young, Wenzel and Cassie and Baxter decades ago, it is the publication by Onda *et al.*[35] presenting both theoretical and experimental results on the wettability of fractal surfaces that marked the start of an explosion in the number of articles published in this topic.[36] In recent years, different techniques were developed to create hydrophobic surfaces. The range of techniques include mimicking and using biological structures as templates,[37] chemical functionalizations of surface[31] and physical modifications.[38] In the area of physical modification, both top-down and/or bottom-up approaches have been utilized for the fabrications of roughness on either intrinsic hydrophobic materials or coating the rough surfaces with a hydrophobic layer.[36]

Recently, Bhushan *et al.*[39] conducted an analysis of how hierarchical roughness was used to optimize biomimetic superhydrophobic surfaces. From their analysis, they proposed that one of the important factors for optimized roughness distribution on water repellent surface was that the asperities at each scale level should have small-width and large distance between them, i.e. a small value for the spacing factor, S_f, where the value of S_f was defined as the ratio of the width of the asperities to the distance between them. However, this requirement was limited by some critical value of S_f, providing the structures were able to support the weight of the water droplet. Using samples comprising asperities and valleys made of single-crystal silicon (Si), coated with hydrophobic 1,1,-2,2,-tetrahydroperfluorodecyltrichlorosilane (PF_3) self-assembled monolayer, the critical value was found to be $0.083 < S_f < 0.111$.[40] While many materials such as PDMS[41] and silicon[42, 43] have been widely used in the study of roughness on hydrophobic effect, one other interesting material to study such phenomenon is carbon nanotubes.

With intrinsic hydrophobic properties and nano-scale surface roughness, CNTs show great potential in applications such as self-cleaning surfaces. By a bottom-up approach, Lin *et al.*[29] reported the improved intrinsic hydrophobic nature of aligned CNTs by growing them into similar structures mimicking those found on lotus leaves. Another piece of work via bottom-up approach was presented by Li *et al.*,[29] where improvement of the hydrohobicity of aligned CNTs was achieved through the growth of honey-comb patterned aligned CNTs by pyrolysis of iron phthalocyanine. Such surfaces were found to exhibit a CA of 163.4 ± 1.4°. Applying similar approach, Zhang *et al.*[44] recently showcased their creations of superhydrophobic surfaces made up of SWNT pillars. With previous studies on superhydrophobic systems highlighting the importance of both micro- and nano-scale roughness in the formation of such surfaces, double structural roughness of the surface were formed. The nano-scaled roughness was induced by the intertwined SWNTs at the top of the pillars while SWNT pillars grown on nanosphere templated substrate constituted to roughness at the micro-scale level.

In the case of top-down approaches, Huang *et al.*[45] and Cho *et al.*[46] modified surfaces of CNTs to improve the intrinsic hydrophobicity of the material. By coating a layer of zinc oxide (ZnO) thin film on CNT arrays, Huang *et al.* created stable superhydrophobic surfaces. With alternation of ultraviolet (UV) radiation and dark storage, a reversible change in the wettability of the hybrid system from being superhydrophobic to hydrophilic was achieved. Replacing the coating material, Cho *et al.* coated Tetrafluoromethane (CF_4) onto CNT surfaces via glow discharge plasma at low pressure. They observed that the treated CNTs remained floating on water for several months due to drastic reduction of the surface free energy of the plasma-treated CNTs from 27.04 mN m^{-1} to 1.32 x 10^{-7} mN m^{-1}. Using a combination of both top-down and bottom-up approaches, Sun *et al.*[47] have demonstrated the preparation of super-hydrophobic anisotropic aligned CNT film by chemical vapour deposition (CVD) on silicon substrates with quadrate micro-pillar arrays prepared by photo-lithography. By varying the spacing between the micro-pillars of height 10 μm, they were able to observe both hydrophobic and hydrophilic surfaces. However, with the introduction of fluorinated SAM of (2-(perfluoroctyl)ethyl)trimethoxysilane, such space dependent wetting properties were no longer observed.

Through their work on simulation, Varnik *et al.*[48] reported their findings on scaling effects in micro-scale fluid flows at rough solid surfaces. It was determined from their work that flow instability was not controlled by Reynolds number alone. Rather, surface roughness/channel geometry provided a new route for tuning qualitative features of the flow. By varying distances between the obstacles, fluid flows were observed to switch between stable and instability flows. Although their work was based on the study of fluid flow, the idea of a possible existence of optimum choice of distance between the obstacles was a source of motivation to carry out a combination of top-down and bottom-up approaches in the investigation of the wettability of aligned CNTs with micro-patterns.

This project is divided into three parts. Firstly, to allow wider applications of CNTs in electronic devices, a transfer technique using polydimethylsiloxane (PDMS) as intermediate was developed. With this technique, aligned CNTs could easily be transferred onto a wide variety of flexible substrates ranging from cloth, transparency to glass substrates. With CNTs being determined to be a potential candidate in field emission applications, field emission studies on both pre- and post-transferred CNTs were conducted. The results showed that due to reasons associated with better alignment and open-end CNTs, together with good electrical contact with the platinum coated substrates, transferred CNTs exhibited better field enhancement properties. Such enhancement in the field emission effect of CNTs were also observed when the substrates used in synthesizing the initial batch of CNTs were re-used to grow a second batch of CNTs using the same catalysts.

In the second part of this work, three different techniques allow well-controlled assemblies of CNTs into large scale negative (CNTs are removed to form the structures), positive (CNTs remained as the building blocks for the formation of the micro-structures) and micro-belts structures. To facilitate the formations of negative CNTs micro-structures, artificial vacancies were introduced into the CNT arrays by focused laser beam pruning before water was introduced as the agent that assisted the assemblies of CNTs. These artificial sites serving as low density regions allowed the formation of hydrostatic dilation stress when water encounters a hydrophilic substrate. With tailored patterning, water-assisted assemblies of top-gathering CNT micro-pillars were achieved. In another experiment, using ethanol as the assembling agent, CNT micro-walls were collapsed over quartz substrates and formed micro-belts. Current-voltage (I-V) measurements of these high density CNT micro-belts resulted in a reduction in resistivity by 3.5 fold.

In the final part of the project, a micro-patterning process was used to improve the hydrophobic nature of the CNTs surfaces. To do so, a focused laser beam was used to create micro-walls on the CNT arrays. These micro-walls, serving as added roughness to the surface of the CNTs, resulted in an improvement in the hydrophobicity of the CNT surfaces. The technique thus provided a viable route for further developments in the creation of water repelling patterned CNTs surfaces.

This thesis is organized as follows. In the following chapter, some background information of CNTs and their classification will be provided. We will also present some theories with respect to wetting action on solid surfaces and field emission. Chapter 3 includes detailed descriptions on the synthesis process of the CNTs used in this work. Descriptions of the experimental setup used in analyzing the samples prepared in this work would also be introduced.

In Chapter 4, detailed experimental results and discussion pertaining to the development of a technique of transferring CNTs would be detailed. Following which, studies conducted on the properties of CNTs re-grown from recycled substrate and field emission properties of the re-grown CNTs would be presented in Chapter 5. Subsequently, techniques developed and studies conducted with respect to capillarity assisted assembly of CNTs into different forms of microstructures with organized initiations would be presented in Chapter 6. In Chapter 7, improved wettability of CNTs was achieved through micro-patterning via a laser pruning technique. Lastly, in Chapter 8, the thesis would conclude with a summary comprising all results obtained from the series of experiments conducted.

References

1. Iijima, S., *Nature* **1991,** *354* (6348), 56-58.
2. Wildoer, J. W. G.; Venema, L. C.; Rinzler, A. G.; Smalley, R. E.; Dekker, C., *Nature* **1998,** *391* (6662), 59-62.
3. Treacy, M. M. J.; Ebbesen, T. W.; Gibson, J. M., *Nature* **1996,** *381* (6584), 678-680.
4. Tekleab, D.; Czerw, R.; Carroll, D. L.; Ajayan, P. M., *Applied Physics Letters* **2000,** *76* (24), 3594-3596.
5. Jang, J. W.; Lee, D. K.; Lee, C. E.; Lee, T. J.; Lee, C. J.; Noh, S. J., *Solid State Communications* **2002,** *122* (11), 619-622.
6. Avouris, P., *Chem. Phys.* **2002,** *281*, 429.
7. Dresselhaus, M. S.; Dresselhaus, G.; Avouris, P., *Carbon Nanotubes*. Springer: Berlin, 2001.
8. Talapatra, S.; Kar, S.; Pal, S. K.; Vajtai, R.; Ci, L.; Victor, P.; Shaijumon, M. M.; S. Kaur; Nalamasu, O.; Ajayan, P. M., *Nature Nanotechnology* **2006,** *1*, 112.
9. Hofmann, S.; Ducati, C.; Kleinsorge, B.; Robertson, J., *Appl. Phys. Lett.* **2003,** *83*, 4661.
10. Choi, J. H.; Park, J. H.; Moon, J. S., *Diamond Relat. Mater.* **2006,** *15*, 44.
11. Talin, A. A.; Dean, K. A.; Jaskie, J. E., *Solid-State Electron.* **2001,** *45*, 963.
12. Saito, Y.; Uemura, S., *Carbon* **2000,** *38*, 169.
13. Spotnitz, M. E.; Ryan, D.; Stone, H. A., *J. Mater. Chem.* **2004,** *14*, 1299.
14. Kordas, K.; Mustonen, T.; Toth, G.; Jantunen, H.; Lajunen, M.; Soldano, C.; Talapatra, S.; Kar, S.; Vajtai, R.; Ajayan, P. M., *Small* **2006,** *2*, 1021.

15. Park, J. U.; Hardy, M.; Kang, S. J.; Barton, K.; Adair, K.; Mukhopadhyay, D. K.; Lee, C. Y.; Strano, M. S.; Alleyne, A. G.; Georgiadis, J. G.; Ferreira, P. M.; Rogers, J. A., *Nat. Mater.* **2007,** *6*, 782.
16. Lyth, S. M.; Silva, S. R. P., *Appl. Phys. Lett.* **2007,** *90*, 173124.
17. Zhang, G.; Mann, D.; Zhang, L.; Javey, A.; Li, Y.; Yenilmez, E.; Wang, Q.; McVittie, J. P.; Nishi, Y.; Gibbons, J.; Dai, H., *Proc. Natl. Acad. Sci. USA* **2005,** *102*, 16141.
18. Chai, Y.; Gong, J.; Zhang, K.; Chan, P. C. H.; Yuen, M. M. F., *Nanotechnology* **2007,** *18*, 355709.
19. Zhu, L.; Sun, Y.; Hess, D. W.; Wong, C.-P., *Nano Lett.* **2006,** *6*, 243.
20. Kumar, A.; Pushparaj, V. L.; Kar, S.; Nalamasu, O.; Ajayan, P. M., *Appl. Phys. Lett.* **2006,** *89*, 163120.
21. Allen, A. C.; Sunden, E.; Cannon, A.; Graham, S.; King, W., *Appl. Phys. Lett.* **2006,** *88*, 083112.
22. Jiang, H.; Zhu, L.; Moon, K.-s.; Wong, C. P., *Nanotechnology* **2007,** *18*, 125203.
23. Chiu, C. C.; Yoshimura, M.; Ueda, K., *Japanese Journal of Applied Physics* **2008,** *47* (4), 1952-1955.
24. Crouse, C. A.; Maruyama, B.; Colorado, R.; Back, T.; Barron, A. R., *Journal of the American Chemical Society* **2008,** *130* (25), 7946-7954.
25. Chakrapani, N.; Wei, B. Q.; Carrillo, A.; Ajayan, P. M.; Kane, R. S., *Proceedings of the National Academy of Sciences of the United States of America* **2004,** *101* (12), 4009-4012.
26. Liu, H.; Li, S. H.; Zhai, J.; Li, H. J.; Zheng, Q. S.; Jiang, L.; Zhu, D. B., *Angewandte Chemie-International Edition* **2004,** *43* (9), 1146-1149.

27. Wei, B. Q.; Vajtai, R.; Jung, Y.; Ward, J.; Zhang, R.; Ramanath, G.; Ajayan, P. M., *Nature* **2002,** *416* (6880), 495-496.

28. Lee, B. Y.; Heo, K.; Bak, J. H.; Cho, S. U.; Moon, S.; Park, Y. D.; Hong, S., *Nano Lett.* **2008,** *8* (12), 4483-4487.

29. Feng, L.; Li, S. H.; Li, Y. S.; Li, H. J.; Zhang, L. J.; Zhai, J.; Song, Y. L.; Liu, B. Q.; Jiang, L.; Zhu, D. B., *Advanced Materials* **2002,** *14* (24), 1857-1860.

30. Gao, X.; Jiang, L., *Nature* **2004,** *432*, 36.

31. Kako, T.; Nakajima, A.; Irie, H.; Kato, Z.; Uematsu, K.; Watanabe, T.; Hashimoto, K., *J. Mater. Sci.* **2004,** *39* (2), 547-555.

32. Scardino, A.; De Nys, R.; Ison, O.; O'Connor, W.; Steinberg, P. In *Microtopography and antifouling properties of the shell surface of the bivalve molluscs Mytilus galloprovincialis and Pinctada imbricata*, 11th International Congress on Marine Corrosion and Fouling, San Diego, California, Jul; San Diego, California, 2002; pp 221-230.

33. Burton, Z.; Bhushan, B., *Nano Letters* **2005,** *5* (8), 1607-1613.

34. Sun, T. L.; Wang, G. J.; Feng, L.; Liu, B. Q.; Ma, Y. M.; Jiang, L.; Zhu, D. B., *Angewandte Chemie-International Edition* **2004,** *43* (3), 357-360.

35. Onda, T.; Shibuichi, S.; Satoh, N.; Tsujii, K., *Langmuir* **1996,** *12* (9), 2125-2127.

36. Roach, P.; Shirtcliffe, N. J.; Newton, M. I., *Soft Matter* **2008,** *4* (2), 224-240.

37. Sun, M. H.; Luo, C. X.; Xu, L. P.; Ji, H.; Qi, O. Y.; Yu, D. P.; Chen, Y., *Langmuir* **2005,** *21* (19), 8978-8981.

38. Zheng, Q. S.; Yu, Y.; Zhao, Z. H., *Langmuir* **2005,** *21* (26), 12207-12212.

39. Nosonovsky, M.; Bhushan, B. In *Hierarchical roughness optimization for biomimetic superhydrophobic surfaces*, 8th International Conference on Scanning Probe Microscopy, Sensors and Nanostructures, Montpellier, FRANCE, Jun 03-06; Montpellier, FRANCE, 2006; pp 969-979.

40. Bhushan, B.; Nosonovsky, M.; Jung, Y. C., *Journal of the Royal Society Interface* **2007,** *4* (15), 643-648.

41. Chen, Y.; He, B.; Lee, J. H.; Patankar, N. A., *Journal of Colloid and Interface Science* **2005,** *281* (2), 458-464.

42. Oner, D.; McCarthy, T. J., *Langmuir* **2000,** *16* (20), 7777-7782.

43. Zhu, L.; Feng, Y. Y.; Ye, X. Y.; Zhou, Z. Y. In *Tuning wettability and getting superhydrophobic surface by controlling surface roughness with well-designed microstructures*, 13th International Conference on Solid-State Sensors, Actuators and Microsystems, Seoul, SOUTH KOREA, Jun 05-09; Seoul, SOUTH KOREA, 2005; pp 595-600.

44. Zhang, L.; Resasco, D. E., *Langmuir* **2009,** *25* (8), 4792-4798.

45. Huang, L.; Lau, S. P.; Yang, H. Y.; Leong, E. S. P.; Yu, S. F.; Prawer, S., *Journal of Physical Chemistry B* **2005,** *109* (16), 7746-7748.

46. Cho, S. C.; Hong, Y. C.; Uhm, H. S., *J. Mater. Chem.* **2007,** *17* (3), 232-237.

47. Sun, T.; Wang, G. J.; Liu, H.; Feng, L.; Jiang, L.; Zhu, D. B., *Journal of the American Chemical Society* **2003,** *125* (49), 14996-14997.

48. Varnik, F.; Raabe, D., *Model. Simul. Mater. Sci. Eng.* **2006,** *14* (5), 857-873.

Chapter 2: Theoretical Background

2.1 Introduction

In this chapter, we will first provide some historical perspective on the development of carbon nanotubes (CNTs) before addressing the properties of CNTs. Information regarding the types of carbon nanotubes available would also be discussed with emphasis being placed on properties of multi-walled carbon nanotubes (MWNTs), which were utilized in all work presented in this thesis. Elaborations on the wetting behaviors of liquid and solid surface will be mentioned and we will show how theories such as Wenzel Equation and Cassie's Law can be used for measurement of wetting behavior of solid surfaces. In addition, a summary of the theory behind the field emission phenomenon would also be presented.

2.2 Carbon Nanotubes (CNTs)

2.2.1 A Brief History

Walking through the historical path to the discovery of CNTs, scientists started working with the macroscopic analogy of CNTs, Carbon Fibers, both in the 19th century and more recently after World War II. In the 1970-80's the synthesis of vapor grown carbon fibers by the decomposition of hydrocarbons together with transitional catalyst dust at high temperature yielded carbon filaments of very small diameter (< 10 nm). However, not much emphasis was being placed in the studies of such thin filaments.[1] It was not until 1991 when Iijima[2] of the NEC Laboratory in Tsukuba, Japan concluded the existence of novel graphitic structures, another new form of carbon similar to tiny tubules of graphite presumably closed at each ends, that sparked off enthusiastic research in the CNT field.

2.2.2 Definition of Carbon Nanotubes

CNTs can be visualized by simply downsizing the size of a human hair by 10 000 times. In doing so, one would be able to visualize both the size and shape of the nanotubes. These nanotubes are honeycomb lattice of the graphite sheet being rolled into cylindrical form with two ends of fullerene-like caps or hemispheres. The diameter of a single CNT is of nanometer scale and the length of each tube is usually more than 1 μm. Thus implying that CNT, neglecting the two end caps, has large length to diameter ratio (as large as $10^4 - 10^5$).[1] With respect to the number of dimensions less than 100 nm, nanostructures can be classified into two dimensional (2D, nanofilm), 1D (nanotube or nanowire), and 0D (nanoparticles) structures. With CNTs having such high aspect ratios, they can thus be considered as 1D nanostructure, which experiences confinement in two other directions perpendicular to the longitudinal direction. Due to a combination of both quantum confinement in the nanoscaled dimensions and the bulk properties in the other dimensions, a host of interesting properties such as optical, electrical and mechanical properties[3-6] could be expected from the CNTs. Thereby creating a wide range of potential applications.

2.2.3 Classifications of Carbon Nanotubes

Based on the types of CNTs observed, they are generally being classified into two categories, namely the Single-wall Carbon Nanotubes (SWNTs) and the Multi-wall Carbon Nanotubes (MWNTs).

The SWNT is one atom in wall thickness and tens of atoms around the circumference. As such, the SWNT can be considered as the fundamental building block of CNTs. In other words, MWNT is made up of many concentric layers of SWNT, with smaller SWNT surrounded by larger ones. Typically, a SWNT has a diameter range of 0.7 nm to ~ 10 nm although most of the observed SWNTs have diameter > 2 nm.[1] Clearly, diameters of MWNTs are much larger than those of SWNTs, from a few nanometers to 500 nm, and the length of MWNTs can be up to 200 μm. Like graphite, bonding between the carbon atoms of the SWNT and MWNT involves three neighbors and their hybridization is expected to be sp^2 like.

Structures of CNTs depend on different orientations of the six-membered carbon ring (hexagon) in the honeycomb lattice relative to the axis of the nanotubes. The direction of the hexagon in the honeycomb lattice relative to the axis of the CNTs orients almost arbitrarily without any distortion to the hexagons, except near the curvature joining the end caps to the tube. As a result, CNTs can take up many different structures although their basic shape remains cylindrical. As such, metallic and semi-conducting properties of the CNTs are also dependent on way in which the graphite sheets were rolled up (Figure 2.1). That is, when integer $n = m$, these CNTs are termed armchair and they are metallic. When either n or $m = 0$, the CNTs are called Zigzag and CNTs with any other values for integer n and m are classified as Chiral. For CNTs to exhibit semi-conducting properties with small band gap, n – m = 3k where k is a nonzero integer. Any remaining CNTs whose relation between both n and m integer fell out of those listed would exhibit semi-conducting properties with the band gap having an inverse relation to the nanotube diameter.[7, 8]

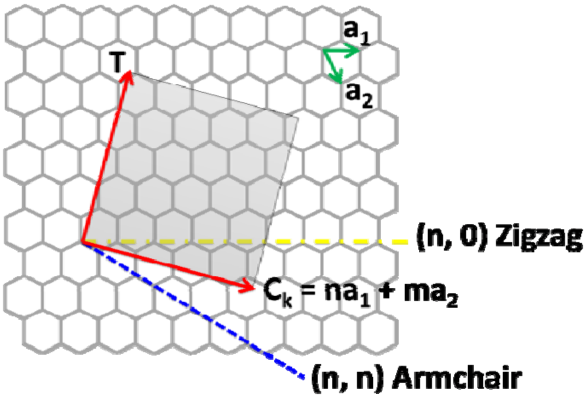

Figure 2.1 Schematic of how CNTs are classified based on the direction in which the graphite sheet is being rolled up. **T** denotes the tube axis, and $\mathbf{a}_1$ and $\mathbf{a}_2$ are the unit vectors of graphene in real space.

2.3 Properties of Multi-walled Carbon Nanotubes

As mentioned in the previous section, electrical properties of CNTs are dependent on the orientation in which the graphite sheets were rolled up. With common techniques such as arc discharge, laser deposition and chemical vapour deposition for the growth of CNTs, prefect control over the chirality of the CNTs is difficult to achieve. Generally, a single growth process would generate a mixture of metallic and semi-conductor type CNTs. While separation of CNTs, in the case of SWNTs, is possible after undergoing a subsequent treatment procedure like the dielectrophoresis technique,[9] such procedure has yet to achieve scalability and the process of re-depositing the separated CNTs may pose a new set of problems altogether.[10] On the other hand, MWNT which exhibit general metallic properties due to larger diameter and high number of conducting shells, turn out to be an interesting subject for applications in electronic interconnects.

2.3.1 Electrical Properties of Multi-walled Carbon Nanotubes

In the studies of electrical transport, the first signature of quantum effects was found in the magnetoresistance (MR) of MWNTs.[11] Based on work carried out by Song *et al.*[12] and Langer *et al.*,[13] both groups observed the presence of negative magnetoresistance at low temperature. This conclusion was consistent despite studies being conducted on bundled MWNTs (Song *et al.*) and single MWNT (Langer *et al.*), respectively. Their result was indicative of the existence of weak localization and the phase coherent length that was determined to be < 20nm at 0.3 K. With further work presented on the observation of Aharonov-Bohm resistance oscillation in MWNTs,[14] it provided a convincing proof that the electric current flows in the outermost (metallic) tube, at a temperature lesser than 70 K. However, this outcome was presumably attributed to the way in which the MWNTs were contacted. Through experimenting different ways of establishing contacts, electrical transport in MWNTs was determined to be ballistic over a distance on the order larger than 1 μm at room temperature.[11] As such, electrons within the nanotubes would be able to move without resistance. Thereby, allowing MWNTs to exhibit outstanding electrical properties: high current carrying capacity, huge thermal conductivity and length independent resistance over a length of 2.5 μm.[15] Such unique properties of MWNTs could be effectively harvested when closely packed nanotubes bundles, which are expected to have higher conductivity than copper, are introduced into integrated circuits (IC).[16]

2.3.2 Field Emission Properties of Multi-walled Carbon Nanotubes

In 1995, several groups of researchers found that CNTs turns out to be excellent electron field emitters, with low turn-on field and high emission current densities.[17, 18] Field emission is a phenomenon observed when electrons tunnel through the metallic sample into vacuum under the application of a strong electric field. To date, field emission properties of CNTs were believed to be independent of type of nanotubes used, namely, SWNTs or MWNTs. While different factors such as vacuum level and morphologies of the CNTs surfaces resulted in a range of experimental results reported on CNTs, the typical turn-on field (at 10 μA/cm^2) and threshold field (at 10 mA/cm^2) were reported to have values of 1 and 6 V/μm respectively.[19] Detailed studies[20] conducted by applying similar experimental parameters to both open and closed tip single MWNT strains show that the turn-on voltage was considerably higher for open tip MWNT. The result thus suggested that the localized states at the dome-shaped tip of the MWNT played an important role in the field emission process observed. In addition, systematic deviations from the Fowler-Nordheim[21] model for field emission could be observed at high emission currents, which suggested that electrons were emitted from well-defined energy levels and this corresponds to localized states at the tip of the nanotubes.[11] With electrons being emitted from the tip of the nanotube, field emission properties of the nanotubes could easily be affected by the tip geometry. This thus implies that in the case of field emission from aligned arrays of MWNTs studied in this work, screening effect due to electrostatic screening between adjacent emitters would have to be taken into consideration.

2.3.3 Wettability of Multi-walled Carbon Nanotubes

With wettability of a solid surface playing an important role for many practical applications, large emphasis had been placed in search for surfaces that are superhydrophobic, with contact angle (CA) greater than 150^o. In the natural world, many of such surfaces had been identified, with the lotus leaf (Figure 2.2) being one of the most famous examples. With a surface comprising of both micro- and nano-scale roughness, the water CA of a lotus leaf was found to be about 160^o.[22] In the midst of creating such superhydrophobic surfaces, MWNTs with their inherent hydrophobic wetting surfaces have gained vast amount of attention in this field of research. Through the use of various methods ranging from chemical functionalizations using CF_4[23] to patterning of the catalyst on which the MWNTs were synthesized, surface wettability of MWNTs[24] had been improved from hydrophobic to being superhydrophobic.

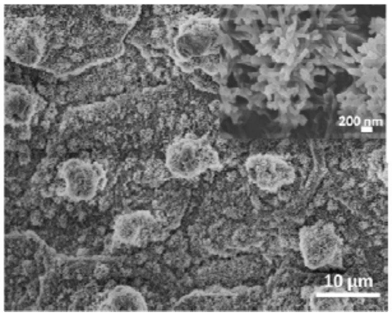

Figure 2.2 SEM image of the surface morphology of a lotus leaf showing both micro- and nano-scale roughness. Insert is a high magnification of the nano-scale roughness covering each microrelief.

2.4 Wetting Action at Solid Surfaces

Following the above discussions on the wettability of MWNTs surfaces, a brief description of a few theories developed for better understanding of the wetting behavior of surfaces is summarized in this section. Wetting of a solid surface almost always involves three different interfacial boundary surfaces, namely, solid – air (free solid), solid – liquid and liquid – air (free liquid) interface. During the process of wetting, solid – air interface would be replaced with equal area of solid – liquid interface together with an additional liquid – air interface.

Interactions between these three interfaces would no doubt be dependent on various experimental conditions such as dryness of air, surface morphology etc. As each interface has its own specific energy content, wetting with its accompanying change in the extent of each interface, will result in variations to the net specific energy content of the system. Hence, wetting is considered as a thermodynamic process and magnitude of the free energy change involved would determine whether the wetting process is spontaneous.

Given an experimental condition and assuming that we have a case of water droplet spreading across a perfectly smooth solid surface (i.e. equilibrium has yet to be achieved), the specific energy content of the solid surface will in general, be different for the wetted area under the droplet than for the dry area outside the droplet. Given the above situation, it is thus reasonable to assume that the wetted area has lower specific energy to bring about spontaneous spreading of the droplet.

As spreading occurs, both wetted area under the droplet and the free liquid surface over it would thereby increase. The former involves release of energy while the latter a consumption of energy. Difference in these energies would be the one that determines wetting characteristics of the solid.[25]

2.4.1 Contact Angle Measurement

When a droplet of liquid is placed on a solid surface, it may remain as a drop of finite area, or it may spread indefinitely over the surface. Contact Angle (CA), α is a measurement that helps us to determine and thus define whether a surface is superhydrophobic ($\alpha \geq 150°$),[26] hydrophobic ($90° \leq \alpha < 150°$)[27] or hydrophilic ($\alpha < 90°$).[27] CA is a measurement of the angle between the sample surface and inner surface of the water droplet.[28] Figure 2.3 shows a schematic diagram of the contact angle measurement obtained using Equation 2.1. θ is the angle between tangent drawn from the interface of water droplet and the sample surface to the sample surface.

$$\alpha = 180^{o} - \theta \tag{2.1}$$

Figure 2.3 Schematic diagram of contact angle measurement, $\alpha = 180^{o} - \theta$ by drawing two tangential lines between the droplet and MWNTs samples.

2.4.2 Young's Equation

For the case of a perfectly smooth, homogeneous and non-deformable surface, in the absence of gravitational effect, cosine of CA, α of the solid could be interpreted as ratio of the difference between solid – air γ_{SA} and solid – liquid γ_{SL} interfacial energy to liquid – air γ_{LA} interfacial energy as shown in Equation 2.2.

$$\cos\alpha = \frac{\gamma_{SA} - \gamma_{SL}}{\gamma_{LA}} \qquad (2.2)$$

The Young's Equation proposed for the study of surface wettability is too ideal to be considered in the case of real solids as any real solid would have a certain degree of roughness on the surface. Hence instead of using the Young's Equation, Wenzel's Equation (detailed in the next section) that takes into account of surface roughness for the measurement of CA would be more appropriate in our case.[25]

2.4.3 Wenzel Equation

In Wenzel's Equation, roughness of a surface is found to magnify the wetting properties of the solid. A solid surface that wets readily tends to wet more efficiently when roughness of the surface is increased and if the surface is smooth and water repelling, it will repel even more strongly when roughness is induced.

When dealing with CA of a rough surface, one has to take note of the difference between 'actual' surface interface and 'geometrical' surface interface. In the case of liquid-liquid or liquid-gas interface, the actual and geometrical interface is considered the same. However, when one considers interaction at a real solid surface, the actual surface would be greater than the geometrical surface due to roughness. Hence the term 'roughness factor, r' is used to represent the ratio of actual surface to geometrical surface:

$$\text{r} = \text{roughness factor} = \frac{\text{actual surface}}{\text{geometric surface}} \qquad (2.3)$$

Since forces are easier to visualize compared to energy value, Wenzel thus defines force concepts (the interfacial surface tensions) as numerically equal to the characteristic interfacial specific energy values, and deals with the forces involved as vector quantities that are constant in magnitude and variable in direction. Considering an ideal smooth surface, the energy content of a measured unit area would be equivalent to that of specific energy of the interface. Let force vectors S_1 and S_{12} represent specific interfacial energy of solid before and after wetting. The vector sum, $S_1 - S_{12}$, defines the adhesive tension, A, its negative value indicating its direction and marking it as resistant to wetting. Letting S_2 be the surface tension of the liquid on the solid and α_{true} be the contact angle. With the assumption that the three forces S_1, S_2 and S_{12} act on the same length of intersection of the boundary surfaces, relation between A, S_2 and α_{true} is found to be:

$$A = S_1 - S_{12} = S_2 \cos\alpha_{true} \tag{2.4}$$

Considering the effect of roughness, adhesive tension becomes rA and also considering α_{obs} as the CA that was measured on the rough surface, Equation 2.4 becomes:

$$rA = r\,(S_1 - S_{12}) = S_2 \cos\alpha_{obs} \tag{2.5}$$

Combining Equation 2.4 and Equation 2.5 we have the Wenzel Equation as:

$$\cos(\alpha_{obs}) = r\cos(\alpha_{true}) \tag{2.6}$$

In our experiment, for a hydrophobic surface (CA > 90^o) surface roughness would cause CA, α_{obs} to increase and hence causing the surface to become even more hydrophobic. Changing the surface to a hydrophilic surface with CA < 90^o, surface roughness would further reduce the CA causing even more spontaneous wetting to occur on the surface.[25]

2.4.4 Cassie's Law

With inspiration from Wenzel's work, Cassie[29] produced a law of his own for measuring CA of rough and heterogeneous surfaces. He further expresses the measurement of CA from Wenzel Equation to include two components of liquid in contact with air and solid.

Cassie stated that if unit geometrical area of a surface has an actual surface area σ_1 of contact angle α_1, and an area σ_2 of contact angle α_2, the energy E gained when the liquid spreads over the unit geometrical area is:

$$E = \sigma_1 (\gamma_{S_1A} - \gamma_{S_1L}) + \sigma_2 (\gamma_{S_2A} - \gamma_{S_2L}) \tag{2.7}$$

where γ_{S_1A} and γ_{S_1L} are interfacial solid-air and solid-liquid energy for the σ_1 areas and γ_{S_2A} and γ_{S_2L} are interfacial solid-air and solid-liquid energy for the σ_2 areas. The CA, α'' for the composite surface is then given by:

$$\cos\alpha'' = \frac{E}{\gamma_{LA}} = \sigma_1\cos\alpha_1 + \sigma_2\cos\alpha_2 \tag{2.8}$$

For the case of a porous surface, solid surface area is σ_1, and σ_2 represents air spaces; γ_{S_2A} is then zero and γ_{S_2L} becomes γ_{LA}, or

$$\cos\alpha'' = \sigma_1\cos\alpha_1 - \sigma_2 \tag{2.9}$$

Since MWNT surfaces can be considered as a porous surface, Cassie's Law would thus be relevant in our work on wettability of MWNTs.

References

(1) S., S. R. D. G. D. M., *Physical Properties of Carbon Nanotubes* Imperial College Press: 1998.

(2) Iijima, S. *Nature* **1991,** 354.

(3) Wildoer, J. W. G.; Venema, L. C.; Rinzler, A. G.; Smalley, R. E.; Dekker, C. *Nature* **1998,** 391.

(4) Treacy, M. M. J.; Ebbesen, T. W.; Gibson, J. M. *Nature* **1996,** 381.

(5) Tekleab, D.; Czerw, R.; Carroll, D. L.; Ajayan, P. M. *Applied Physics Letters* **2000,** 76.

(6) Jang, J. W.; Lee, D. K.; Lee, C. E.; Lee, T. J.; Lee, C. J.; Noh, S. J. *Solid State Communications* **2002,** 122.

(7) Baughman, R. H.; Zakhidov, A. A.; de Heer, W. A. *Science* **2002,** 297.

(8) Lieber, T. W. O. J. H. H. C. M., *Carbon Nanotubes* Springer Berlin / Heidelberg: 2001; Vol. 80/2001.

(9) Ralph Krupke, F. H., Hilbert V. Löhneysen, Manfred M. Kappes *Science* **2003,** 301, 344.

(10) Hermann, S.; Ecke, R.; Schulz, S.; Gessner, T. In *Controlling the Formation of Nanoparticles for Definite Growth of Carbon Nanotubes for Interconnect Applications*, 12th European Workshop on Materials for Advanced Metallization, Dresden, GERMANY, Mar 02-05, 2008; Dresden, GERMANY, 2008; pp 1979-1983.

(11) Avouris, M. S. D. G. D. P., *Carbon Nanotubes: Synthesis, Structure, Properties and Applications*. Springer-Verlag Berlin Heidelberg: New York, 2001.

(12) Song, S. N. W., X. K.; Chang, R. P. H.; Ketterson, J. B. *Phys. Rev. Lett.* **1994,** 72 679.

(13) Langer, L. B., V.; Grivei, E.; Issi, J. P.; Heremans, J. P.; Olk, C.H.; Stockman, L.; Van Haesendonck, C.; Bruynseraede, Y. *Phys. Rev. Lett.* **1996,** 76, 479.

(14) Bachtold, A. S., C.; Salvetat, J. P.; Bonard, J. M.; Forro, L.; Nussbaumer, T.; Schonenberger, C. *Nature* **1999,** 397, 673.

(15) Kreupl, F.; Graham, A. P.; Duesberg, G. S.; Steinhogl, W.; Liebau, M.; Unger, E.; Honlein, W. In *Carbon Nanotubes in Interconnect Applications*, European Workshop on Materials for Advanced Metallization, Vaals, Netherlands, Mar 03-06, 2002; Vaals, Netherlands, 2002; pp 399-408.

(16) Liu, Z. C.; Ci, L. J.; Kar, S.; Ajayan, P. M.; Lu, J. Q. *IEEE Trans. Nanotechnol.* **2009,** 8.

(17) Rinzler, A. G.; Hafner, J. H.; Nikolaev, P.; Lou, L.; Kim, S. G.; Tomanek, D.; Nordlander, P.; Colbert, D. T.; Smalley, R. E. *Science* **1995,** 269.

(18) Deheer, W. A.; Chatelain, A.; Ugarte, D. *Science* **1995,** 270.

(19) Rao, A. M. J., D.; Haddon, R. C.; Zhu, W.; Bower, C.; Jin, S. *Applied Physics Letters* **2000,** 76, 3813.

(20) Bonard, J.-M. S., T.; Meier, F.; de Heer, W. A.; Chatelain, A.; Salvetat, J. -P.; Forro, L. *Ultramicroscopy* **1998,** 77, 7.

(21) Nordheim, R. H. F. L. W. *Proceedings of the Royal Society of London. Series A, Containing Papers of a Mathematical and Physical Character* **1928,** 119, 173.

(22) Cheng, Y. T.; Rodak, D. E. *Applied Physics Letters* **2005,** 86.

(23) Hong, Y. C.; Shin, D. H.; Uhm, H. S. *Surface & Coatings Technology* **2007,** 201.

(24) Li, S. H.; Li, H. J.; Wang, X. B.; Song, Y. L.; Liu, Y. Q.; Jiang, L.; Zhu, D. B. *Journal of Physical Chemistry B* **2002,** 106.

(25) Wenzel, R. N. *Ind. Eng. Chem.* **1936,** 28.

(26) Sun, T. L.; Wang, G. J.; Feng, L.; Liu, B. Q.; Ma, Y. M.; Jiang, L.; Zhu, D. B. *Angewandte Chemie-International Edition* **2004,** 43.

(27) Burton, Z.; Bhushan, B. *Nano Letters* **2005,** 5.

(28) Zisman, W. A., *Relation of Equilibrium Contact Angle to Liquid and Solid Constitution.* American Chemical Society Applied Publications: 1964; p 51.

(29) D., C. A. B. *Discuss. Faraday Society* **1948,** 3, 11.

Chapter 3: Experimental Procedures

3.1 Introduction

In this section, we will explain how MWNTs are synthesized using a Plasma Enhanced Chemical Vapor Deposition (PECVD) system. Following which, descriptions of the working principles of some of the techniques and equipment used in analyzing the samples, namely, Scanning Electron Microscopy (SEM), Transmission Electron Microscopy (TEM), Fluorescence Microscopy (FM), Oxygen Reactive Ion Etching (O_2 RIE), Laser Pruning System and Field Emission System (FE) will be provided.

3.2 Synthesis of Multi-walled Carbon Nanotubes

The MWNT samples used in the experiments were prepared using a Plasma Enhanced Chemical Vapor Deposition (PECVD) system.

Clean N – type Silicon (Si, 100) wafers containing native oxide layer were used as substrates. They were cut into small pieces of approximately 5 mm by 5 mm and pre-cleaned with ethanol for sputtering (Model: radio frequency (RF) Magnetron Denton Discovery 18). During the sputtering process, plasma glow produced from Argon (Ar) gas was used to bombard an iron (Fe) target (99.9%, Aldrich) with a base pressure of ~ 10^{-7} Torr. Flow rate of Ar gas was maintained at 100 sccm (standard cubic centimeters per minute) with pressure of sputtering being kept at 10 mTorr throughout the sputtering process. An RF power of 100 W was used to deposit Fe catalyst layer of thickness 17 nm onto the substrate at room temperature (21 °C) with sputtering rate of 3 nm/min.[1] Choice of such thin catalyst layer was to prevent reduction in MWNTs density,[2] while synthesizing MWNTs with smaller inner diameter.[3]

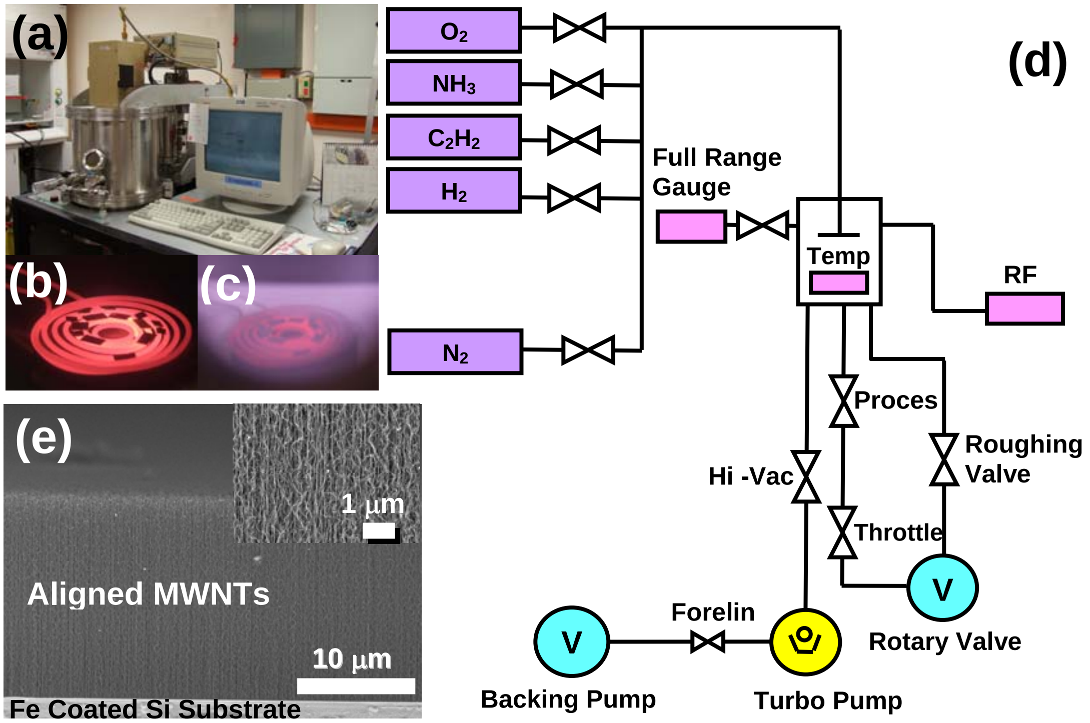

Figure 3.1 (a) PECVD chamber. (b) Glowing heating coil with pieces of catalyst coated Si. (c) Introducing C_2H_2 and H_2 mixture into the chamber. (d) Schematic diagram of the PECVD system. (e) SEM images of aligned MWNTs grown via PECVD method.

The catalyst coated Si substrates were placed in a PECVD chamber (Figure 3.1a) with heating coil for heating (Figure 3.1b). The substrates were then heated to ~700 ^{o}C in H_2 plasma (Figure 3.1c) with RF power at 100 W for 10 min. The aim was to promote the formation of catalyst particles and elemental Fe essential for growth of MWNTs. After which, a gaseous mixture of C_2H_2 as carbon source and H_2 with flow rates at 15 sccm and 60 sccm respectively was introduced into chamber. This combination produces reactive species in the plasma used to remove any excess amorphous carbon whose presence inhibits formation of nanotubes.[4] Temperature of the substrate was maintained at ~700 ^{o}C. The working pressure and RF power were also maintained at 1200 mTorr and 100 W. Deposition were carried out for duration of 60 min, producing aligned MWNTs carpet of 50 – 60 μm.[2]

3.3 Experimental Setup

3.3.1 Scanning Electron Microscopy (SEM)

Scanning electron microscopy (SEM) generally produces images reflecting surface morphology. Images of SEM reported in this report were captured using JEOL JSM-6400F field emission scanning electron microscope system operating at voltage and current of 5 kV and 10 μA respectively. This SEM has a resolution of about 5 nm and works under 9.63×10^{-5} Pa. Sample holder could be tilted or rotated within certain limit. By utilizing special sample holder, cross-sectional views of MWNTs such as the ones in Figure 3.1E were obtained.

Figure 3.2 shows a schematic diagram of the SEM. Firstly, electrons are emitted from the field emission tip. As the electrons accelerate down towards the sample stage, two magnetic lenses help to set both the spot size at which the electron would hit the sample and also to help bring the spot into focus. The electron beam would lastly go through manual focusing onto the sample using objective lens (affects microscope resolution), stigmator and beam limiting aperture (prevent stray electrons from hitting the sample) before hitting the sample surface. A scanning coil (not shown in the schematic) helps to scan the beam across the sample line by line.

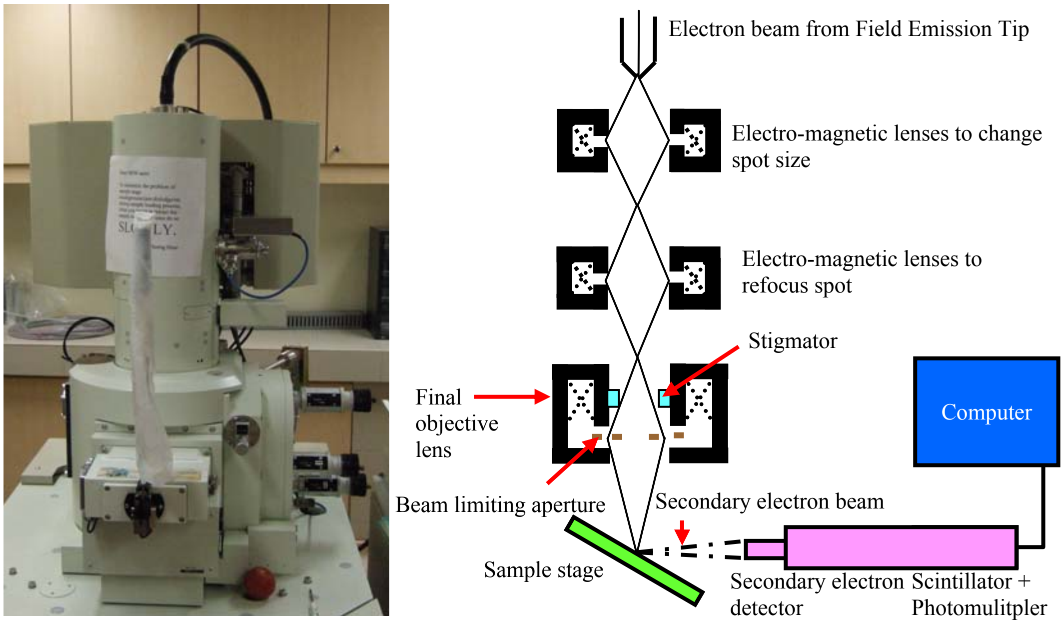

Figure 3.2 Schematic diagram, not to scale, of the SEM (Insert is photo of SEM used for this experiment)

Upon hitting the sample, secondary electrons would be emitted from the sample surface and accelerated towards positively charged electrode of the detector, passing through to scintillator. The electrons collide with the scintillator material and photons are produced. The photons then travel through a light pipe via total internal reflection to a photomultiplier where upon striking the surface of the multiplier, photons are converted to highly amplified electrical signals. These signals were then fed to a computer display where images of MWNTs surface morphology would be shown on computer monitor and captured for further analysis.[5]

3.3.2 Transmission Electron Microscopy (TEM)

Transmission electron microscopy (TEM, JEOL JEM-2010F) was employed for the analysis of the difference between both 1st and 2nd generations of MWNTs grown. TEM normally work with an acceleration voltage of 200 kV in order to obtain clear atomically-resolved high-resolution TEM (HRTEM) images. For studies of the MWNTs, the samples were scratched off the substrate and dropped onto copper (Cu) grids with carbon films.

3.3.3 Fluorescence Microscopy (FM)

Fluorescence Microscope was used to capture live view images of the formation process of the negative MWNT microstructures. Fluorescence images of QDs suspended in water and deposited onto pre-patterned MWNTs were captured using an Olympus IX71S1F – 3 Inverted Microscope. The QDs were illuminated via two 12V/100W Mercury (Hg) lamp tilted rearward. The UV source emitted goes through a single reflection after bouncing off a dichroic filter through apochromat relay lenses before hitting the inverted samples. Samples used were pasted onto glass slides using normal double sided tapes. Reflected images from glowing samples were then passed through the diaromat filter again before being captured by a camera as shown in Figure 3.3.

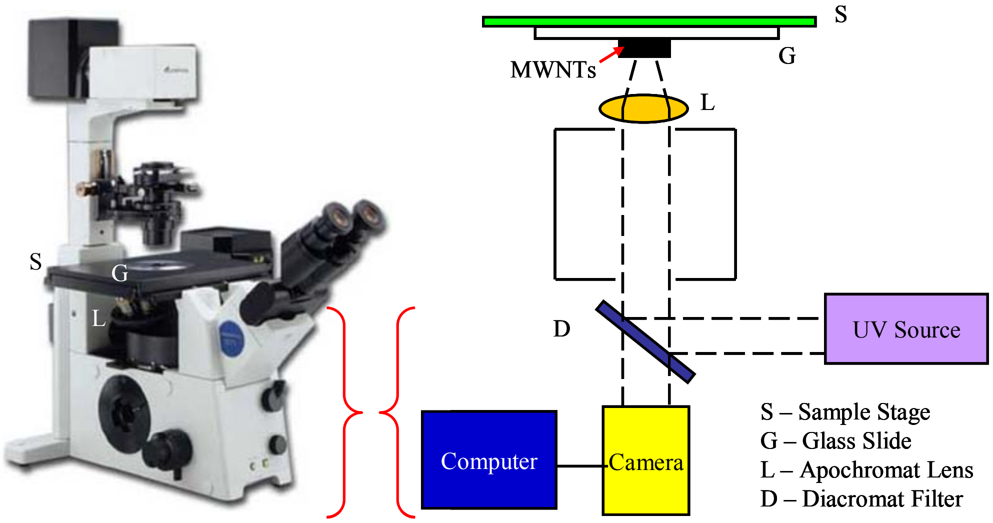

Figure 3.3 Schematic diagram, not to scale, of the FM (Insert is photo of the microscope used)

3.3.4 Oxygen Reactive Ion Etching (O_2 RIE)

MWNTs are hydrophobic by nature, hence when we are dealing with water assisted assembly of MWNTs, it is necessary to change the hydrophobic nature of the MWNTs to hydrophilic. Such conversion is to assist the spreading of water across the MWNTs. Based on previous experiments,[6] oxygen reactive ion etching (O_2 RIE) of MWNTs prove to be an efficient way to functionalize the MWNTs and change the surface wettability of the MWNTs from being hydrophobic to hydrophilic.

As-grown MWNTs were placed inside the chamber of a SAMCO RIE-10N Reactive Ion Etching Unit, on a RF driven capacitively coupled electrode and pumped down to a base pressure of 4×10^{-6} Torr. Following which, Oxygen (O_2) gas was introduced at a flow rate of 34.5 sccm for 30s. A radio frequency (RF) glow discharge was then used to generate the reactive O_2 plasma at 13.56 MHz. The RF power used was set at 20 W and the reflected power was about 1 W. Throughout the etching process, the work pressure was maintained at ~ 0.05 Torr in the chamber and the temperature was kept at 20^{o}C during the etching process.

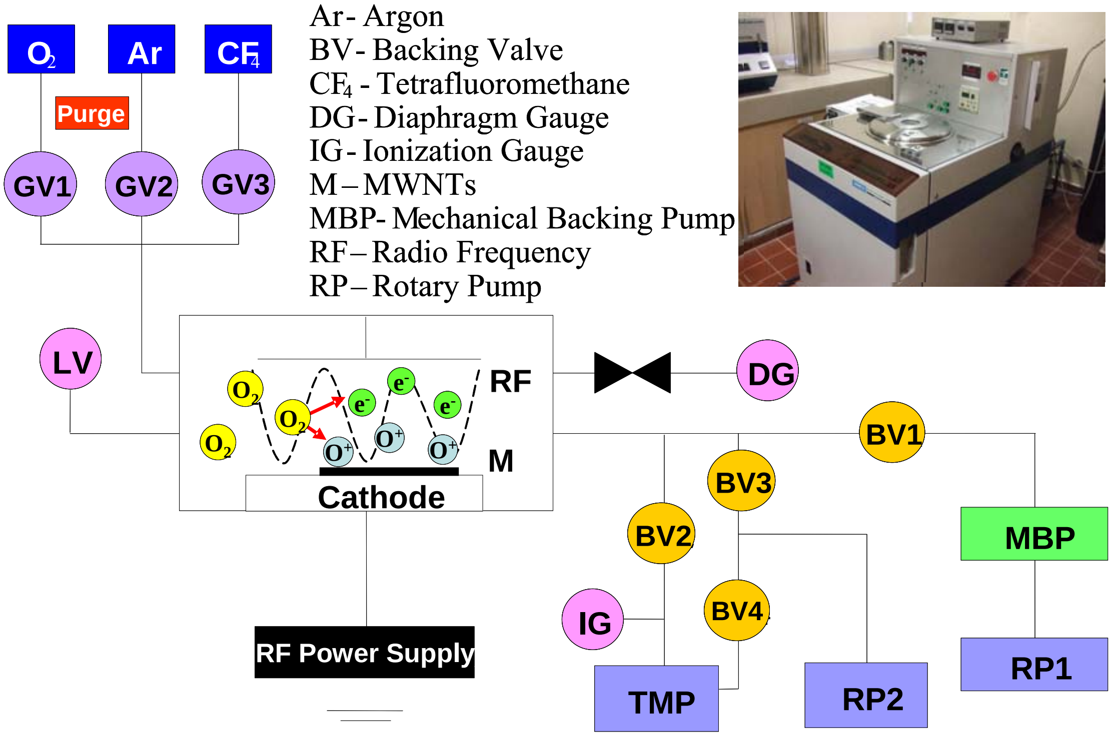

Figure 3.4 Schematic, not to scale, of the RIE system (Insert is photo of RIE system used for this experiment)

3.3.5 Contact Angle (CA) System

The measurement of the contact angle was achieved using a custom-built Contact Angle (CA) measurement system (Figure 3.5). After O_2 RIE treatment, distilled water droplets were then sprinkled onto MWNTs surface. Images of droplets were being captured using charge-coupled device (CCD) camera (maintained at 8 times zoom) that was connected to TV-Tuner, which in turn was linked to a laptop for video and image capturing.

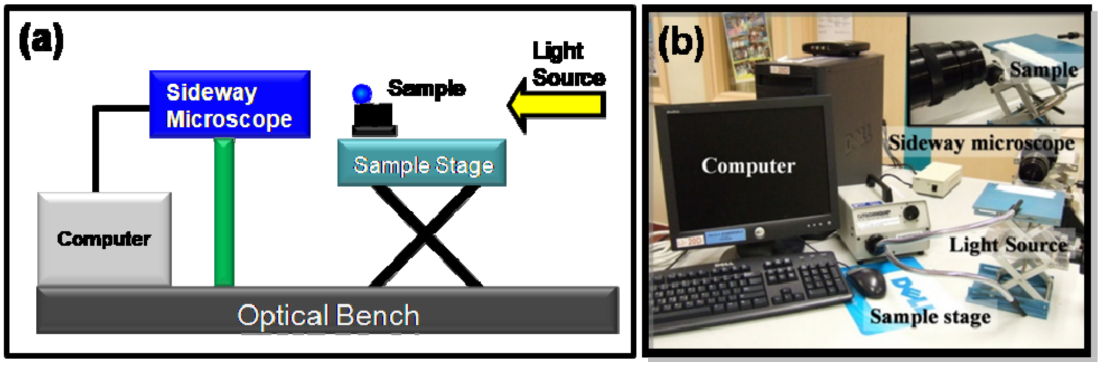

Figure 3.5 (a) Schematic of the experimental set up. (b) Photo of the experimental setup with the insert showing a close up of the sample stage.

The images were subsequently analyzed to determine the contact angle (CA) between the water droplet and the MWNT surface. Measurements of CA were obtained using an ImageJ software, over an average of 80 droplet images per sample. The average size of water droplets was 100 ± 30 μm (calibrated using tungsten wire of diameter 80 μm). Figure 3.5 shows the experimental set-up developed in this work for the measurement of CA.

3.3.6 Laser Pruning System

For the micro-patterning process, we made use of a laser pruning technique developed in our lab to create micro-structures from the aligned MWNTs array. Figure 3.6 shows a schematic illustration of the laser pruning setup. An incident diode laser (λ = 660 nm) with a beam beam width of 3 mm, and a measured power of 70 mW was directed into the microscope using two reflecting mirrors (M). The beam splitter (S1) directs the beam towards the objective lens. The beam was focused onto the sample using a Nikon 50X lens (numerical aperture of 0.55) objective lens (L).

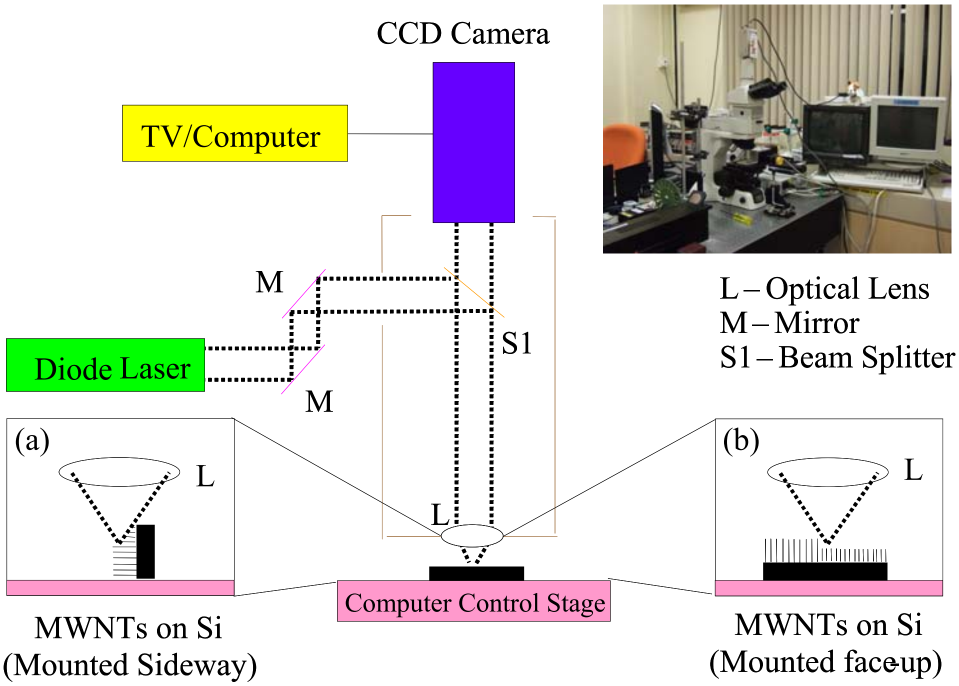

Figure 3.6 Schematic, not to scale, of the laser pruning setup. MWNTs were cut using a focused laser beam in (a) side-way and (b) an upright position.

The sample was placed on a MICOS XY sample stage with 25 mm travel and a minimum step size of 50 nm in the x and y directions. It was controlled by a MICOS motor controller and interfaced to the computer via Microsoft Visual Basic software. During cutting, light was collected via the objective lens (L) and passed through S1 to be captured by a JVC CCD camera which was then connected to a TV and a computer for viewing and capturing images/videos throughout the process.[7] Depth of MWNTs trimmed off by laser was dependent on the power of the laser and how well the laser was being focused onto the sample surface. Thus using this method, we were able to create patterns on MWNTs samples.

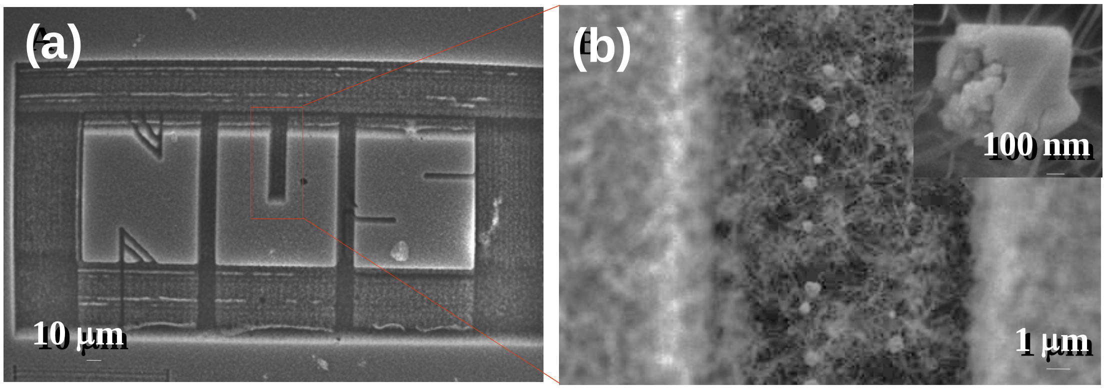

Figure 3.7 SEM images of (a) NUS structure being created after pruning by laser on MWNTs surface; (b) zoomed in view of region enclosed by the red rectangle, revealing small irregular shape amorphous clusters. Insert in (b) is a zoomed in on one of the small amorphous cluster.

Figure 3.7 shows SEM images of MWNTs trimmed by laser. Figure 3.7a shows 'NUS' made up of MWNTs carpet after laser cutting. From Figure 3.7b regions pruned by laser reveals small clustering of irregularly shaped amorphous particles, which were found on trimmed MWNTs surface. Insert in Figure 3.7b shows a zoom in image on one of the amorphous particles.

3.3.7 Field Emission

With high aspect ratio of MWNTs giving them the edge as potential candidate for field emission, field emission measurement of various samples were conducted at room temperature using a two-parallel plate arrangement in a vacuum chamber with a base pressure of 4 x 10^{-6} Torr (Figure 3.8). FE measurements for each sample were conducted by securing the sample to a copper (Cu) substrate cathode using a Cu double-sided tape. In the setup, indium tin oxide (ITO) glass coated with a layer of phosphor acted as the anode. A 200 μm thick polymer film with a square opening was employed as a spacer between the electrodes. The voltage across the electrodes was increased in steps of 10 V up to a maximum of 850 V. The corresponding emission current was measured using a Keithley 237 high-voltage source measure unit (SMU) repeatedly till there was no more variation in repeated measurement. A schematic of the FE setup is as illustrated in Figure 3.8a. Figure 3.8b and 3.8c shows photographs of the actual experimental setup and the sample holder, respectively.

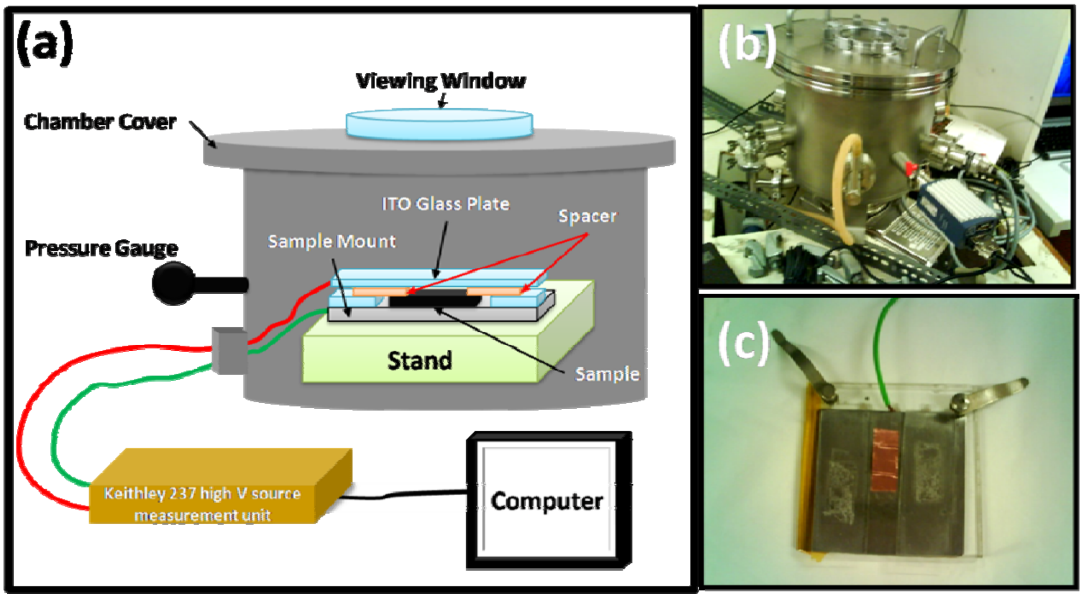

Figure 3.8 (a) Schematic of the FE measurement setup. (b-c) Photographs of the actual experimental setup, (b) FE chamber and (c) sample holder.

References

(1) Zhu, Y. W.; Cheong, F. C.; Yu, T.; Xu, X. J.; Lim, C. T.; Thong, J. T. L.; Shen, Z. X.; Ong, C. K.; Liu, Y. J.; Wee, A. T. S.; Sow, C. H. *Carbon* **2005,** 43.

(2) Wang, Y. H.; Lin, J.; Huan, C. H. A.; Chen, G. S. *Appl. Phys. Lett.* **2001,** 79.

(3) Ren, Z. F.; Huang, Z. P.; Wang, D. Z.; Wen, J. G.; Xu, J. W.; Wang, J. H.; Calvet, L. E.; Chen, J.; Klemic, J. F.; Reed, M. A. *Appl. Phys. Lett* **1999,** 75.

(4) Bell, M. S.; Teo, K. B. K.; Lacerda, R. G.; Milne, W. I.; Hash, D. B.; Meyyappan, M. *Pure and Applied Chemistry* **2006,** 78.

(5) Yacobi, B. G. H., D. B., *Scanning Electron Microscopy*. Plenum Press: 1994.

(6) Li, P. H.; Lim, X. D.; Zhu, Y. W.; Yu, T.; Ong, C. K.; Shen, Z. X.; Wee, A. T. S.; Sow, C. H. *JPCB* **2007,** 111.

(7) Lim, K. Y.; Sow, C. H.; Lin, J. Y.; Cheong, F. C.; Shen, Z. X.; Thong, J. T. L.; Chin, K. C.; Wee, A. T. S. *Adv. Mater.* **2003,** 15.

Chapter 4: Versatile Transfer of Aligned Carbon Nanotubes with Polydimethylsiloxane as an Intermediary

4.1 Introduction

In this chapter, we report a simple and direct technique for transferring aligned MWNTs grown on Si substrates at room temperature, onto target substrates with polydimethylsiloxane (PDMS) intermediation. Since PDMS is a soft elastomer at room temperature, the technique can be readily used to transfer MWNTs onto both conductive and flexible substrates. Further characterizations were also carried out to investigate the surface morphology and tip microstructures of transferred MWNTs, and the interface between them and target substrates. From transport measurements, a maximal current density of $\sim 10^4$ A/cm^2 through the MWNTs was achieved. From field emission measurements, low emission turn on field of 0.7 V/μm and high current density up to 8 mA/cm^2 (at 1.15 V/μm) were obtained from transferred MWNTs onto polymer substrates. Furthermore, the surface of the transferred MWNTs was found to be more hydrophilic as compared to the super hydrophobic surface of as-grown MWNTs.

4.2 Transferring MWNTs onto Various Substrates

Figure 4.1a shows a schematic of the experimental procedures used in transferring the MWNTs onto different substrates using PDMS as intermediate. Figure 4.1b shows a collection of aligned MWNTs transferred onto different substrates. In our preliminary results, the MWNTs were successfully transferred onto metallic substrates such as Cu and Fe foils, brittle substrates such as glass slides, flexible polymers and fabrics such as paper and cloth. The sample size was dependent on the size of as-grown MWNTs on Si. Typical dimensions of our samples were about one centimeter by a few millimeters. It was found that wetting of the PDMS solution on the target substrate was crucial for adhesion of MWNTs. This in turn, determined the efficiency of the transfer process. Repeated experiments showed that Pt was a suitable candidate for inducing good wetting and excellent contact on substrates that were not readily wetted by PDMS. Figure 4.1b shows successful transfer of MWNTs onto glass and transparent polymer substrates, making them potential candidates for optoelectronic applications. The flexibility of polymer film with transferred aligned MWNTs can be seen in Figure 4.1c. No obvious breaking or peeling of MWNTs was observed when the sample was bent. Real foldable devices could be realized based on MWNTs transferred onto cloth or paper.

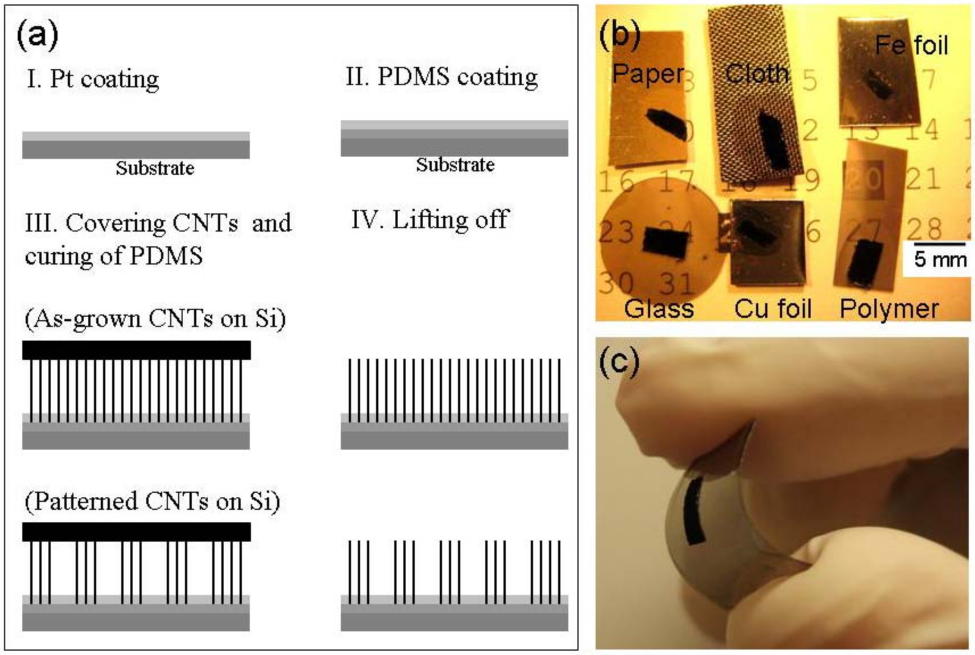

Figure 4.1 (a) Schematic of direct transfer process of aligned as-grown or patterned MWNTs onto target substrates. (b) Optical image of aligned MWNTs transferred onto different substrates used in the experiments. (c) Optical image illustrating the flexibility of a transferred MWNT film on polymer substrate.

4.3 Comparison Between As-Grown and Transferred MWNTs

Figure 4.2(a,b) show the top view SEM images of as-grown and transferred MWNTs respectively. In this case, the height of MWNTs was ~70 μm and the average diameter was 20-40 nm with the top part of as-grown MWNTs highly curved and entangled. Many particles with size of a few hundred nanometers could be observed on the sample and thorn-shape coatings could also be seen on the surface of some MWNTs as shown in the inset of Figure 4.2a. Comparatively, the top of transferred MWNTs, which used to be the root part of as-grown MWNTs, was much cleaner and had better alignment, as shown in Figure 4.2b and its inset.

Such differences could be observed more clearly from their Raman spectra (Figure 4.2c). In the spectra, the two main peaks at ~1340 and ~1575 cm^{-1} could be identified as the D and G bands of MWNTs.[1] After transfer, although the positions of D and G bands remained unchanged, the ratio of D band intensity to that of G band reduced from 0.80±0.06 to 0.42±0.02. Since D band was used to indicate disordered or amorphous carbon while the G-band corresponds to ordered graphite in MWNTs,[1] the Raman study suggested that the root part of as-grown MWNTs contain fewer defects than the top part. It was previously reported that the top of MWNTs tend to be covered by amorphous carbon after long-duration growth,[2-4] which means that our transfer technique allows one to select the higher-quality region of aligned MWNTs as the tip of sample. This will minimize unexpected influences of amorphous carbon in certain applications such as field emitters. Having previously developed a focused laser pruning technique to create patterned microstructures made of an array of aligned MWNTs array,[3] we used the same method to fabricate a periodic array of MWNTs pillars and parallel platforms on the as-grown sample. As shown in Figure 4.2d, these patterns were successfully transferred with little distortion onto another Si substrate. Using with different patterning techniques, various architectures of MWNTs could be created and transferred onto desired substrates via this simple transfer method.

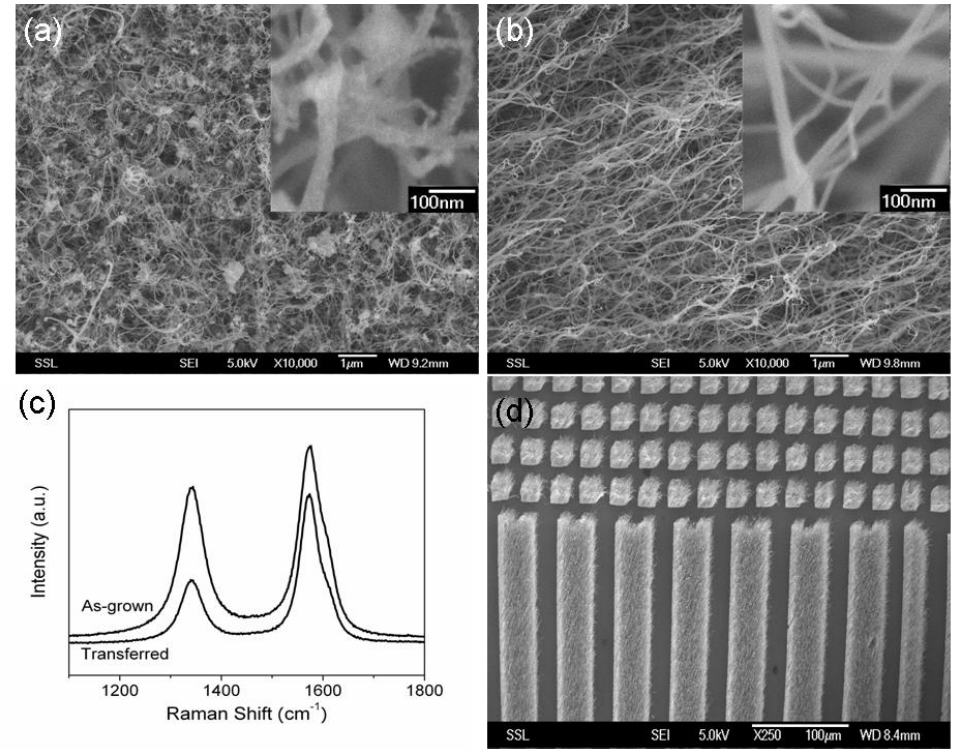

Figure 4.2 Typical top-view SEM images of (a) as-grown and (b) transferred MWNTs. The insets show the close-up views of individual MWNTs respectively. (c) Micro Raman spectra from the surface of as-grown and transferred MWNTs. (d) SEM image of a patterned and transferred MWNTs sample created by focus laser pruning on the as-grown substrate followed by the transfer.

4.4 Cross Section Analysis of Transferred MWNTs using SEM

The cross-section of a MWNT film transferred onto glass was subject to detailed SEM studies (Figure 4.3). In Figure 4.3a, a PDMS layer with a thickness of ~ 15 μm was observed. From the image, the PDMS had diffused uniformly into the forest of MWNTs and bonded them together during the polymerization process. Higher magnification of Region b (interface of the protruding MWNTs and PDMS layer) is shown in Figure 4.3b.

From the image, a sharp interface could be observed at micrometer scale. In Figure 4.3c, a close-up view of Region C (bottom part of the PDMS layer) showed that some of the MWNTs were encompassed with polymers while others were left exposed. However, not all the exposed MWNTs were in contact with the Pt coating due to the non-uniform height of the as-grown MWNTs. Nevertheless, good wetting and adhesion between the PDMS and Pt made the contact strong.

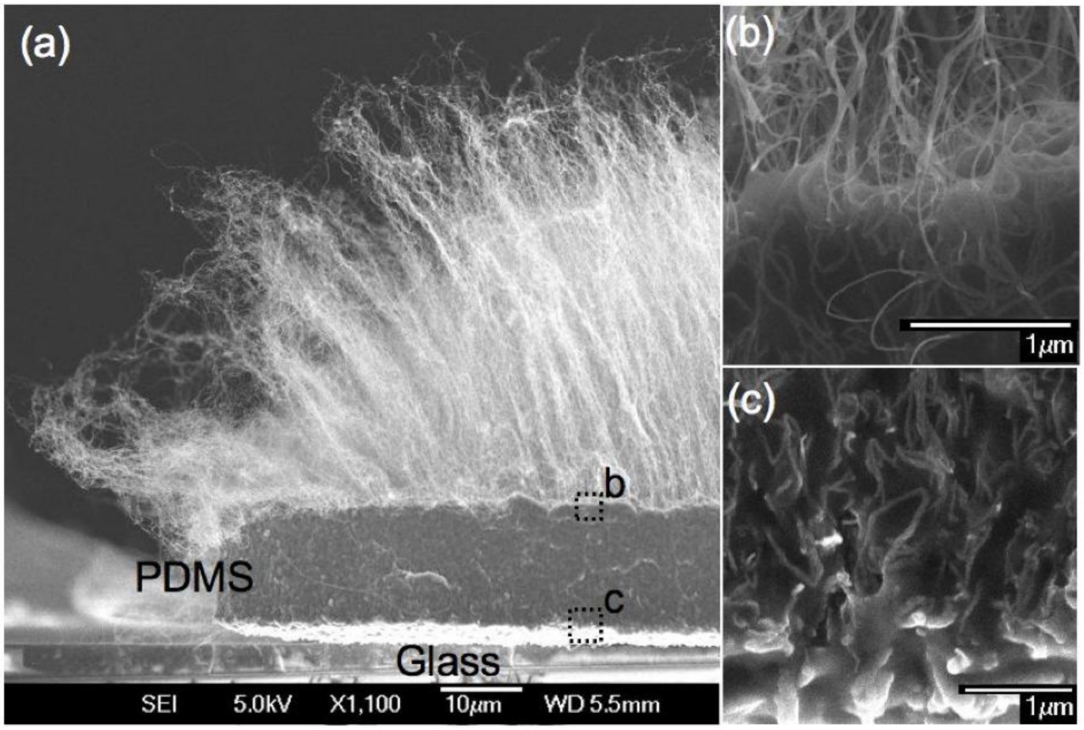

Figure 4.3 Side view SEM image of transferred MWNTs on glass substrate. Markers b and c represent those regions magnified in (b) and (c) respectively.

4.5 TEM Analysis of Transferred MWNTs

TEM investigations were carried out on MWNTs directly transferred onto a Cu O-ring. With this method, only the tips of transferred MWNTs were exposed to the electron beam since the other end (tips of as-grown MWNTs) was bonded to the Cu ring by PDMS. Figure 4.4a shows a low magnification image of the top part of the transferred MWNTs. Two typical types of tips were observed from the figure. Solid arrows point at MWNT tips with round edges while block arrows mark those with sharp edges. The close-up TEM image (Figure 4.4b) shows that the round edged tips were hollow rings in the two-dimensional projection by the electron beam. The high resolution TEM (HRTEM) image in Figure 4.4c shows that the ring has a multi-layer structure with the interlayer distance of about 3.4 Å. On the other hand, no remarkable layers were found from the sharp edged tips, as shown in Figure 4.4d. The TEM observations indicated that open-ended tips were dominant for transferred MWNTs.

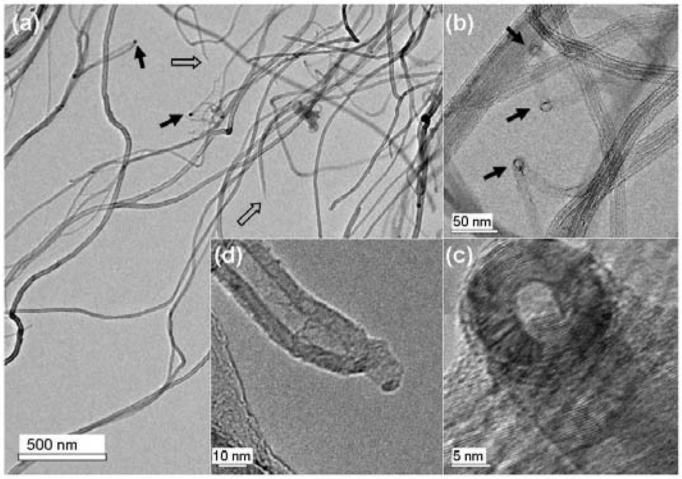

Figure 4.4 (a) Typical low-magnification TEM image with different ending tips marked by solid and block arrows. (b) and (c) Close-up views of hollow rings. (d) Close-up view of a sharp tip, caused by breaking during transfer.

4.6 SEM Analysis of Transferred Substrate

In our work, the aligned arrays of MWNTs were grown on Si substrates coated with Fe nanoparticles as catalyst. The growth of MWNTs mainly followed a root growth process where, the Fe particles remained firmly anchored on the Si substrate. During the transfer process, pulling/stretching caused the MWNTs to detach from Fe particles, resulting in transferred MWNTs with open-ended structures. This result was consistent with our SEM observation (Figure 4.5a), where most Fe catalyst particles were left on the Si substrates after transfer. Moreover, for MWNTs with defects at root part, they would tend to break at these defective points by the axis stress.[5] Some broken MWNTs left on the Si substrate were marked by arrows in Figure 4.5a. The stretching, possibly accompanying with twisting, may cause the buckling, collapse or extension in MWNTs.[6, 7] This could explain the absence of ordered layers around the broken tips under TEM. It was interesting that, those catalyst particles left on Si substrates were still active and second or multiple growth had been realized on the "recycled" substrates. Figure 4.5b and c show cross-sectional SEM images of as-grown (1st generation) MWNTs and regrown (2nd generation) MWNTs on the same Si substrate after the as-grown ones were transferred. Clearly, more aligned and neat MWNT arrays could be obtained from the regrowth. However, the growth rate was lower under the same conditions. This could be due to the lower efficiency of the "recycled" Fe catalyst.

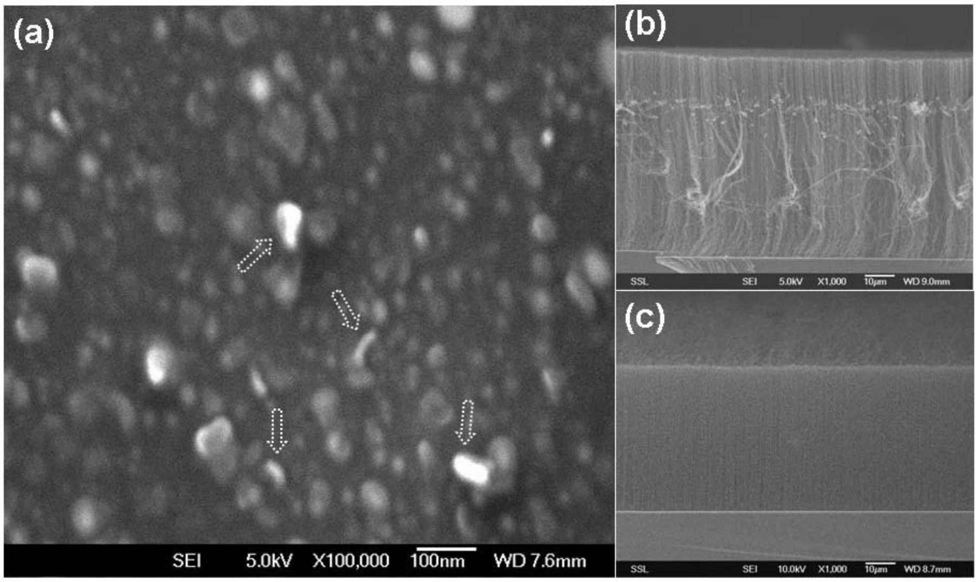

Figure 4.5 (a) Typical SEM image of the Si substrate after the MWNTs grown on it have been transferred. Dashed block arrows point at those broken MWNTs with root left. (b) Side view SEM image of as-grown first-generation MWNTs. (c) SEM image of the second-generation MWNTs grown on the “recycled” Si substrate after the MWNTs in shown in (b) were transferred away.

4.7 I-V Measurements of Transferred MWNTs

The formation of a good electrical contact was essential for the application of transferred MWNTs in electronic devices such as interconnects. A simple two-probe measurement was carried out in vacuum to characterize the electrical transport properties of MWNTs transferred on a polymer substrate. The current versus voltage (*I*-*V*) plot is shown in Figure 4.6a. As observed, the curve is rather linear and this could be an indication of the ohmic nature of the contacts between the probe and MWNTs/Pt. The effective conductivity was estimated to be 0.5~0.7 S/cm, based on the SEM measurements of the contact area of the probe tip on MWNTs and the length of this sample. Passing a high current through the sample would cause the MWNTs to break down as shown in Figure 4.6 (inset). The maximal current density was estimated to be ~10^4 A/cm^2 from repeated measurements. It was worth noting that both values could be underestimated since the real number of MWNTs involved in the transport was unknown due to the entangled nature of MWNTs on the top layer. Compared with previous reports,[8, 9] the conductivity of our transferred MWNTs was one or two orders lower, possibly due to high contact resistance between probes and MWNTs, defective MWNT structures or fewer contact points on Pt coating, as revealed in Figure 4.5. Better contacts could either be obtained by optimizing the uniformity of the length of as-grown MWNTs or by applying a suitable pressure on the Si during curing of the PDMS. Through application of a suitable amount of pressure, more contact points between Pt coating and tips of MWNTs could be created and hence achieving better contacts. However, overwhelming pressure may cause the Si substrate to be in contact with the PDMS film. This in turn would lead to difficulty in removing the Si substrate and crunching of MWNTs when the Si substrate was forcefully removed. Thus, an optimized contact between MWNTs and Pt coating depends on the balance of the following factors: length of MWNTs, thickness of PDMS coating and pressure on the Si during PDMS curing.

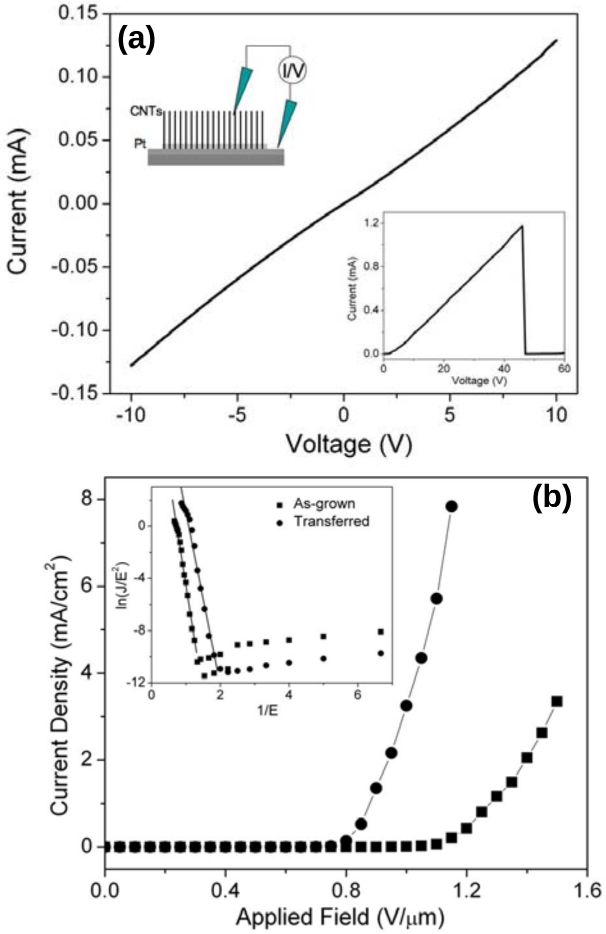

Figure 4.6 (a) Typical I-V curve to show the electrical transport of transferred MWNTs on a Pt coated polymer substrate. Upper inset schematically demonstrates the two-probe measurement setup and bottom inset shows the breakdown of MWNTs measured under high voltage. (b) Typical field emission *J-E* curves and (inset) corresponding FN plots from as-grown MWNTs on Si and those transferred on a polymer substrate.

4.8 Field Emission of Transferred MWNTs

The good electrical contact between MWNTs and substrates renderred them as promising field emitters. Figure 4.6b shows the field emission current density versus applied field (*J*-*E*) curves and corresponding Fowler-Nordheim (FN) plots of as-grown and transferred

MWNTs on polymer substrates. By comparison, the transferred MWNTs possessed a lower field emission turn-on field of about 0.7 V/μm, corresponding to a current density of 10 μA/cm^2. A high current density of 8 mA/cm^2 was observed when the applied field was only 1.15 V/μm. Such a field emission performance was comparable to the best performance from MWNTs.[10-13] The linearity in FN plots suggested that the emission current originated from quantum tunneling.[14] At high electric fields, the FN plots from both samples show a deviation from a straight line. Such deviations were often observed from MWNT emitters and could be due to space charge effect,[15] non-metallic density of states at the tip,[16] or different enhancement factors within emitters.[17] Such deviation was more notable in the case of transferred MWNTs due to the larger emission current. By fitting the whole FN part with a straight line, an enhancement factor of ~5400 for transferred MWNTs could be estimated from the FN equation after setting the work function at 5 eV.[18] Such a value was comparable to reported enhancement factors from MWNT films,[19, 20] and was sufficient for the application in field emission displays. On the other hand, the as-grown MWNTs gave a lower enhancement factor of ~4300. The improvement of field emission performance after transfer was consistent with the previous report based on metal intermediation transfer of MWNTs.[21] The superior field emission property of transferred MWNTs could be attributed to a few factors. These include cleaner MWNTs exposed to field emission and better alignment of transferred MWNTs. Furthermore, as revealed by TEM, the open-ended structures of transferred MWNTs could contribute to the overall improved emission properties,[22] especially the sharp tips that may further enhance the local electric field and thus emission current. In addition, as seen from figure 3c, only a fraction of MWNTs was in contact with the Pt layers and formed electron transport channels. Although the MWNTs were highly entangled, the actual number of effective emitters could be reduced and thus the screening effect due to high density of MWNTs may be partially compensated. However, more systematic study of the effect of transfer on the electrical property, including field emission is necessary to clarify the different contributions of these factors.

4.9 Hydrophobicity of Surface of Transferred MWNTs

Surface morphology and structure differences had significant influence on the wettability of aligned MWNTs.[23] A few reports had shown that tall as-grown MWNT arrays were super hydrophobic with contact angles larger than 150°.[24, 25] Our previous work had also demonstrated a high contact angle of 150° for our MWNTs grown with PECVD.[26] The surface wetting property of transferred MWNTs were also investigated in this work. As shown in Figure 4.7, after transfer, the contact angle of water droplet on the surface decreased from the original 151.6 ± 5.5° for as-grown MWNTs to 93.4 ± 5.8° for transferred ones. Such a significant decrease indicated that the surface of transferred MWNTs was much more hydrophilic than that of as-grown MWNTs. This could be attributed to factors such as reduction in density and increase in alignment of MWNTs, open-ended tip structures and also cleaner MWNTs with less amorphous carbon. Since the fraction of air-trapping between MWNTs was unknown, it was difficult to unambiguously determine the role of morphological changes. On the other hand, internal wetting could occur due to the open-ended structure of some MWNTs after transfer.[27] For the MWNTs with diameters less than 40 nm, the internal contact angle was further deceased, which resulted in a more hydrophilic surface.[28] Although it was reported that high graphitization surface could cause high external contact angles of MWNTs,[29] smaller internal contact angles may cause the internal wetting to dominate in the process of determining the overall surface wettability.[28] Compared with as-grown MWNT arrays, a more hydrophilic surface of transferred MWNTs offers new potential for applications in water-based chemical/electrical analysis.

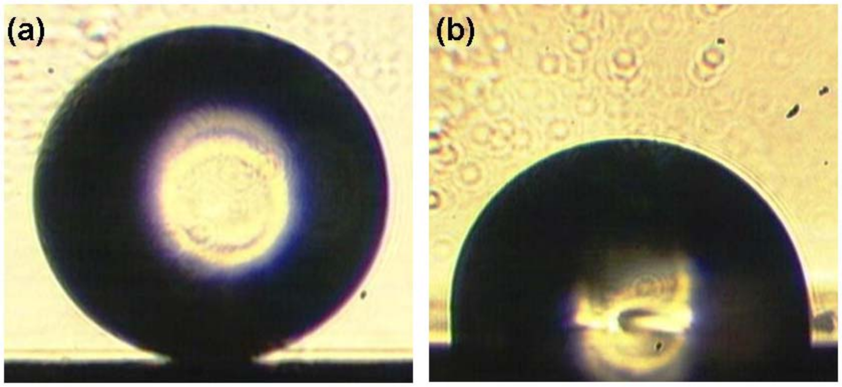

Figure 4.7 Typical optical image of a water droplet on the surface of (a) as-grown and (b) transferred MWNT arrays.

4.10 Conclusion

In summary, a direct transfer technique to fabricate aligned MWNTs on a wide range of substrates with the assistance of PDMS was presented. The transfer could be carried out at room temperature, largely broadening the range of applications of this simple technique. The transfer could be realized on conducting metals, transparent glass, flexible polymers and even cloth. Characterization had shown that the surface of transferred MWNTs was cleaner and had fewer defects as compared to the top part of as-grown

MWNTs. Open-ended tips were also observed from transferred MWNTs. Satisfactory electrical conductance, superior field emission performance and a more hydrophilic surface wettability had been observed from transferred MWNTs. This versatile and simple technique could find more applications in MWNTs based electronics such as interconnects, flexible field emission displays and electrodes for fuel cells.

References

(1) Nilsson, L.; Groning, O.; Emmenegger, C.; Kuttel, O.; Schaller, E.; Schlapbach, L.; Kind, H.; Bonard, J. M.; Kern, K. *Appl. Phys. Lett.* **2000,** 76.

(2) Kim, D. H.; Jang, H. S.; Kim, C. D.; Cho, D. S.; Kang, H. D.; Lee, H. R. *Chem. Phys. Lett.* **2003,** 378.

(3) Lim, K. Y.; Sow, C. H.; Lin, J.; Cheong, F. C.; Shen, Z. X.; Thong, J. T. L.; Chin, K. C.; Wee, A. T. S. *Adv. Mater.* **2003,** 15.

(4) Huang, S.; Dai, L. *J. Phys. Chem. B* **2002,** 106.

(5) Dumitrica, T.; Hua, M.; Yakobson, B. I. *Proc. Natl. Acad. Sci. USA* **2006,** 103.

(6) Chopra, N. G.; Benedict, L. X.; Crespi, V. H.; Cohen, M. L.; Louie, S. G.; Zettl, A. *Nature* **1995,** 377.

(7) Yu, M.-F.; Lourie, O.; Dyer, M. J.; Moloni, K.; Kelly, T. F.; Ruoff, R. S. *Science* **2000,** 287.

(8) Xu, T.; Wang, Z.; Miao, J.; Chen, X.; Tan, C. M. *Appl. Phys. Lett.* **2007,** 91.

(9) Zhu, L.; Xu, J.; Xiu, Y.; Sun, Y.; Hess, D. W.; Wong, C. P. *Carbon* **2006,** 44.

(10) Zhang, L.; Balzano, L.; Resasco, D. E. *J. Phy. Chem. B* **2005,** 109.

(11) Bonard, J. M.; Salvetat, J. P.; Stockli, T.; de Heer, W. A.; Laszlo; Chatelain, A. *Appl. Phys. Lett.* **1998,** 73.

(12) Sveningsson, M.; Morjan, R. E.; Nerushev, O. A.; Campbell, E. B.; Malsch, D.; Schaefer, J. *Appl. Phys. Lett.* **2004,** 85.

(13) Jung, Y. J.; Kar, S.; Talapatra, S.; Soldano, C.; Viswanathan, G.; Li, X.; Yao, Z.; Ou, F. S.; Avadhanula, A.; Vajtai, R.; Curran, S. S.; Nalamasu, O.; Ajayan, P. M. *Nano Lett.* **2006,** 6.

(14) Bonard, J.-M.; Maier, F.; Stöckli, T.; Châtelain, A.; de Heer, W. A.; Salvetat, J.-P.; Forró, L. *Ultramicroscopy* **1998,** 73.

(15) Xu, N. S.; Chen, Y.; Deng, S. Z.; Chen, J.; Ma, X. C.; Wang, E. G. *J. Phys. D: Appl. Phys.* **2001,** 34.

(16) Ma, X. C.; Wang, E. G.; Zhou, W. Z.; Jefferson, D. A.; Chen, J.; Deng, S. Z.; Xu, N. S.; Yuan, J. *Appl. Phys. Lett.* **1999,** 75.

(17) Park, K. H.; Lee, S.; Kohb, K. H. *J. Appl. Phys.* **2006,** 99.

(18) Hofmann, S.; Ducati, C.; Kleinsorge, B.; Robertson, J. *Appl. Phys. Lett.* **2003,** 83.

(19) Kumar, A.; Pushparaj, V. L.; Kar, S.; Nalamasu, O.; Ajayan, P. M. *Appl. Phys. Lett.* **2006,** 89.

(20) Zhu, L.; Sun, Y.; Hess, D. W.; Wong, C.-P. *Nano Lett.* **2006,** 6.

(21) Jeong, T.; Heo, H.; Lee, J.; Lee, S.; Kim, W.; Lee, H.; Park, S.; Kim, J. M.; Oh, T.; Park, C.; Yoo, J.-B.; Gong, B.; lee, N.; Yu, S. *Appl. Phys. Lett.* **2005,** 87.

(22) Zhi, C. Y.; Bai, X. D.; Wang, E. G. *Appl. Phys. Lett.* **2002,** 81.

(23) Sun, T.; Wang, G.; Liu, H.; Feng, L.; Jiang, L.; Zhu, D. *J. Am. Ceram. Soc.* **2003,** 125.

(24) Li, H.; Wang, X.; Song, Y.; Liu, Y.; Li, Q.; Jiang, L.; Zhu, D. *Angew. Chem. Int. Ed.* **2001,** 40.

(25) Lau, K. K. S.; Bico, J.; Teo, K. B. K.; Chhowalla, M.; Amaratunga, G. A. J.; Milne, W. I.; McKinley, G. H.; Gleason, K. K. *Nano Lett.* **2003,** 3.

(26) Li, P.; Lim, X.; Zhu, Y.; Yu, T.; Ong, C. K.; Shen, Z.; Wee, A. T. S.; Sow, C. H. *J. Phy. Chem. B* **2007,** 111.

(27) Kim, B. M.; Sinha, S.; Bau, H. H. *Nano Lett.* **2004,** 4.

(28) Barber, A. H.; Cohen, S. R.; Wagner, H. D. *Phys. Rev. B* **2005,** 71.

(29) Mattia, D.; Rossi, M. P.; Kim, B. M.; Korneva, G.; Bau, H. H.; Gogotsi, Y. *J. Phy. Chem. B* **2006,** 110.

Chapter 5: Re-grown Aligned MWNTs with Improved Field Emission

5.1 Introduction

In this chapter, we present a simple yet efficient method of improving field emission properties of MWNTs via re-growing MWNTs on the same substrate after removal of the initial batch of MWNTs (1st generation). As-grown MWNTs were first grown on iron (Fe) coated Si substrates. Using a transfer technique previously discussed in Chapter 4, the as-grown MWNTs were transferred onto various substrates leaving the Fe catalyst on the Si substrate. The same substrate covered with the initial Fe catalyst was used to re-grow another batch of MWNTs under exactly the same conditions as the initial batch. Success in re-growing MWNTs (2nd generation) using the same Fe catalysts was attributed to the predominant root growth mechanism in MWNTs synthesized in our laboratory. Further characterizations were conducted using field emission scanning electron microscope (FESEM), atomic force microscope (AFM), transmission electron microscope (TEM) and Micro-Raman. Comparing both generations of MWNTs, upper regions and tips of the new batch of MWNTs were found to have a larger diameter distribution and were covered with sharp carbonaceous impurities. These sharp impurities, serving as new emission sites, brought about ~ 2.6 times improvement in the field enhancement factor. In addition, the turn-on field at 10 μA cm^{-2} of the 2nd generation was found to be 1.40 $V\mu m^{-1}$. This was much lower than that of the 1st generation, which had a turn-on field of 2.85 $V\mu m^{-1}$. On top of this improvement in field emission, we were also able to achieve more uniform emission surface from the 2nd generation of MWNTs.

5.2 Method to Recycle the Iron Catalysts

Before the 2nd generation of MWNTs can be synthesized on the same substrate, the 1st generation of MWNTs has to be removed. The removal or transfer of 1st generation of MWNTs was carried out using the method described in Chapter 4. Figure 5.1 illustrates the removal of the 1st generation (as-grown) of MWNTs from the original substrate. The remaining silicon (Si) substrate that was covered with Fe catalysts was used again for another round of MWNTs synthesis under the same growth conditions. To transfer the MWNTs, polydimethylsiloxane, PDMS, $((H_3C)_3SiO[Si(CH_3)_2O]_nSi(CH_3)_3)$ was first spin-coated over a thin layer of platinum (Pt) covered substrate. A sample of 1st generation of aligned MWNTs was then inverted and pressed onto the PDMS covered substrate. The samples were then cured in a hot oven. After curing, the Si substrate on which the 1st generation of MWNTs was grown could be easily removed. After removal, the Si substrate remained decorated with Fe catalysts. The same substrate was then sent for another round of synthesis using identical growth conditions.

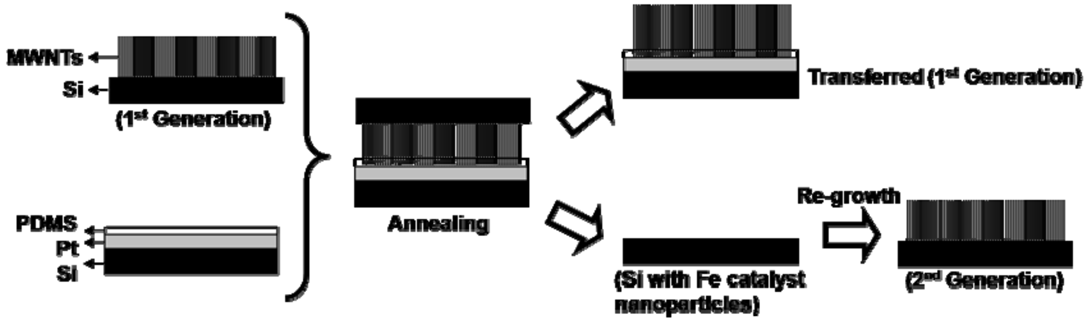

Figure 5.1 Schematic of preparing Si substrate such that the Fe catalyst on the substrate could be used to re-grow a 2nd generation of MWNTs.

While this method of removing the 1st generation of MWNTs managed to maintain the alignment and have good electrical contact as shown in Chapter 4, the success of the second round of MWNTs synthesis was very much dependent on ensuring that no PDMS came into contact with the Fe catalysts. In cases where PDMS remained coated onto the Fe catalysts, no MWNTs were successfully synthesized again. These observations were consistent with the previous report [1] that at least part of the catalyst had to be exposed to the carbon source for successful growth of MWNTs.

5.3 Growth Mechanism of MWNTs

MWNTs used in our experiments were synthesized in a plasma enhanced chemical vapour deposition (PEVCD) system. Growth of our MWNTs could be classified under catalytic based CVD synthesis and the overall growth process of MWNTs was described in the previous section. Synthesis of CNTs could generally be classified into two models, namely, the tip-growth and the root-growth model. In the tip-growth model, the catalyst particles are lifted off from the substrate during growth. On the other hand, catalyst particles of the root-growth model remain on the substrate. In this case, carbon atoms obtained from the decomposition of acetylene were absorbed into the catalyst to form a carbon-iron solid state solution. At super saturation, carbon atoms precipitate out from the particle and initiate the growth of the CNTs. In order for the re-growth experiments to be successful, MWNTs had to be synthesized using the root-growth mechanism. Otherwise, Fe catalysts would be transferred together with the MWNTs and thus, no MWNTs could be synthesized using the same substrate again.

From our previous work [2], MWNTs produced in our laboratory were grown by the root growth mechanism. This thus lays the basis for the success of the MWNTs re-growth experiment as Fe catalysts remained on the Si substrate upon removal of the 1st generation of MWNTs. AFM characterizations of the Fe catalysts coated Si substrates before growth and after removal of MWNTs were carried out.

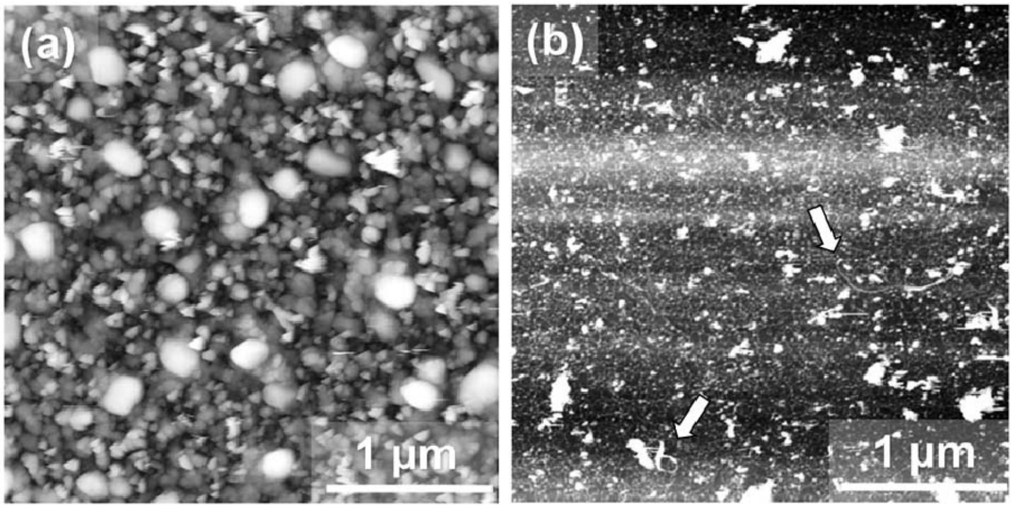

Figure 5.2 AFM images of (a) Fe catalysts on Si substrate after heating at 700 ^{o}C followed by cooling to room temperature in vacuum; (b) Fe catalysts and some broken MWNTs (indicated by the arrows) remaining on Si substrate after transfer.

Figure 5.2a shows AFM images of Fe catalysts formation after the Fe coated Si substrates had undergone heating at 700 ^{o}C. Similarly, Figure 5.2b showed AFM images of Fe catalysts formed after 1st generation of MWNTs had been transferred. From Figure 5.2a, the number density of the Fe catalysts was found to be 1.63 x 10^{13} particles mm^{-2}, whereas that of the Fe catalysts remaining on the Si substrate after transfer (Figure 5.2b) was 1.42 x 10^{14} particles mm^{-2}. Thus, this Fe coated surface is suitable for the re-growth of MWNTs.

5.4 Diameter Distributions of 1st and 2nd Generation of MWNTs

Further studies were conducted on both generations of MWNTs using the FESEM. 20 images (10 for each generation of MWNTs) at similar magnifications were obtained. Figure 5.3(a,b) shows examples of top-view FESEM images of the 1st and 2nd generations of MWNTs used to obtain the diameter distribution histograms shown in Figure 5.3c.

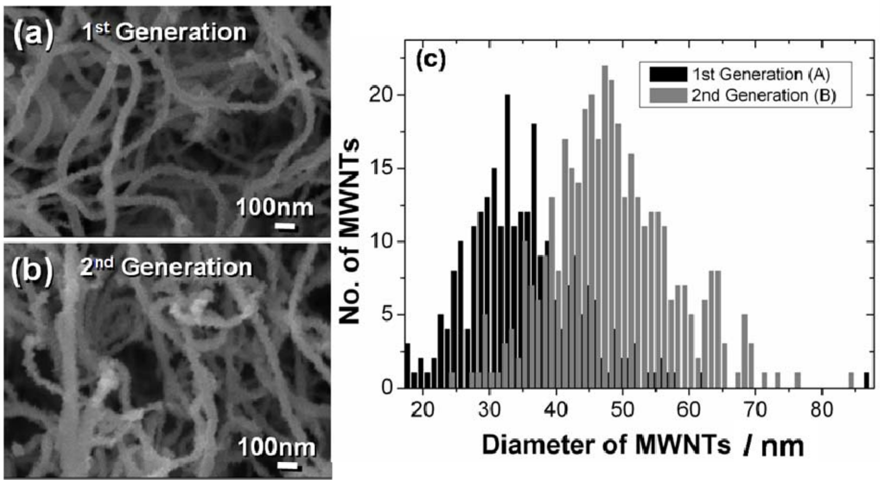

Figure 5.3 Top-View FESEM images of (a) 1st generation and (b) 2nd generation of MWNTs. (c) Diameter distribution of top-view MWNTs.

From Figure 5.3c, a shift in the distribution towards larger diameter is observed for the 2nd generation MWNTs. The shift involved a change in mean distribution from 35 ± 9 nm to 48 ± 9 nm. This trend is in contrast to that reported by Chiu *et al.* [3] who found that their MWNTs tend to shrink in diameter after subsequent re-growth. Such a difference in observations is attributed to the fact that both the experimental processes were different. Chiu *et al*. used an hour of thermal annealing of their substrate to remove any amorphous carbon on the catalyst as well as to burn off the initial growth of CNTs; no such treatment was conducted on the substrates used in our experiment upon transferring of MWNTs.

Similar studies of the distributions of the diameter of MWNTs near the Si substrates were conducted. In this case, another set of 20 FESEM images of the side-view of both generations of MWNTs with same magnification were obtained. Likewise, 10 images for each generation of MWNTs were obtained. Figure 5.4(a,b) show typical FESEM images from which the diameter distribution histogram in Figure 5.4c was generated. Based on our observations, MWNTs grown in our lab tend to be more entangled nearer to the top surface. To ensure a fair comparison for the distributions, we obtain the side-view FESEM images from similar regions (insert in Figure 5.4c), nearer to the substrate. Minimal changes in the diameter distribution of both generations were observed with the mean value for both histograms located at 19 ± 4 nm.

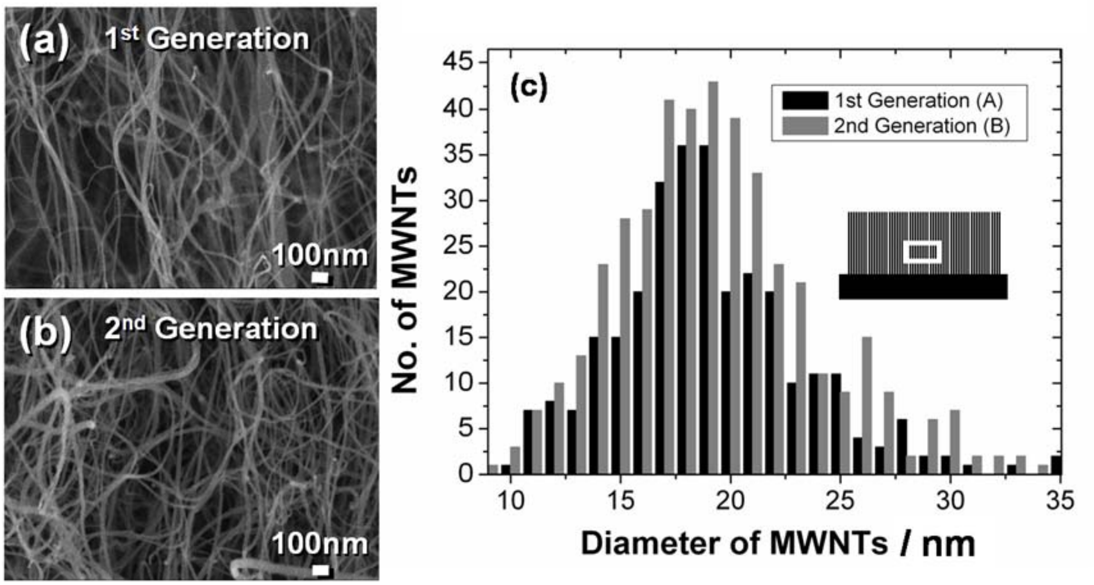

Figure 5.4 Side-View FESEM images of (a) 1st generation and (b) 2nd generation of MWNTs. (c) Diameter distribution of side-view MWNTs (insert shows region on the MWNTs samples where (a) and (b) were taken).

Comparing Figure 5.3c and 5.4c, the MWNT diameter reduces from 35 ± 9 nm (top) to 19 ± 4 nm (side) for 1st generation of MWNTs and 48 ± 9 nm (top) to 19 ± 4 nm (side) for the 2nd generation. Based on the results shown in Chapter 4, 1st generation MWNTs near the Fe catalysts, ie., the base, were found to be cleaner and contained fewer defects than the top region of the MWNTs. In addition, long-duration of growth could also result in MWNTs being covered by a layer of amorphous carbon at the top of the MWNTs [2-4]. Thus, defects and amorphous carbon could be the reasons behind the difference in top and bottom diameter for both generations of MWNTs.

5.5 Length of 1st and 2nd generation of MWNTs

Using the cross-sectional view of FESEM for analysis, the length of the 1st generation of MWNTs (Figure 5.5a) was found to be twice as long as that of the 2nd generation (Figure

5.5b). Such a difference could be attributed to the following reasons. Firstly, the amorphous carbon surrounding the recycled Fe catalysts might not be removed completely via plasma etching during the initial phase of MWNT growth. Based on a previous study by K. Hata *et al.* [5], the amorphous carbon could restrict the activity of catalysts and in this case reduce the efficiency of MWNTs growth despite using identical growth conditions and durations for both generations [5]. Secondly, applying too much pressure on the 1st generation of MWNTs during transfer could cause some PDMS to be in contact with the Fe catalysts, thus affecting the effectiveness of the catalysts and resulting in shorter 2nd generation of MWNTs. Thirdly, MWNTs with defects at the root portion would dislocate at these defective points due to axial stress [6] and remain attached to the Fe catalysts as indicated by the arrows shown in Figure 5.2b. The remaining MWNTs could thus be a factor hindering the growth of the 2nd generation of MWNTs.

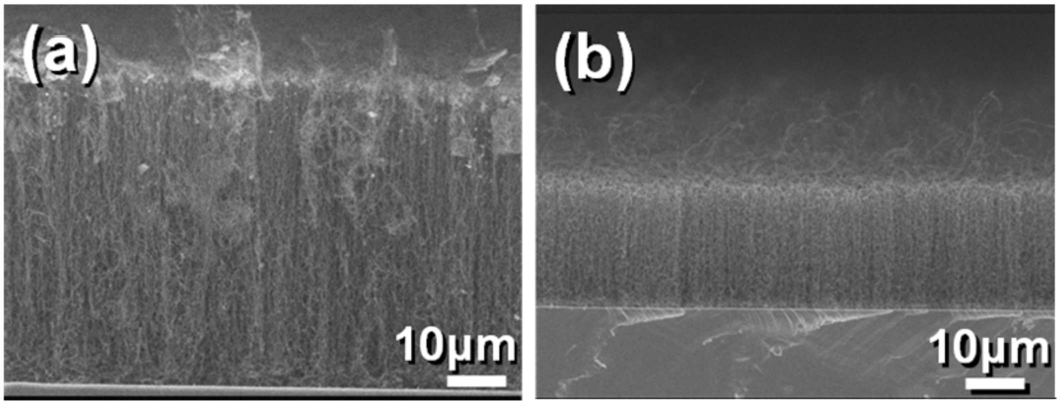

Figure 5.5 Side-View FESEM images showing the length of (a) 1st generation MWNTs and (b) 2nd generation MWNTs.

5.6 TEM Study of the 1st and 2nd generations of MWNTs

TEM investigations were carried out on both sets of samples. MWNTs samples were scratched onto a nickel (Ni) TEM grid. By doing so, we were able to obtain TEM images of the top and near root region of the respective generations of MWNTs.

Figure 5.6a shows TEM images of 1st generation MWNTs. Higher magnification of the same generation of MWNTs is shown in Figure 5.6b. As observed from Figure 5.6b, a thin layer of amorphous carbon could be seen surrounding the MWNTs. Figure 5.6(c,d) show low and higher magnification TEM images of the 2nd generation MWNTs, respectively. Comparing Figure 5.6b and 5.6d, a significant change in the morphology of the 2nd generation of MWNTs could be observed as a rough layer of coating was found covering both the amorphous carbon layer and the 2nd generation of MWNTs. Based on the comparison, the origin of the increased diameter of the 2nd generation MWNTs as seen in Figure 5.3c could be associated to the rougher layer of coating.

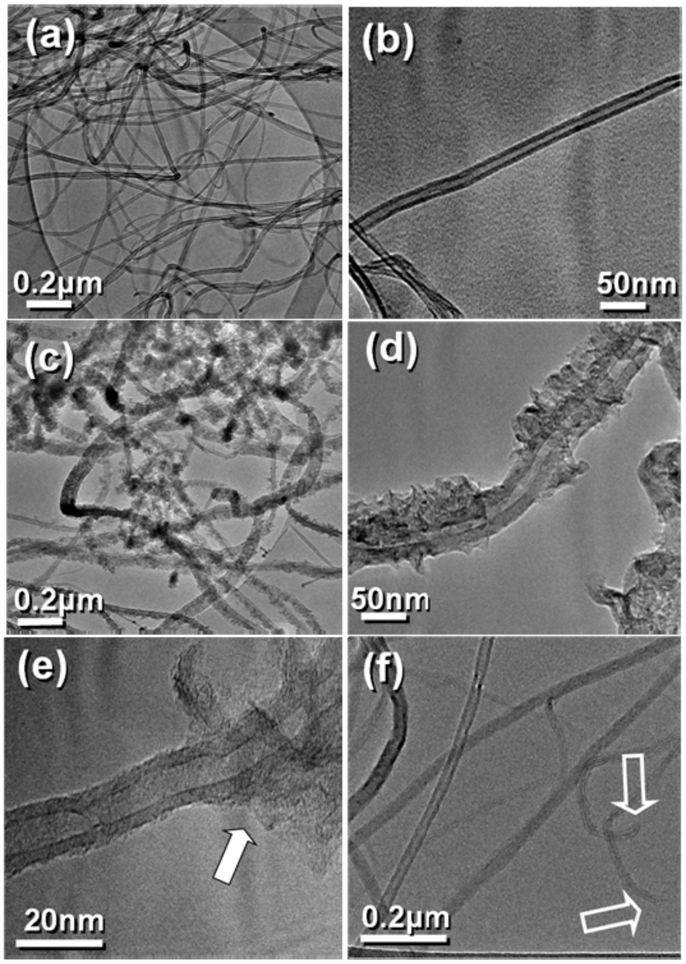

Figure 5.6 TEM images of (a) 1st generation MWNTs with higher magnification shown in (b); (c) 2nd generation MWNTs with higher magnification shown in (d); (e) single strand of 2nd generation MWNT at the junction where no more oxide and Fe particles (indicated by the block arrow) are covering the MWNT and (f) the end region of the 2nd generation of MWNTs (hollow arrows indicating opened end of MWNTs).

Figure 5.6e shows a TEM image of 2nd generation MWNT near the root. From this figure, part of the MWNT was covered with the rough outer layer of Si, O and Fe particles (indicated by the block arrow) while the remaining half were covered by amorphous carbon. On one hand, as the MWNTs grew from the Fe catalysts, loose Fe particles were found to detach from the catalyst and wrap themselves around the MWNTs. On the other hand, once all the loose Fe particles were removed from the catalysts, the remaining MWNTs would be synthesized with the usual amorphous carbon coating as shown in Figure 5.6f. Hollow arrows in Figure 5.6f indicate open ends of MWNTs. In addition, similar diameter distributions for both generations shown in Figure 5.4c imply that the 2nd generations MWNTs were indeed synthesized from the remaining Fe catalysts on the substrate. The TEM observations could thus explain the 2.5 times difference in mean diameter distributions between the top and bottom sections of the 2nd generation of MWNTs.

From the energy dispersive x-ray (EDX) spectra shown in Figure 5.7 below, the rough outer layer surrounding the 2nd generation of MWNTs was a combination of O, Si and Fe particles. Nickel (Ni) and copper (Cu) peaks were attributed to both the Ni TEM grid and the Cu TEM grid holder. The EDX result reveals that in the process of the second growth, some Fe particles could have separated from the Fe catalysts and encompassed the MWNTs as they grew from the Fe catalysts. As a result, the diameter of the 2nd generation would thus be larger than that of the 1st generation as verified in Figure 5.3c. Moreover, with lesser Fe catalyst in the regrowth of MWNTs, it was thus reasonable to have a less efficient second round of MWNTs synthesis at the same growth condition. The Si and O peaks observed in the spectrum are attributed to the presence of PDMS on the catalysts. This observation thus verified the previous hypothesis that applying too much pressure could cause some PDMS to be in contact with the Fe catalysts and hence hinder the growth of the MWNTs.

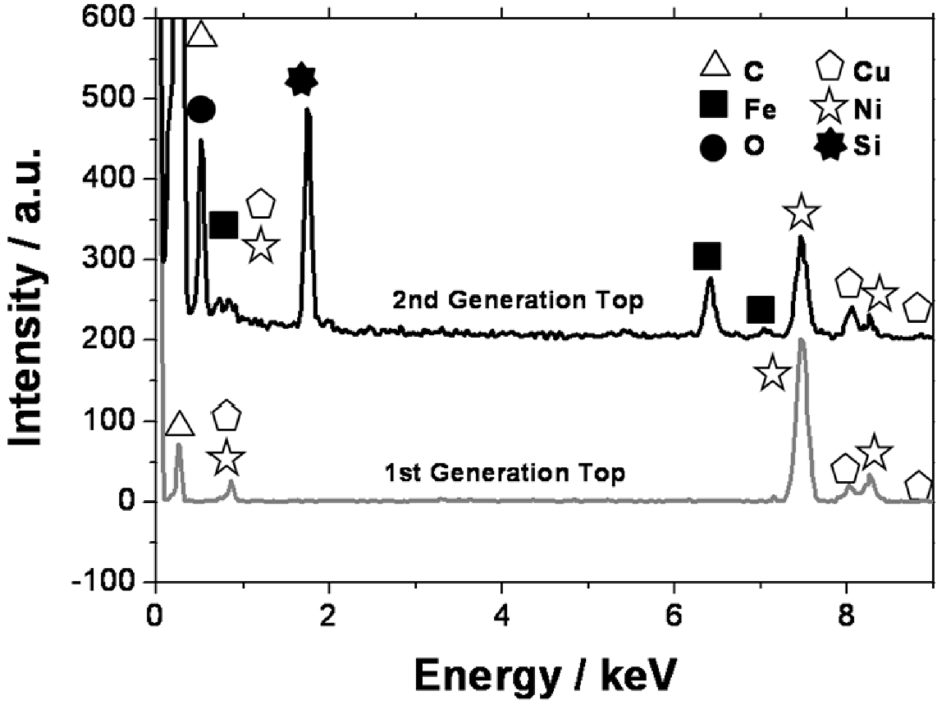

Figure 5.7 EDX of the top region of 1st and 2nd generation of MWNTs. The spectrum for the 2nd generation of MWNTs was offset for clarity.

5.7 Micro-raman Analysis of 1st and 2nd Generation of MWNT

The Micro-Raman spectra shown in Figure 5.8 have two main peaks at ~1354 cm^{-1} and ~1593 cm^{-1}. These peaks could be identified as the D and G bands of MWNTs. The D band is an indicator of disorder or amorphous carbon and the G band corresponds to ordered graphite in MWNTs [7]. From the figure, it could be observed that both position and shape of the Micro-Raman spectra obtained for both the 1st and 2nd generations of MWNTs are similar. However, the ratio of D band intensity to that of G band increased from 1.09 to 1.19. This ratio is an indication of the amount of disorder in the nanotube material [8]. Thus the Micro-Raman spectra suggested that there were more carbonaceous impurities [9] on the top surface of the 2nd generation MWNTs as compared to the 1st.

This finding is consistent with the results obtained using both FESEM and TEM analysis of the samples.

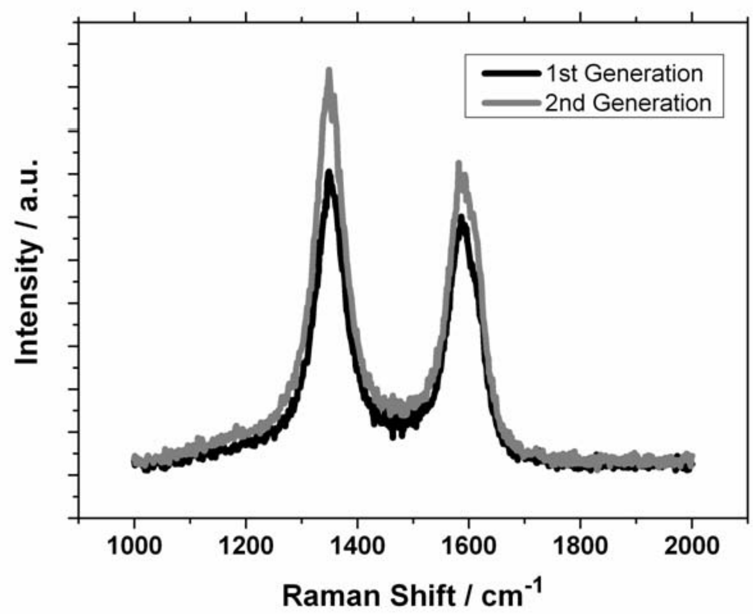

Figure 5.8 Micro-Raman spectra from the surface of 1st and 2nd generation of MWNTs.

5.8 Field Emission and UPS Characterization of the 1st and 2nd Generations of MWNTs

To compare the electrical properties of both generations of MWNTs, field emission (FE) characterization was carried out on both set of samples (at room temperature) using a two-parallel plate arrangement in a vacuum chamber with a base pressure of 4 x 10^{-6} Torr. FE measurements for each sample were conducted by securing the sample to a copper (Cu) substrate cathode using a Cu double-sided tape. In the setup, indium tin oxide (ITO) glass coated with a layer of phosphor acted as the anode. A 200 µm thick polymer film with a square opening was employed as a spacer between the electrodes. The voltage across the electrodes was increased in steps of 10 V up to a maximum of 850 V. The corresponding emission current was measured using a Keithley 237 high-voltage source measure unit (SMU) repeatedly till there was no more variation in repeated measurement.

Figure 5.9a shows a typical plot of measured FE current density, J (mA cm^{-2}) as a function of applied electric field, E (Vμm^{-1}). For the case of the 1st generation, the turn-on field that produced a current of 10 μA cm^{-2}, was found to be ~ 2.85 Vμm^{-1} and an applied field of 4.25 Vμm^{-1} was required to bring about an emission current density of 0.94 mA cm^{-2}. Looking at the 2nd generation of MWNTs, the turn-on field in this case was ~ 1.40 Vμm^{-1} and the applied field required to produce an emission current density of 0.81 mA cm^{-2} was 2.25 Vμm^{-1}. Based on the results obtained, 2nd generation of MWNTs were able to produce similar amount of emission current while requiring ~ 50% less applied electric field as compared to the 1st generation. In addition, at 2.75 Vμm^{-1}, the FE from the 2nd generation of MWNTs was found to be more uniform when compared to the 1st generation as justified by the fluorescence images shown in Figure 5.9(b,c). Note that the fluorescence images were obtained from a different set of MWNTs samples with the same trend of FE results as those presented, thus proving that the results were repeatable.

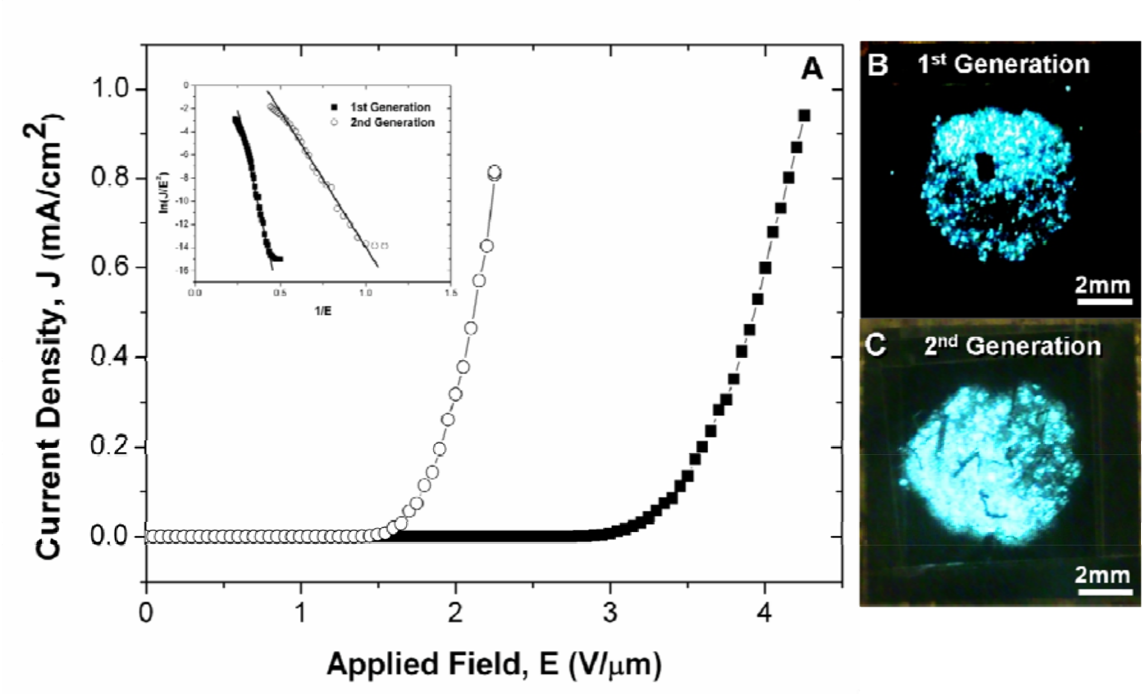

Figure 5.9 (a) Field emission measurements of both 1st and 2nd generation MWNTs taken in room temperature. Insert shows the respective FN plot. Fluorescence images obtained during field emission from the (b) 1st generation and (c) 2nd generation of another set of MWNTs.

The relation between the emission current density, J (Acm^{-2}) and the electric field, E (Vμm^{-1}), is given by the Fowler-Nordheim (FN) equation:

$$J = \frac{AF^2}{\varphi}\exp\left(-\frac{B\varphi^{3/2}}{\beta E}\right) \tag{5.1}$$

where F (= βE) is local electric field (Vcm^{-1}), β is the enhancement factor, φ is the work function (eV), A and B are constants with respective values being 1.4 x 10^{-6} AeVV^{-2} and 6.44 x 10^{3} VeV$^{-3/2}$cm^{-1}.

A plot of ln(J/E^2) with respect to 1/E inserted in Figure 5.9 shows respective FN plots of both generations of MWNTs. Linearity of the FN plot is used as an indication that the emission current originates from the quantum tunneling effect [10]. While the FN plots in the insert showed linear fit at low electric field, deviations at higher electric field was observed. Such non-linearity of the FN plots were frequently related to issues such as different enhancement factors within emitters [11], space charge effect [12] and non-uniform local field near the tip of MWNTs [13].

From the UPS data shown in Figure 5.10, there were no observable differences in the work function of both generations of MWNTs as could be observed from the cutoff point of the spectra. By extrapolating the cutoff point of the spectra (enclosed in the circle), the work function of both generations of MWNTs was found to be 4.2 eV as shown in the insert in Figure 5.10.

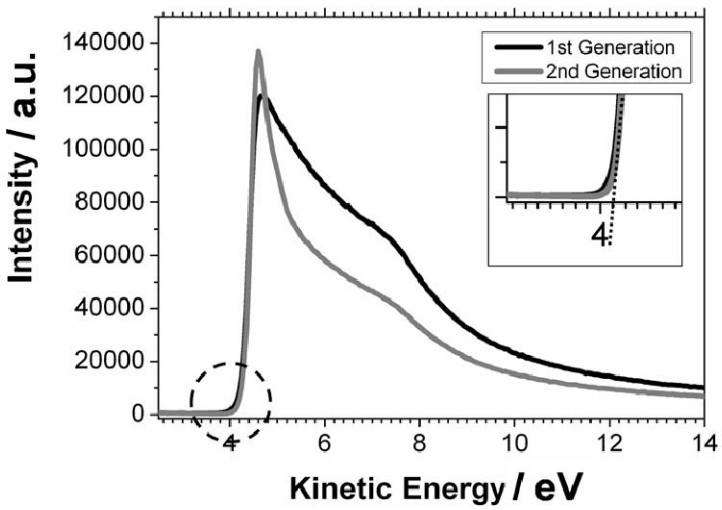

Figure 5.10 UPS data showing no changes in work function upon comparison between both generations of MWNTs. Insert shows that work function of both generations of MWNTs had the same value of 4.2eV as obtained by extrapolating the cut off point (enclosed in the circle) to the horizontal axis.

Using the value of work function obtained above together with the gradients of the FN plots, the enhancement factor β. of the 1st generation MWNTs and 2nd generation MWNTs was found to be 998 and 2614 respectively. The field enhancement factor of the

2nd generation of MWNTs was found to be ~ 2.6 times more than that of the 1st generation. From the above results, the simple technique of transferring and re-growing MWNTs is able to produce MWNTs with better field emission properties as compared to the 1st generation of growth. Possible reasons for such a significant improvement of FE property could be associated to the presence of pointed carbonaceous impurities surrounding the tip and upper portion of the 2nd generation of MWNTs shown in the FESEM, TEM and Micro-Raman analyses. Given no changes in work function as determined using UPS, these sharp edges added to the original morphology of the MWNTs could provide more effective emission sites and, as a result, enhance the current density [14].

5.9 Conclusion

Re-grown MWNTs from the same substrates, after the 1st generation of MWNTs was transferred onto other substrates (using PDMS as intermediation), were found to exhibit better field emission properties as compared to the 1st generation of MWNTs. Field emission studies of the MWNTs showed ~ 2.6 times improvement in terms of the enhancement factor from the 2nd generation of MWNTs. The significant improvements were attributed to sharp impurities surrounding the tip and upper portion of the 2nd generation of MWNTs as verified using FESEM, TEM and Micro-Raman analyses. With the use of this re-growth technique, MWNTs may turn out to be better field emission candidate for various potential applications.

References

(1) Helveg, S.; Lopez-Cartes, C.; Sehested, J.; Hansen, P. L.; Clausen, B. S.; Rostrup-Nielsen, J. R.; Abild-Pedersen, F.; Norskov, J. K. *Nature* **2004,** 427.

(2) Lim, K. Y.; Sow, C. H.; Lin, J. Y.; Cheong, F. C.; Shen, Z. X.; Thong, J. T. L.; Chin, K. C.; Wee, A. T. S. *Adv. Mater.* **2003,** 15.

(3) Chiu, C. C.; Yoshimura, M.; Ueda, K. *Jap. J. Appl. Phys.* **2008,** 47.

(4) Huang, S. M.; Dai, L. M. *J. Phys. Chem. B* **2002,** 106.

(5) Hata, K.; Futaba, D. N.; Mizuno, K.; Namai, T.; Yumura, M.; Iijima, S. *Abstracts of Papers of the American Chemical Society* **2005,** 229.

(6) Chopra, N. G.; Benedict, L. X.; Crespi, V. H.; Cohen, M. L.; Louie, S. G.; Zettl, A. *Nature* **1995,** 377.

(7) Belin, T.; Epron, F. *Mater. Sci. Eng. B-Solid State Materials for Advanced Technology* **2005,** 119.

(8) Zhang, J. H.; Feng, T.; Yu, W. D.; Liu, X. H.; Wang, X.; Li, Q. *Diamond Rela. Mater.* **2004,** 13.

(9) Uh, H. S.; Lee, S. M.; Jeon, P. G.; Kwak, B. H.; Park, S. S.; Kwon, S. J.; Cho, E. S.; Ko, S. W.; Lee, J. D.; Lee, C. G. *Thin Solid Films* **2004,** 462-63.

(10) Bonard, J. M.; Salvetat, J. P.; Stockli, T.; de Heer, W. A.; Forro, L.; Chatelain, A. *Appl. Phys Lett.* **1998,** 73.

(11) Park, K. H.; Lee, S.; Koh, K. H. *J. Appl. Phys.* **2006,** 99.

(12) Xu, N. S.; Chen, Y.; Deng, S. Z.; Chen, J.; Ma, X. C.; Wang, E. G. *Journal of Physics D-Applied Physics* **2001,** 34.

(13) Buldum, A.; Lu, J. P. *Phys. Rev. Lett.* **2003,** 91.

(14) Chiu, C. C.; Tsai, T. Y.; Tai, N. H. *Nanotechnology* **2006,** 17.

Chapter 6: Capillarity-Assisted Assembly of CNTs Microstructures with Organized Initiators

6.1 Introduction

In this chapter, three techniques involving solvent assisted-assembly of CNTs are presented. The first technique describes the creation of negative CNTs structures via the use of water and a continuous laser beam of varying laser power. Subsequently, an in-depth analysis of the effect of oxidization, density and laser power induced artificial vacancies on the assembly of CNTs would be investigated. In addition, real-time study of the formation process of the negative CNTs structures under fluorescence microscopy would also be conducted. In doing so, a better understanding of the dynamics involved in the formation of the negative structures would be achieved. The second technique presents water assisted large scale assembly of top gathering pillar arrays made out of CNTs. This new technique could possibly serve as an additional set of tools for further developments in controlling the architecture of the CNTs on the substrates for the creations of future CNTs based devices and packing systems. Lastly, a dip-dry method involving the use of ethanol to pack large scale CNT strips onto the substrate surfaces is introduced. Detailed I-V measurements of the packed CNT strips were also investigated.

6.2 Negative MWNTs Microstructures

6.2.1 Laser Power Dependent Study

Previous work by Liu *et al.*[9] reasoned the existence of a greater value of hydrostatic dilation stress in the higher density regions of the CNTs compared to that at the lower density regions. Due to this difference, CNTs were flattened outward from a region of lower CNTs density while "walls" were formed when CNTs collapsing in opposite directions meet. Thus, negative structures could be constructed through the introduction of artificial sites with even lower density than those found naturally in the CNT arrays.

To verify such a phenomenon, a continuous focused laser beam was used to create artificial vacant sites on vertically aligned multi-walled carbon nanotube (MWNT) arrays by releasing the laser intermediately with a shutter. Subsequently, the patterned MWNTs array was transferred onto a transparency using PDMS as intermediation via a process described in the Chapter 4. In doing so, the hydrophilic substrate surface was completely covered by PDMS and part of the MWNTs was embedded in the PDMS. This thus prohibited any formations of the hydrostatic dilation stress and any bending of MWNTs was prevented as they were embedded in the polymer. As a result, no MWNT polygons were formed (Figure 6.1) even after the introduction of water as the assembly solvent. The result thus emphasized the importance of the presence of hydrostatic dilation stress in the formation process of the MWNT polygons.

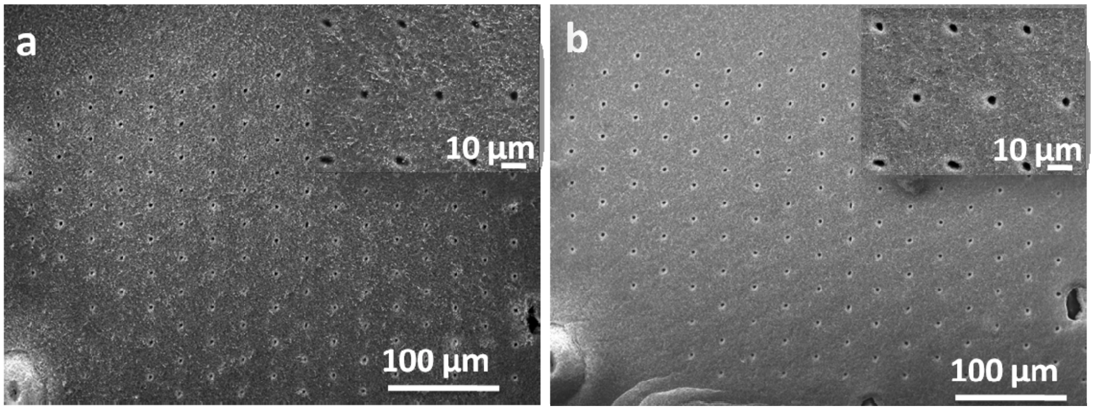

Figure 6.1 SEM images showing artificial vacancies created onto transferred MWNT arrays (a) before and (b) after the introduction of water as assembly agent.

With that as the basis, effects of the depth and area of the vacant sites on the formation of the negative structures were investigated. Depths of the vacant sites were changed by varying the laser power, from 50 mW to 27 mW. In doing so, the diameter of the laser induced vacancies changes from 13.0 ± 0.2 µm to 6.4 ± 0.1 µm with height varying from 22.4 µm to 16.2 µm. Similar patterns of vacant sites were created on the same MWNTs samples with Figure 6.2a showing similar pattern formed using only 50 mW laser power while Figure 6.2b was obtained with 27 mW laser power. Figure 6.2c shows a mixture of sites created using 50 mW (larger holes) and 27 mW (smaller holes). By introducing distilled water onto the surfaces of oxidized patterned MWNTs surfaces, different negative structures due to the use of different laser power could be observed. Formations of the hexagonal structures shown in Figure 6.2d and Figure 6.2e were consistent with the proposed mechanism that the "wall" of the polygon would form approximately at the vertical bisector of two adjacent vacancies shown in Figure 6.2a and Figure 6.2b.[9] However, through varying the laser power, such phenomenon was only observed between vacancies created using the same laser power. The “wall” of the polygon was no longer positioned at the bisector of two adjacent vacancies created using different laser power as shown in Figure 6.2f.

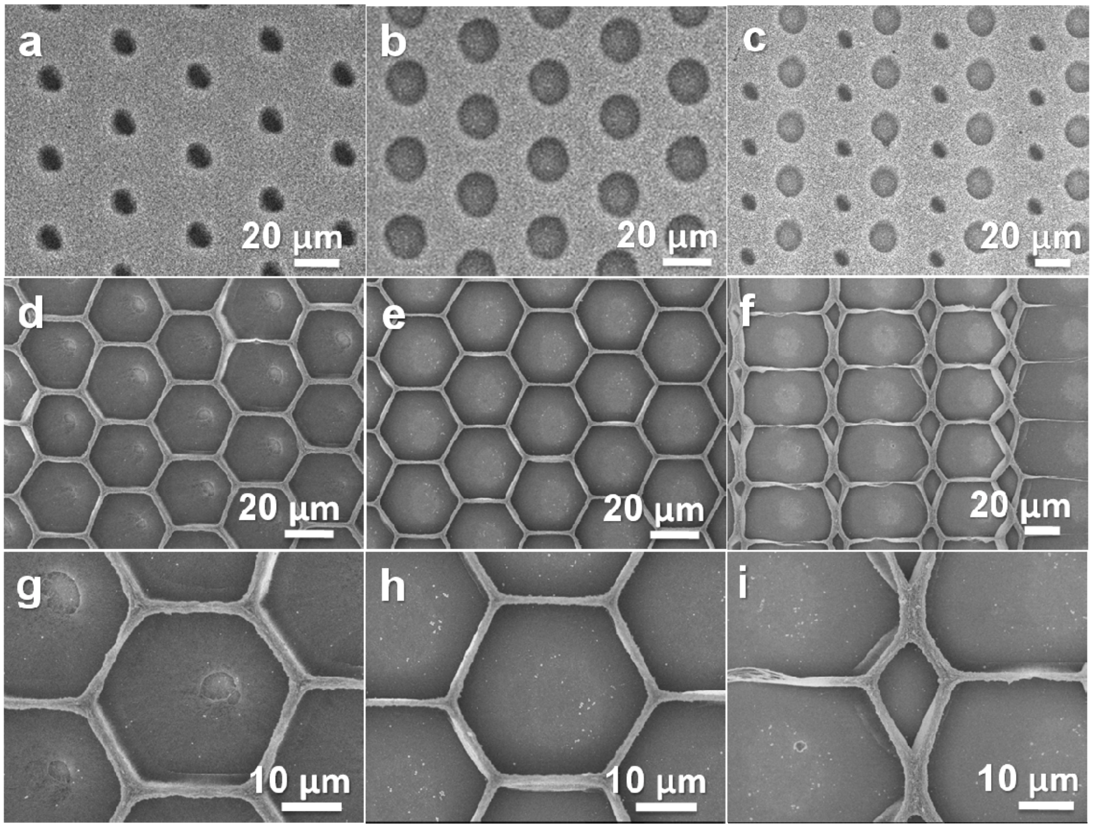

Figure 6.2 SEM images of same vacant sites created using (a) 27 mW and (b) 50 mW and (c) a mixture of both laser power before water assisted assembly. After water assisted assembly, (d, e) show “walls” of the polygons forming approximately at the vertical bisector of two adjacent vacancies while (f) show a shift in the positions of the polygon “walls”. (g-i) show larger magnfications of the individual polygons formed in (d-f).

A possible explanation could be as follows: due to the use of higher laser power, more MWNTs were removed from the surfaces as compared to those formed using lower laser power. Thereby creating an area of lower density (or larger vacancies) than those formed via lower laser power. Owing to such differences in density, the base of the smaller vacancies was mostly covered with bent MWNTs (Figure 6.2g) whereas majority of the base from the larger vacancies shows more Si substrates (insert of Figure 6.2h). Lower hydrostatic dilation stress existing in the larger vacancies, due interactions with the larger area of exposed Si substrate, would overcome those from the smaller vacancies. Hence, with similar amount of water and evaporation time, bending of MWNTs out from the center of the larger vacancies would occur over a larger distance. It was due to such variations in distance that shifted the positions of the polygon "wall" from the bisector of two adjacent vacancies (Figure 6.2i).

In addition to the shift in the positions of the polygon "walls", the polygon "walls" shown in Figure 6.2d were less compact as compared to those in Figure 6.2e. Such difference in the degree of packing of the polygon "walls" could be related to the extent of the hydrostatic dilation stress experienced in both larger and smaller vacancies. With distance between two larger vacancies being the same that those between two smaller vacancies, larger hydrostatic dilation stress experienced in the larger vacancies would cause the MWNTs making up the polygon "walls" to be more compacted as compared to those between the smaller vacancies.

6.2.2 Density Dependent Study

To verify the density dependence of the formations of these polygons, similar vacancies pattern shown in Figure 6.3b was created on MWNTs using 50 mW laser power with MWNTs density ranging from 0.95 x 10^9 MWNT/cm^2 (Figure 6.3a), 1.87 x 10^9

MWNT/cm^2 (Figure 6.3b) and 2.04 x 10^9 MWNT/cm^2 (Figure 6.3c). The respective polygons formed after water-assisted assembly were as shown in Figure 6.3(d-f) with Figure 6.3(g-i) showing higher magnification of the corresponding individual polygon. From the MWNTs with the lowest density (Figure 6.3d), small cracks were observed to form in between the polygon "walls" due to presence of many low density regions . In the case of MWNTs with higher density (Figure 6.3f), limitations to the packing of the polygon "walls" were observed.

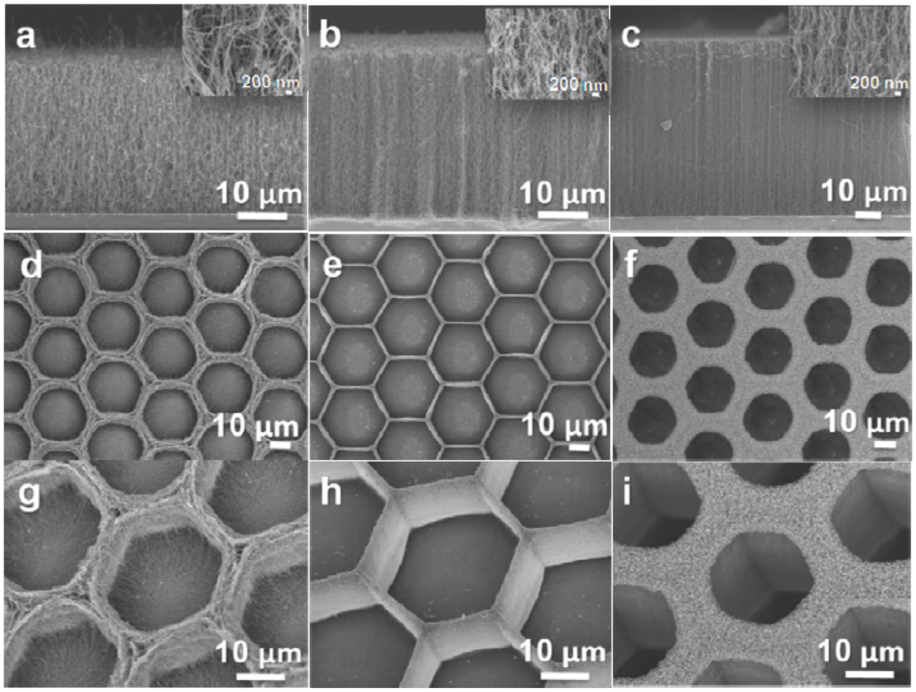

Figure 6.3 SEM images of same vacant sites created using 50mW laser power on MWNTs with different density, (a) 0.95 x 10^9 MWNT/cm^2; (b) 1.87 x 10^9 MWNT/cm^2 and (c) 2.04 x 10^9 MWNT/cm^2. (Inserts show higher magnifications of the MWNTs) The respective polygons form on the MWNTs after interaction with water was as shown in (d-f). (g-i) show higher magnifications of individual polygon taken at an angle of 25.0^o.

In the process of the formation of the polygons, more force was required to bend the densely packed MWNTs as compared to the loosely packed MWNTs in Figure 6.3a. Given the same amount of water, hence similar time restriction, there was insufficient time for the polygons to form. Moreover, unlike the sample shown in Figure 6.3d, no smaller cracks were observed to form in the polygon walls as the artificial sites produce much lower density as those found naturally on the MWNTs sample. Based on the results, an ideal density for the formation of polygons would be expected to exist between 0.95×10^9 MWNT/cm^2 and 2.04×10^9 MWNT/cm^2. Using MWNTs with density of 1.87×10^9 MWNT/cm^2 (Figure 6.3b), polygons with well packed walls were obtained (Figure 6.3e).

6.2.3 Oxidation Dependent Study

Based on previous studies, exposure to oxygen plasma readily converts hydrophobic MWNTs into hydrophilic ones. Using laser trimming to remove the top layer of the oxidized MWNTs, the hydrophilic surface would revert to being hydrophobic.[12] Hence by changing the sequence of oxidation after (Figure 6.4a) and before (Figure 6.4b) the creation of artificial vacant sites, different types of polygons were formed. From Figure 6.4a, polygons with the base covered with flattened MWNTs were observed as compared to the aggregations of MWNTs at the center of the polygons for MWNTs with vacancies created after oxidation (Figure 6.4b). When vacancies were created before oxidation, oxygen ions would be able to functionalize the interior of the vacancies, thereby allowing smooth flow of water into the vacancies as illustrated in the insert of Figure 6.4a. Reversing the process, the vacancies created after oxidation would revert to being hydrophobic. With a hydrophilic top surface, water was able to spread across the MWNTs surface. Assisted by gravity, water was able to sip into the vacancies. However, at the base of the vacancies, formations of air pockets due to hydrophobic nature of the MWNTs hindered the creation of a hydrostatic dilation stress as no interactions between the water and the substrate could occur at the center of the vacancies. Hence clustering of MWNTs at the center of the vacancies would occur together with packing of MWNTs along the polygon "walls".

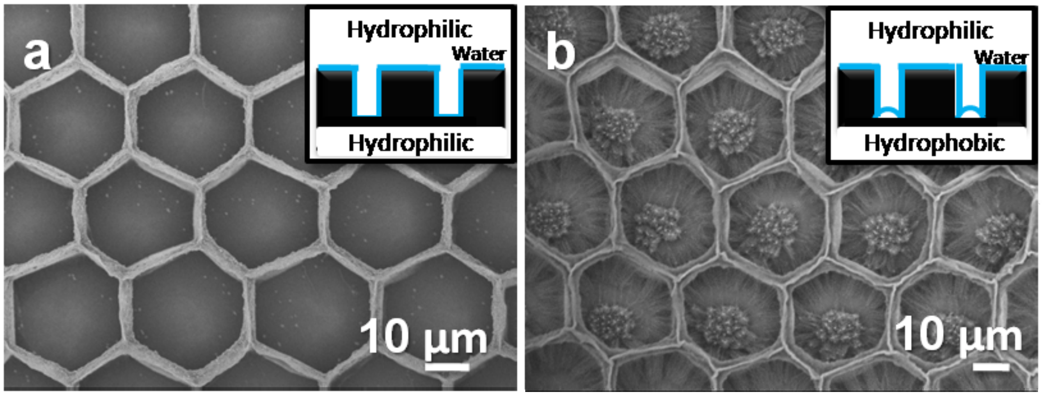

Figure 6.4 SEM images of capillary-assisted MWNT patters on samples with vacant sites created using focused laser (50mW) on MWNTs with (A) prior and (B) post oxidation. Inserts show proposed mechanisms for the formations of different types of MWNTs polygons.

6.2.4 Effect of Capillarity Forces on the Formations of Microstructures under Fluorescence Microscope

All the above studies were conducted with the samples kept in an upright position and a water droplet was placed on the surface of the MWNTs. As such, both gravitational and capillarity effect would occur in the opposite direction to the normal of the MWNTs surface. Hence, allowing the formations of hydrostatic dilation stress due to interactions between water and the MWNTs substrates. While this is a method well received in the study of water assisted assembly of MWNTs,[8, 9, 13, 14] an interesting phenomenon would be to investigate on the how competition between gravitational and capillarity effect could affect the formations of these MWNTs polygons. To do so, a droplet of quantum dot (QD) mixture in water was placed onto the patterned MWNTs sample and the sample was inverted. The real time formation process of the MWNTs polygons was captured under Fluorescence Microscopy (FM). With the presence of optically active QDs, the formation dynamics of the polygons was revealed readily with FM.

Figure 6.5(a-l) show snap shots from the real time video captured. Detailed analysis was conducted on vacancies marked I, II and III enclosed within the dotted rectangle in Figure 6.5a. Initially, all three regions remained black even though the QDs mixture had already covered the vacancies. This could be attributed to the effect of gravity working against capillary forces. However, after 1 sec, Region III (Figure 6.5b) appeared orange. This was taken as an indication of capillary forces overcoming that of gravitational forces as the QDs mixture began to flow into the artificial vacancies. After 11s (Figure 6.5c), saturation of QDs occur in Region III and the color within the vacancies changed from orange to yellow. At the same time, Region II began to be filled with QDs. Hence, similar orange tone as those seen in Region III of Figure 6.5b could be observed. While saturation of Region III remained constant for the following 5 sec, Region II continued to be filled with the orange QDs, without achieving the saturation point, as shown in Figure 6.5d. At 1 min 35 sec (Figure 6.5e), three shades of colors could be observed with Region

III being illuminated with a shade of yellow, Region II with orange and though Region I was slightly filled with the QDs, it remained as a darker shade of orange. The series of images shown in Figure 6.5(f-h) revealed that for a duration of 49 sec, no further filling of the vacancies occurred. Such consistence could be associated with QDs being drawn to fill the natural vacancies existing between the MWNTs. Evidence of such filling could be seen by comparing Region III shown in Figure 6.5e and Figure 6.5(f-h), the shade of yellow appeared dimmer than before. Hence implying a reduction in concentration of QDs as capillary forces pulls the QDs into the natural vacancies within the MWNTs.

Subsequently, evaporation of the solvent took place as Region II reappeared as black in Figure 6.5i. As the evaporation proceed, 59 sec later (Figure 6.5j), Region III reappeared as black too. Eventually, the MWNTs polygons were formed as the mixture evaporates completely (Figure 6.5(k-l)). The process of the formation of the MWNT polygons as the water evaporates were found to be similar to those observed when the MWNTs sample was kept in an upright position.[8]

Based on the above study, the whole formation process of the MWNT polygons in an inverted position could be divided into three sections. Namely, (i) the filing process where the QDs mixture filled up the vacancies; (ii) saturation process where QDs were pulled by capillary forces to fill up the natural vacancies in the MWNTs and (iii) the evaporation of solvent and formation process of the MWNT polygons.

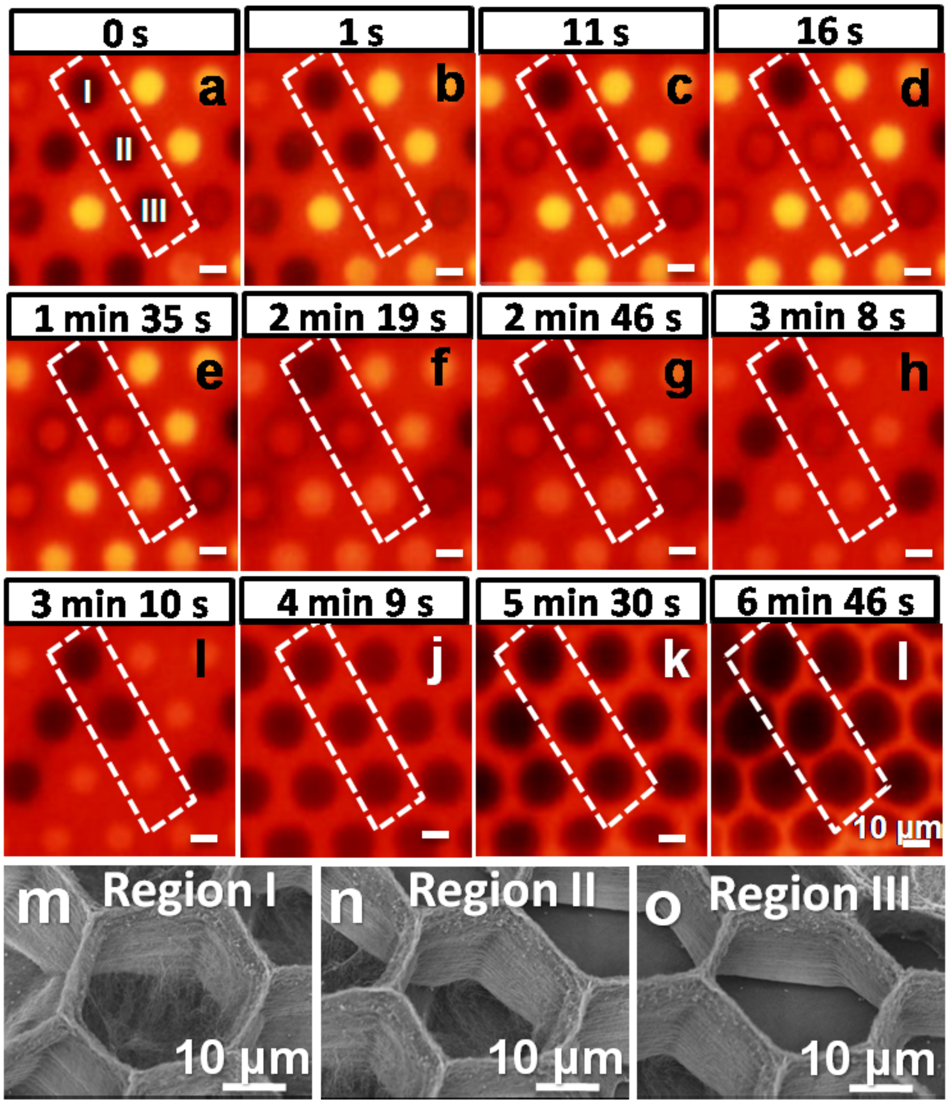

Figure 6.5 (a-l) Real time FM images of the formation process of MWNTs - QDs polygons showing the (a-e) filling; (f-h) saturation; (i-l) evaporation and polygon formation process. The dotted rectanglular boxes were used to mark out the vacancies used for analysis. (m-o) SEM images of MWNTs polygons labelled (I-III) in (a) taken at an angle of 25°.

Due to difference in the duration and the amount of QD mixture that filled the vacancies, the eventual polygons formed from Region I, II and III were expected to differ. With FESEM imaging, polygons formed in Region I, II and III respectively were analyzed. **Figure 6.5m** shows image of Region I, which holds the shortest duration and least amount of QD mixture. As such, while the top portion of the MWNT vacancy developed into a hexagon, loose strands of MWNTs could still be observed brunching out of the semi-packed MWNTs. In addition, unlike those observed in Figure 6.2e, Figure 6.3e and Figure 6.4a no MWNTs were flattened at the base of the polygon. With increased duration and quantity of the QD mixture, no stray MWNTs brunching out from the packed polygon top was observed in Region II (Figure 6.5n). However, MWNTs at the base of the polygon remained un-flattened. Based on Figure 6.5(m,n), a longer period of occupancy of the QDs and increasing the quantity of the QDs mixture to the point of saturation would inevitably result in the formation of well packed MWNT polygons. This expectation was verified in the FESEM image of Region III (Figure 6.5o). Being the only one to achieve saturation, as well as being the first among the three observed regions to be filled with QDs, the MWNT polygons formed had well-defined walls and the base was covered with flattened MWNTs. Hence this finding thus provide a route to the formation of well-defined polygons with different types of bases that could allow possible applications as seeding sites for tissue culture.[15]

6.3 Positive MWNTs Microstructures

Making use of the competition between gravitational and capillary forces, together with controlled amount of water, one could possibly restrict clustering of MWNTs to the surface of the MWNTs. Together with the use of focused laser beam, water assisted top gathering MWNTs pillars could be created.

6.3.1 Technique for the Formation of Positive MWNT Microstructures

With hydrostatic stress being identified as the driving force behind the collapse of MWNTs from regions of lower densities towards that of higher densities,[9] simulated high density regions could be created via close packed MWNT pillars. By maintaining large distances between each cluster of MWNT pillars, empty spaces could be created between each cluster. Consequently, water induced hydrostatic stress would cause the pillars to bend towards each other, thereby creating top gathering MWNTs.

Patterns were crafted out of as-grown MWNTs (Figure 6.7a) using a focused laser beam (Figure 6.7b). The patterned MWNTs were oxidized using reactive ion etching (RIE) and placed inversely onto the surface of distilled water (Figure 6.7c). In doing so, upon removing the sample from the water surface, a minimum volume of water required to wet the MWNTs completely would remain on the MWNT surface (Figure 6.7d). Such control is crucial in ensuring that only the top portion of the MWNTs would experience capillary effect as the water evaporates (with the samples being kept inverted), thereby allowing top gathering of the MWNTs pillars to occur (Figure 6.7e).

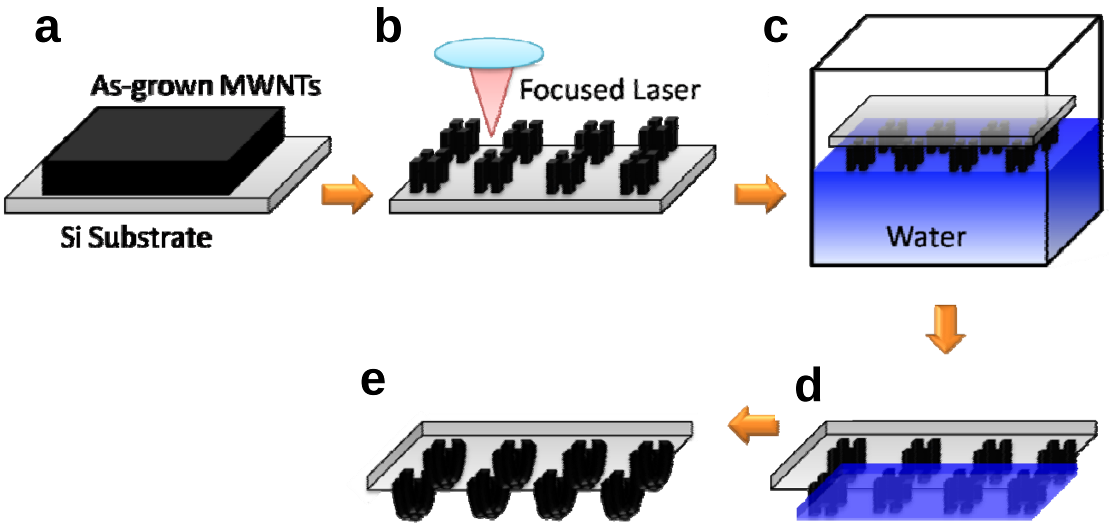

Figure 6.6 Schematic of the procedure to create positive MWNTs microstructures. (a) As-grown MWNT array; (b) creating MWNT pillars using focused laser beam; (c) inverting MWNT pillars over water; (d) keeping the samples inverted while drying and (e) formations of top gathering MWNT pillars.

6.3.2 Water Assisted Assembly of Positive MWNT Microstructures

Based on the above technique, ordered array of MWNTs pillars as illustrated in the insert of Figure 6.7a, were found to collapse in a random manner. However, with pillars created in clusters of four pillars separated by large spacing (Figure 6.7b, insert), the MWNTs were found to gather at the top in an orderly manner. The results shown in Figure 6.7a and Figure 6.7b thus verified the above proposed technique for the formation of top-gathering MWNT pillars. Modifying the positions of the pillars as shown in the insert of Figure 6.7c, the three pillar clusters were observed to gather at the top-portion of the pillars within the clusters. Tilted views (40^o) of the top-gathering MWNT pillars were as shown in Figure 6.7(d,e). From both images, MWNT pillars were observed to gather at the top regions with the base of the MWNT pillars remaining attached to the Si substrate. As such, through creations of both high and low density regions in the MWNTs array, one could easily control the eventual formations of the top-gathering MWNTs.

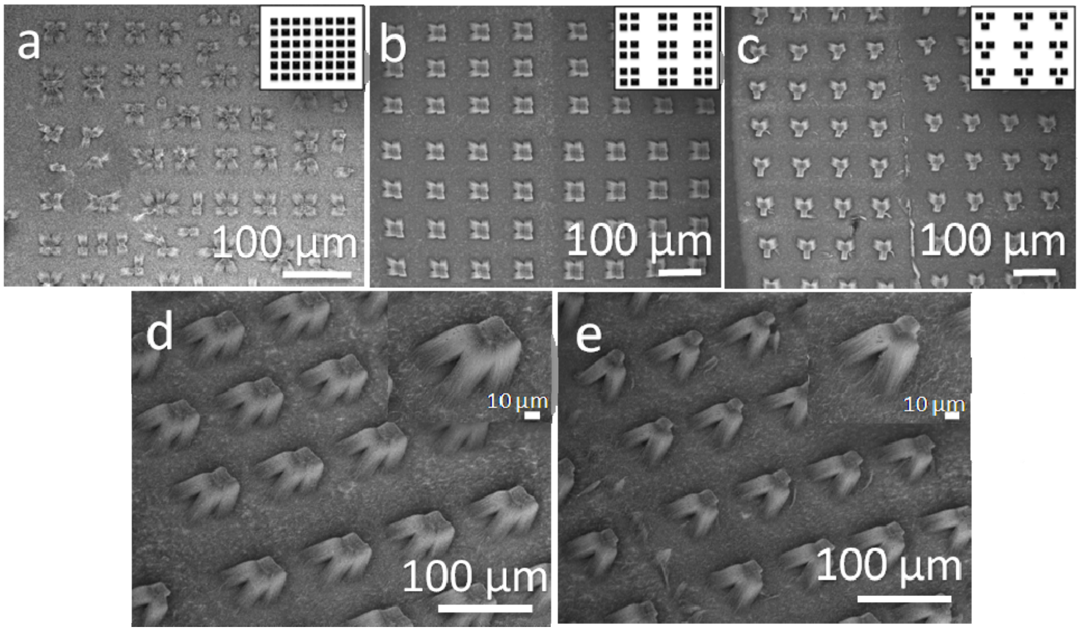

Figure 6.7 SEM images of capillary-assisted (A) randomly collapsed MWNT pillars; ordered top-gathering of (B) four and (C) three MWNT pillars. Inserts (A-C) are schematics showing the respective positions of the MWNT pillars before water assisted assembly. (D-E) SEM images taken at a 40^o tilt of the top-gathering (D) four and (E) three MWNT pillars. Inserts in (D-E) are higher magnifications of the respective clusters of MWNT pillars.

6.3.3 Analysis of Top Gathering MWNT Pillars

For the analysis of the top-gathering MWNTs pillars, a beam sway model, similar to the one proposed by Beguchi *et al.*[16] to calculate the maximum resist deflection in synchrotron radiation lithography, was used. Individual MWNT pillar was treated as a beam supported at one end as shown in Figure 6.8.

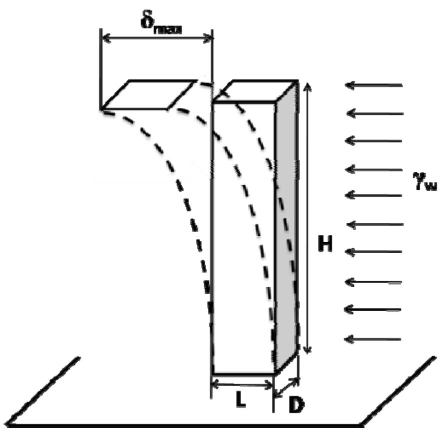

Figure 6.8 Illustration of the beam sway model used in the analysis of the top-gathering MWNT pillars.

In this case, the relation between the Young's modulus and the maximum deflection is expressed by Eq. (6.1):

$$E=\frac{\gamma_w H^4}{8I}\left(\frac{1}{\delta_{max}}\right) \qquad (6.1)$$

where E is the Young's modulus; γ_w is the surface tension of water; H is the pillar height; δ_{max} is maximum deflection and I is the second moment of area expressed by Eq. (6.2):

$$I=\frac{1}{12}DL^3 \qquad (6.2)$$

where L is the width of the pillar and D is the length of the pillar. Substituting Eq. (6.2) into Eq. (6.1), the Young's modulus of the MWNT pillar can be expressed as:

$$E=1.5\ HA^3\left(\frac{\gamma_w}{D}\right)\left(\frac{1}{\delta_{max}}\right) \qquad (6.3)$$

where A is the aspect ratio (H/L). As such, the Young's modulus of the MWNT pillar, E, hence the pillar's flexural stiffness (EI), is proportional to the height, H of the MWNTs as well as the third power of the aspect ratio, A of the MWNT pillar. It is also inversely proportional to the maximum deflection, δ_{max} experienced by the pillar.

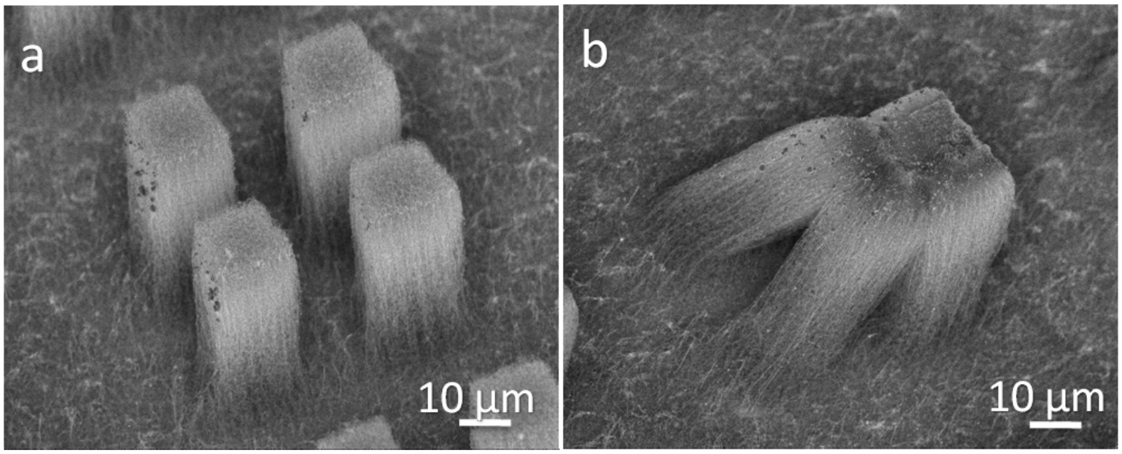

Figure 6.9 SEM images taken at 40^o tilt, showing (a-b) four MWNT pillars (a) before and (b) after water assisted top-gathering.

Considering a cluster of four MWNT pillars as shown in Figure 6.9, with the MWNT pillars gathering at the center of the cluster, the maximum deflection that the pillars could undergo in this configuration was found to be 22.6 μm. Substituting this value into eq. (3), and with the other variables obtained from Figure 6.9, the estimated Young's modulus of the MWNT pillars were found to be ~ 11.9 MPa. With the surface tension (as known as the force per unit length) of water as 72.8 mN/m[9] and the height, H of the MWNTs found to be ~ 20.8 μm, a force of ~ 1.98 μN would be sufficient to bring about such top-gathering effect of the MWNT pillars.

However, it had to be noted that such top-gathering phenomenon of the MWNT pillars could be separated into macro- and micro-scopic view. In the beam sway model proposed, only the macroscopic effects were considered. With MWNT pillars being made up of ~ 4000 individual MWNTs, capillary forces acting on the individual MWNTs as water evaporates from the MWNTs surface also had to be taken into consideration for such a phenomenon to occur.

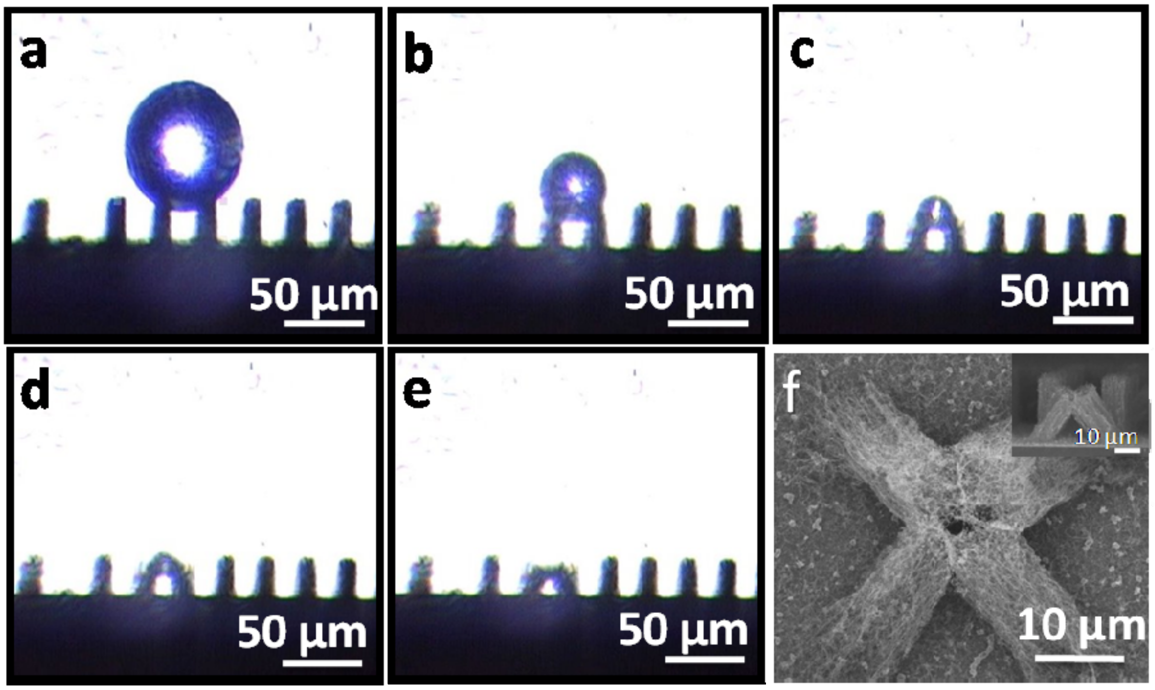

Figure 6.10 (A-E) Optical images of capillarity-assisted top-gathering of MWNT pillars as the water droplet evaporates. (F) SEM image showing the top view of the gathered pillars. (Insert of (F) is the side view of the same set of top-gathering pillars)

In situ observations of such capillary induced top-gathering MWNT pillars could be observed using a side-view optical microscope. As shown in the series of snap shots (Figure 6.10(a-e)) as the water droplet which lands on two MWNT pillars evaporates, MWNT pillars were found to gather at the top. SEM images of the gathered MWNT pillars taken from top view showed that capillary forces resulting from the evaporation of a water droplet with volume ~ 0.21 pl is sufficient to induce a deflection of MWNT pillar with dimension 9.2 μm (L) x 9.2 μm (D) x 24.1 μm (H), over a distance of 14.7 μm.

6.4 Large Scale Collapsing of MWNT Walls by Dip-Dry Method

In addition to the ability to create both positive and negative structures into desired configurations and at specific positions, large scale MWNT walls could be collapsed via a dip-dry method.

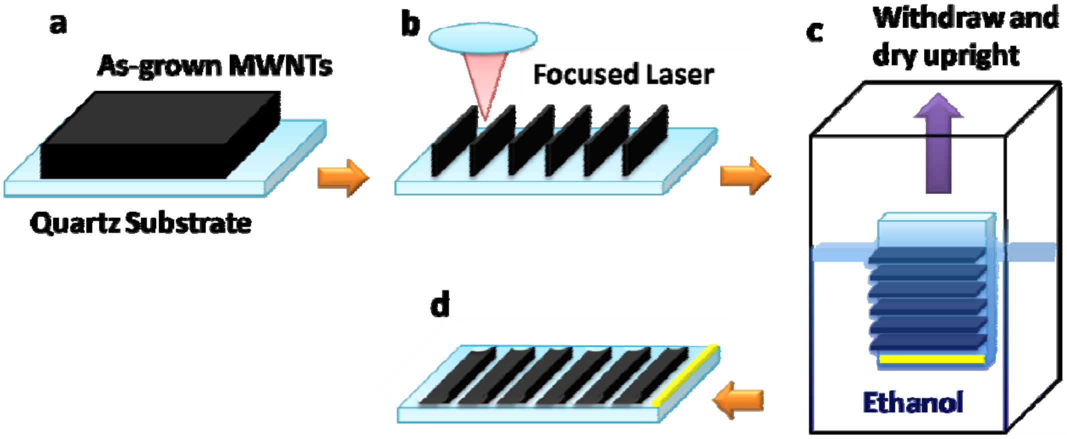

Figure 6.11 Schematic of the dip-dry method used in collapsing large scale MWNT micro-walls. (A) As-grown MWNT arrays; (B) focused laser beam was used to create MWNT micro-walls; (C) the patterned MWNTs sample was placed into a container of ethanol and withdrawn vertically; and (D) the MWNT micro-walls collapsed into MWNT micro-belts. The yellow bar indicates the direction in which the sample was removed from the ethanol.

To do so, MWNT walls were crafted out of as-grown MWNTs on quartz via a focused laser beam as shown in Figure 6.11(a,b). The laser pruned MWNTs were then submerged into a small amount of ethanol reservoir and pulled vertically out of the wetting agent as illustrated in Figure 6.11c. The extracted MWNT samples were left to dry vertically and the eventual outcome comprises collapsed MWNT belts as shown in Figure 6.11d.

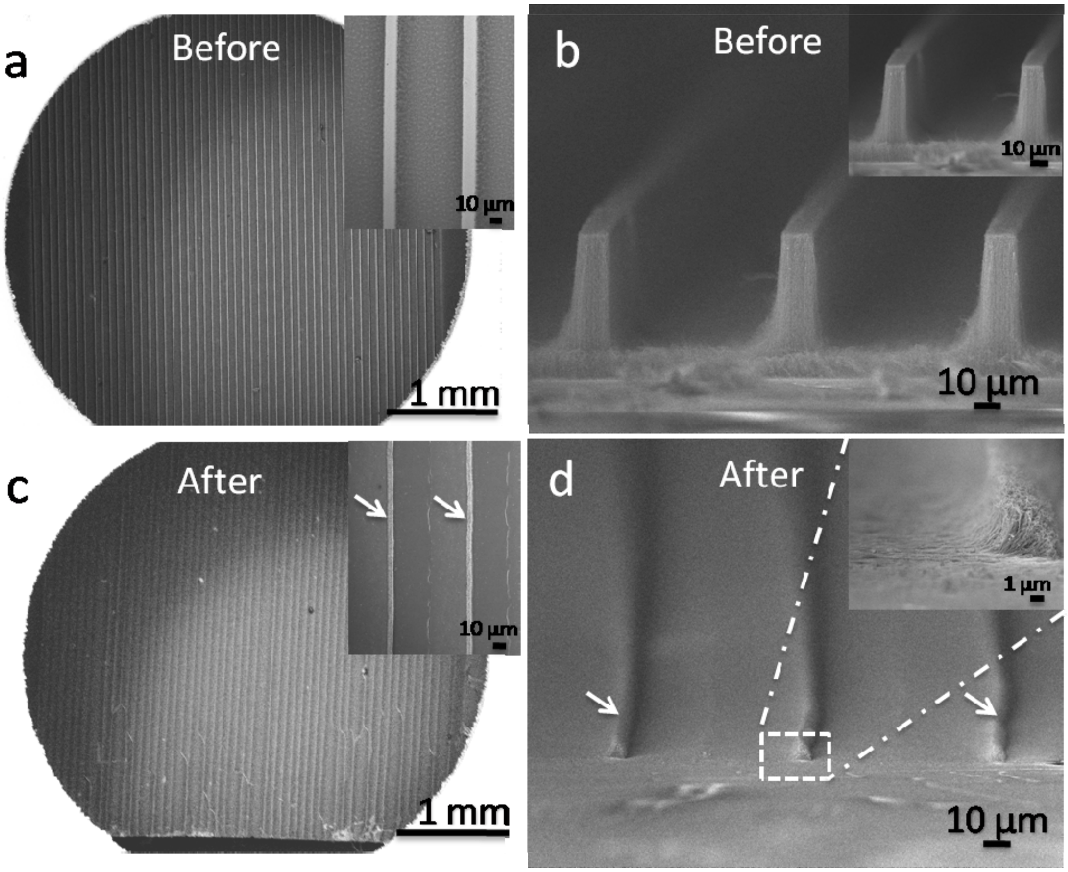

Figure 6.12 SEM images showing both (A, C) top and (B, D) side view (tilted at 40^o) before and after being collapsed via the dip-dry method. Inserts (A-C) are higher magnifications of the walls before and after collapsing. Insert in (D) is a higher magnification of the top region of the walls enclosed within the dotted rectangle box after collapsing. The white arrows indicate the top regions of the belts.

MWNT walls as long as 4 mm with a channel width of 10 µm were pruned as shown in both Figure 6.12a and its insert. The cross-sectional views of the walls were as shown in Figure 6.12b. After going through the dip-dry method, the walls were found to collapse in an orderly manner, thereby allowing MWNTs to be aligned in a parallel manner to the direction in which the walls were collapsed. While majority of the MWNT belts were packed down on the quartz substrate, the top portion of the channel remained relatively less compact. These loosely packed channel tops could be seen in both Figure 6.12(c,d) as indicated by the white arrows. Insert of Figure 6.12d showed a higher magnified view of one of these loosely packed channel tops with a well packed down channel body.

6.4.1 Proposed Mechanism of Collapsed MWNT Walls

Possible formation mechanism of the packed-down MWNT walls could be as follows: (1) As the quartz substrates with the MWNT walls were withdrawn vertically from the ethanol reservoir, as ultrathin ethanol film was formed over and on the MWNT channels.[17] (2) Leaving the substrate to dry vertically, under the unidirectional gravitational force, the downward dewetting ethanol film exerts a hydrodynamic drag force onto the MWNT channels. (3) This hydrodynamic drag force would be further complimented via the presence of downward surface tension from the receding line of the ethanol film.[18] (4) Once the receding ethanol film moved beyond the base of the MWNT channels, the MWNTs would be pinned to the quartz substrate, hence upon full retreat of the ethanol thin film, the MWNT belts would be completely packed-down to the substrates. (5) However, with the MWNT walls comprising many intertwined MWNTs, air pockets would inevitably be pushed from the base of the walls to the top of the MWNT walls as the ethanol thin film retreats. (6) With the receding ethanol solvent, before the air bubbles could be removed from the MWNTs, the film would have travelled past the air packed MWNTs. Thereby, leaving the top regions of the MWNT belts loosely packed.

While the majority of the MWNT belts collapsed unidirectional, MWNT belts near the edge of the substrate were twisted 180^o (Figure 6.12c). Such twisting phenomenon of the belts could be due to difference in receding rates of the ethanol thin film over the channels, since; the surface tension effect would differ between the center portion and the edges of the substrate.

6.4.2 I-V Measurements of Collapsed of MWNT Walls

With high densities of aligned nanotube arrays preferred for applications in interconnects and sensors,[19-21] in addition to controlling the initial density of the MWNT arrays during the growth process, the process of collapsing the MWNT walls also allowed densification of the MWNT arrays as the MWNTs became well-packed to the substrate surfaces. In addition, the ability to flatten the MWNT walls horizontally onto the substrates also opened up possibilities of creating suspended and stretched nanotubes that could be implemented for nanoscale electro-mechanical sensing components.[11]

To illustrate the feasibility of using this approach for electrical applications, current-voltage (I-V) measurements of the MWNT walls, before and after collapsing, were conducted (Figure 6.13). Figure 6.13(a,c) are optical images of the MWNT walls before and after collapsing. As the MWNTs were grown on quartz, the IV-measurements of the laser pruned walls were expected to reflect that of individual MWNT walls. Two probe electrical measurements were carried out along the whole length of the MWNT walls. The sample was placed onto the CascadeTM Microtech micro-probe station where electrical contacts were made using two probe tips (tip diameter: 2.4 μm) situated at each end of individual MWNT walls as illustrated by the schematic in Figure 6.13(b,d). 20 individual strands of MWNT walls before and after collapsing were used for the I-V measurements and the average of these values were plotted in Figure 6.13e. The average total resistance of the MWNT walls was ~ 70 kΩ, whereas that of the MWNT belts was ~ 20 kΩ. Thus by simply undergoing the dip-dry method of packing the MWNTs to the substrate, an approximately 3.5 fold reduction in resistivity and corresponding 3.5 fold improvement in current measured from the MWNT belts were achieved.

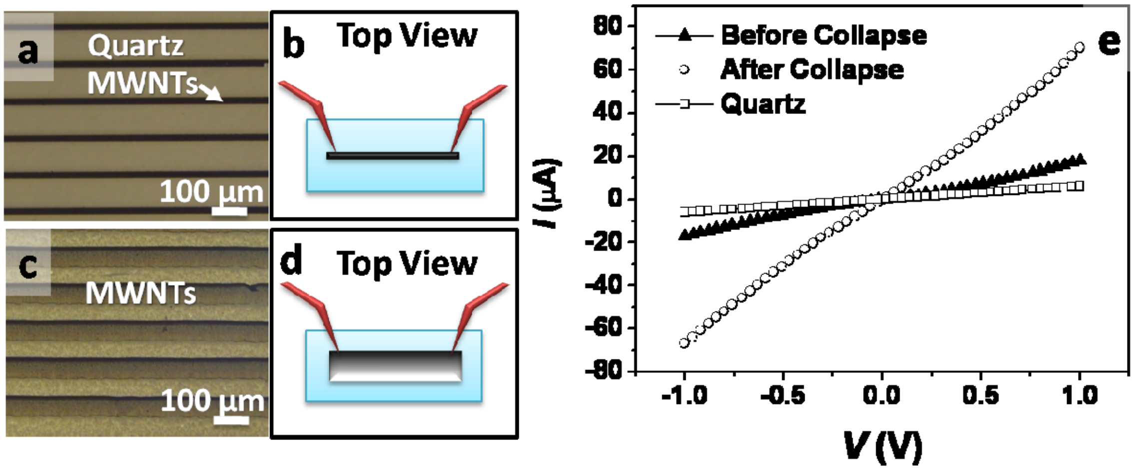

Figure 6.13 (a) I-V measurements of the MWNT walls before and after being collapsed using the dip-dry method. (b,d) Optical images of the walls (b) before and (d) after collapsing; (c,e) Schematic showing the respective positions of the probe tips on individual MWNT walls (c) before and (e) after collapsing.

In addition to the I-V measurements conducted across fully collapsed MWNT belts, similar measurements were also conducted at different positions of the MWNT belts. These include measurements along the length of the MWNTs that made up the walls, across twisted MWNT belts that were found near the edges of the samples and across belts that had collapsed together. For these measurements, 5 to 6 sets of readings were taken for each point of measurements and the average values were obtained. The average values of the I-V measurements plotted in Figure 6.14a were obtained from position B, C and D as shown in the corresponding optical images in Figure 6.14(b-d).

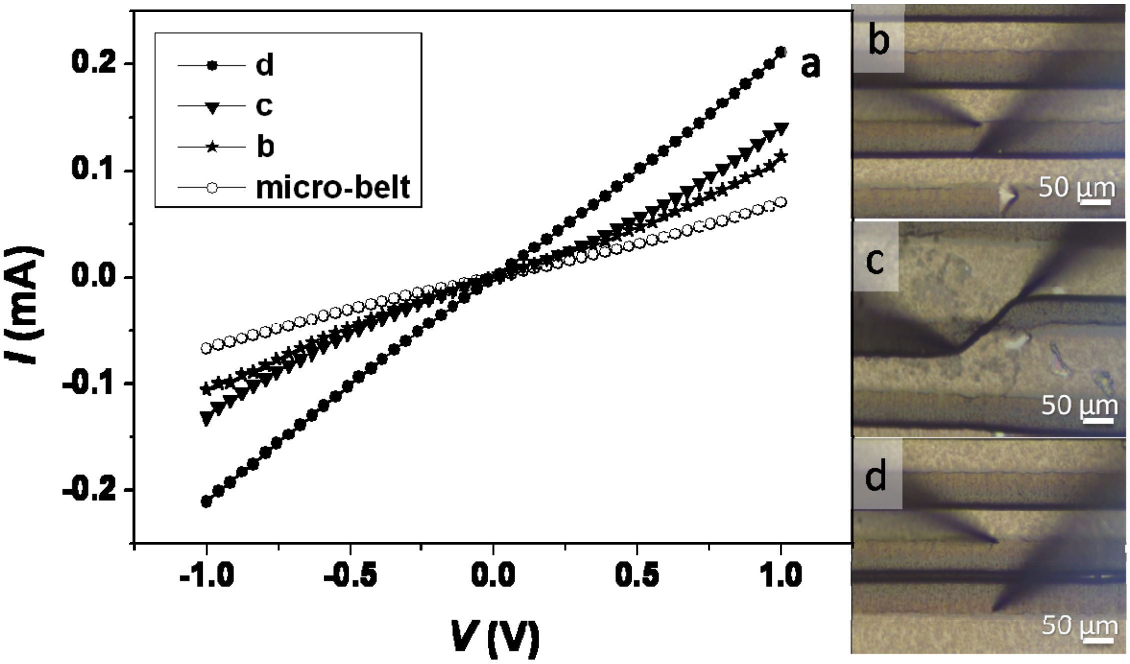

Figure 6.14 (A) I-V measurements of the MWNT walls before and after being collapsed using the dip-dry method. (B, D) Optical images of the walls (B) before and (D) after collapsing; (C, E) Schematic showing the respective positions of the probe tips on individual MWNT wall (C) before and (E) after collapsing.

From the I-V measurements plotted in Figure 6.14a, by simply changing the position of the two probe tips from across the length of the collapsed wall to along the length of the MWNTs that made up the wall (Figure 6.14b), the resistance changed from ~ 20 kΩ to ~ 11 kΩ. Moving the two probes to take measurements across the twisted MWNT channel, a resistance of ~ 5 kΩ was detected. Similar resistance (~ 5 kΩ) was obtained when two probe tips were placed across two MWNT walls that had collapsed towards each other.

Based on above experiments, by simply twisting the MWNT walls by 180^o, a reduction in resistance by as much as 14 times, as compared to the MWNT walls before collapsing, could be achieved. Thus to achieve greater control over the twisting effect of the MWNT walls, laser pruning was used to patterned the MWNT array into the wavy structure shown in Figure 6.15(a,c). The joint between parallel walls from 45^o (Figure 6.15a) to that of 90^o (Figure 6.15c). Similar ethanol assisted assembly as that shown in Figure 6.11 was carried out on the samples. The resultant assembled MWNT walls were as shown in the optical images in Figure 6.15(b,d). Comparing the regions boxed out in Figure 6.15(b,d), different types of twisting to the MWNT walls could be observed by simply changing the angle at which the walls were joined. From both Figure 6.15b and Figure 6.15d, the MWNT walls were twisted at an angle similar to that pre-determined by the laser pruned structures. As such, it could be verified that through laser pruning and using the dip-dry method of assembling MWNT walls, the degree at which the MWNT walls were twisted could be varied. In turn, the resistance of the packed-downed MWNT walls could be controlled.

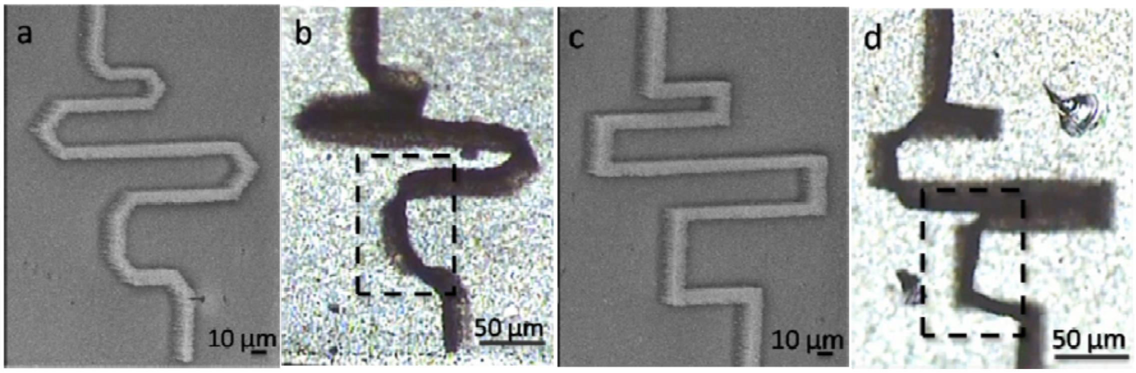

Figure 6.15 (a,c) SEM images of different curve structures created via laser pruning on MWNT arrays. (b,d) Ethanol assisted assembly of twisted MWNT walls. The dotted rectangle box outlined similar regions on both structures except for the angle at which the parrallel MWNT walls were joint.

6.5 Conclusion

In conclusion, three different capillarity assisted assemblies of both positive and negative MWNT microstructures were presented. Using the first method of introducing artificial vacancies, laser power, densities of MWNTs and oxidation process dependencies for the creation of negative MWNT microstructures were investigated. With the results showing that via the use of different laser power, the polygon “walls” were observed to shift from the vertical bisector between two adjacent artificial vacancies. Proposed ideal density of well formed MWNTs polygons was determined to be between 0.95 x 10^9 MWNT cm^{-2} and 2.04 x 10^9 MWNT cm^{-2} and the importance of the sequence in which the MWNT samples were oxidized was presented. Positive microstructures made up of top gathering MWNT pillars were created and 0.21 pl of water was found to produce sufficient force to bring about 14.7 µm deflections of a (9.19 x 9.19 x 24.1) μm^3 pillar. Lastly, using a dip-dry method, densification of large scale MWNT micro-walls were achieved as the micro-walls became well-packed to the surface of the substrates, thereby forming MWNT micro-belts. Consequently, improved resistivity of the MWNT micro-belts by 3.5 fold after densification was achieved. In addition, through forming different types of collapsed MWNT strips, the resistance of the MWNT strips could be controlled. The techniques thus provided a viable route for the creation of large scale of highly packed aligned MWNTs for implementation in nanoscale electronic devices.

Reference

(1) Nishikawa, T. Nishida, J. Ookura, R. Nishimura, S. I. Wada, S.; Karino, T.; Shimomura, M., Mesoscopic patterning of cell adhesive substrates as novel biofunctional interfaces. **1999,** *10*, 141.

(2) Shimoda, H. Oh, S. J. Geng, H. Z. Walker, R. J. Zhang, X. B. McNeil, L. E. Zhou, O. *Adv. Mater.* **2002,** *14*, 899.

(3) Wildoer, J. W. G. Venema, L. C. Rinzler, A. G. Smalley, R. E. Dekker, C. *Nature* **1998,** *391* , 59.

(4) Treacy, M. M. J. Ebbesen, T. W. Gibson, J. M. *Nature* **1996,** *381*, 678.

(5) Jang, J. W. Lee, D. K. Lee, C. E. Lee, T. J. Lee, C. J. Noh, S. J. *Solid State Communications* **2002,** *122*, 619.

(6) Tekleab, D. Czerw, R. Carroll, D. L. Ajayan, P. M. *Appl. Phys. Lett.* **2000,** *76*, 3594.

(7) Baughman, R. H.; Zakhidov, A. A. de Heer, W. A. *Science* **2002,** *297*, 787.

(8) Chakrapani, N. Wei, B. Q. Carrillo, A. Ajayan, P. M. Kane, R. S. *PNAS* **2004,** *101*, 4009.

(9) Liu, H. Li, S. H. Zhai, J. Li, H. J. Zheng, Q. S. Jiang, L. Zhu, D. B. *Angewandte Chemie-International Edition* **2004,** *43*, 1146.

(10) Wei, B. Q. Vajtai, R. Jung, Y. Ward, J. Zhang, R. Ramanath, G. Ajayan, P. M. *Nature* **2002,** *416*, 495.

(11) Lee, B. Y. Heo, K. Bak, J. H. Cho, S. U. Moon, S. Park, Y. D. Hong, S. *Nano Letters* **2008,** *8*, 4483.

(12) Li, P. H. Lim, X. D. Zhu, Y. W. Yu, T. Ong, C. K. Shen, Z. X. Wee, A. T. S. Sow, C. H. *J. Phys. Chem. B* **2007,** *111*, 1672.

(13) Li, Q. W. DePaula, R. Zhang, X. F. Zheng, L. X. Arendt, P. N. Mueller, F. M. Zhu, Y. T. Tu, Y. *Nanotechnology* **2006,** *17* , 4533.

(14) Liu, H. Zhai, J. Jiang, L. *Soft Matter* **2006,** *2* (10), 811-821.

Correa-Duarte, M. A. Wagner, N. Rojas-Chapana, J. Morsczeck, C. Thie, M. Giersig, M. *Nano Letters* **2004,** *4*, 2233.

(15) Deguchi, K. Miyoshi, K. Ishii, T. Matsuda, T. *Japanese Journal of Applied Physics Part 1-Regular Papers Short Notes & Review Papers* **1992,** *31*, 2954.

(16) Darhuber, A. A. Troian, S. M. Davis, J. M. Miller, S. M. Wagner, S. *J. Appl. Phys.* **2000,** *88*, 5119.

(17) Hong, S. W. Jeong, W. Ko, H. Kessler, M. R. Tsukruk, V. V. Lin, Z. Q. *Adv. Funct. Mater.* **2008,** *18*, 2114.

(18) Nihei, M. Kawabata, A. Kondo, D. Horibe, M. Sato, S. Awano, Y. *Japanese Journal of Applied Physics Part 1-Regular Papers Short Notes & Review Papers* **2005,** *44*, 1626.

(19) Kreupl, F. Graham, A. P. Duesberg, G. S. Steinhogl, W. Liebau, M. Unger, E. Honlein, W. *Carbon Nanotubes in Interconnect Applications*, Vaals, Netherlands, **2002**, 399.

(20) Kaur, S. Sahoo, S. Ajayan, P. Kane, R. S. *Adv. Mater.* **2007,** *19*, 2984.

Chapter 7: Improving Hydrophobicity via Micro-patterning

7.1 Introduction

In this chapter, a combination of top-down and bottom-up approaches in the investigation of the wettability of aligned multi-walled carbon nanotubes (MWNTs) with micro-patterns was conducted. In particular, we studied the hydrophobic nature of patterned MWNT array comprising parallel arrays of micro-walls. To do so, both the channel width (A) between the micro-walls and structure width (B) of the micro-walls were varied and the respective contact angles were measured. Parallel arrays of micro-walls made out of aligned array of MWNTs were created via a laser pruning technique[1]. The laser pruning technique involved the use of an optical lens to focus a laser beam into a spot of diameter ~ 5 µm. By fixing the position of the laser spot while moving the MWNT sample, parallel arrays of micro-walls were pruned or burned out of the MWNT arrays due to the intense heat produced by the focused laser beam. The height of these micro-walls is 10 – 30 µm while the widths of the micro-walls are 7, 13 or 21 µm. The channel width, wall-to-wall distance, between the micro-walls was varied at a A/B width ratio of 2 to 6. The contact angle was measured after patterning. The average size of the water droplets used was 100

± 30 μm. From the results obtained, the hydrophobic nature of the sample was much improved whenever water droplets landed on one micro-wall of 7 μm in width. However, when a droplet bridges across two micro-walls, the surface became less hydrophobic. Thus to ensure that the water droplets mostly landed on one micro-wall, an optimal super-hydrophobic MWNT surface corresponded to parallel array of micro-walls with a width of 13 μm and a channel width of ~ 50 μm. Such findings could possibly serve as value-add for further developments in the creation of water repelling patterned MWNTs surfaces.

7.2 Creation of MWNT Micro-walls

A laser pruning system as mentioned in the previous section was used to create parallel arrays of micro-walls from vertically aligned MWNTs (Figure 7.1a).[1] The channels were cut using laser power of 50 mW and at a velocity of 150 μms^{-1}. Figure 7.1 (b-d) show examples of parallel arrays of micro-walls with widths of (b) 7 μm, (c) 13 μm and (d) 21 μm respectively created using the laser pruning system as seen under the FESEM. In the course of investigation, systematic studies on the effect of micro-walls on the hydrophobicity of the MWNTs were conducted by varying the ratio of the width of the channel width (A) to the width of the micro-walls (B), as well as the width of the micro-walls, B, as indicated in Figure 7.1c.

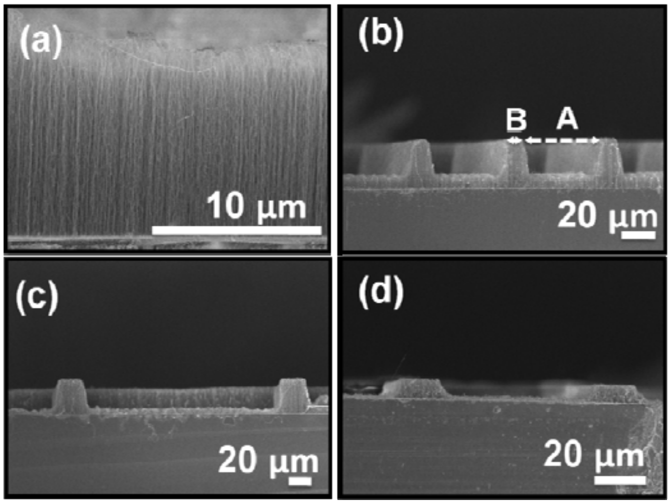

Figure 7.1. (a-d) FESEM image of (a) un-patterned MWNTs; parallel arrays of (b) 7 µm, (c) 13 µm and (d) 21 µm MWNT micro-walls created using the laser pruning technique.

7.3 Effect of Micro-patterning on the Hydrophobicity of MWNTs

Wetting of a solid surface usually involves three different interfacial boundary surfaces, namely, solid – air (free solid), solid – liquid and liquid – air (free liquid) interface. With each interface having its own specific energy content, wetting with its accompanying change in the extent of each interface will result in variations to the net specific energy content of the system. As a water droplet spreads, both wetted area under the droplet and the free liquid surface over it would thereby increase. The former releases energy while the latter consumes energy. Difference in these energies would be the one that determines the wetting characteristics of the solid.[5] When a water droplet lands on the MWNT surface, due to the MWNT surface having a higher surface energy, the droplet would tend to maintain a near spherical shape on the MWNTs. Water droplets landing on un-patterned MWNTs (Figure 7.2a) and 1 micro-wall (Figure 7.2b) has only 1 point of contact, whereas water droplets landing on 2 micro-walls (Figure 7.2c) have two contact points. The contact angle of water droplets landing on 1 micro-wall can be observed to be greater than that of un-patterned MWNTs.

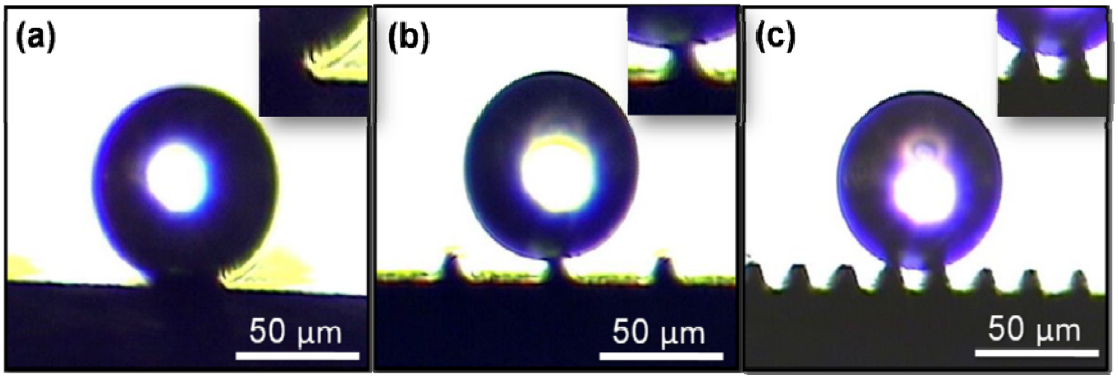

Figure 7.2. Cross sectional view showing point of contact between a water droplet and (a) an un-patterned MWNT surface; (b) 1 micro-wall and (c) 2 micro-walls. Inserts are higher magnification of the contact point between the water droplet and the micro-wall(s).

Figure 7.3 (a-c) shows the measured mean CA of water droplets landed on 1 micro-wall or across 2 micro-walls, on different patterned MWNTs. The horizontal axis in these graphs corresponds to the A/B ratio for these samples. The widths of the micro-walls were 7 µm, 13 µm and 21 µm. For comparison, the measured upper and lower limits for the CA of water droplets landed on un-patterned MWNTs are shown in Figure 7.3. The graphs show that for the same structure width, the largest CA was obtained when the droplet lands on 1 micro-wall. The CA decreased when the droplet landed across 2 micro-walls. In Figure 7.3a, the CA for water droplet landing on 1 micro-wall was at least 10% greater than that for 2 micro-walls. Furthermore, with the exception of micro-walls with width of 21 µm, the CA of water droplets landing on 1 micro-wall, with width of 7 and 13 µm, was higher than the CA of water droplets landing on un-patterned MWNTs.

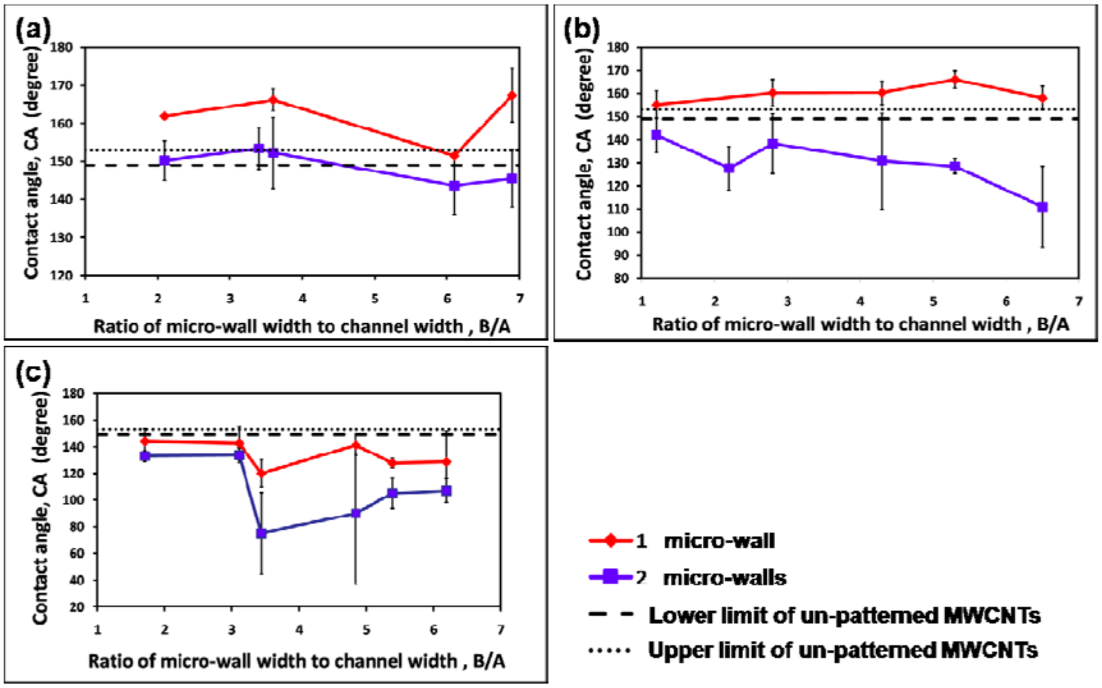

Figure 7.3. Comparison of mean contact angle with the water droplets landed on different number of micro-walls on different patterned MWNTs arrays. The widths of the micro-walls are (a) 7 µm; (b) 13 µm and (c) 21 µm. The dotted lines represent upper and lower limits of the error in the contact angle of un-patterned MWNT array.

As such, with reference to Figure 7.4, when a water droplet lands on 2 micro-walls, the water droplet would try to maintain a spherical shape about both points. However, an attempt of the droplet to bridge across both structures causes the water droplet to deviate from a spherical shape, resulting in a reduced contact angle (Figure 7.3) as compared to that of un-patterned MWNTs or droplets landing on 1 micro-wall. To determine the value of the CA for water droplets landing on un-patterned and 1 micro-wall, a tangential line from the contact point between the droplet and the surface of the MWNTs was drawn as shown in Figure 7.4a and Figure 7.4b. For the case of water droplet landing on 2 micro-walls, a horizontal line connecting the 2 micro-walls that the droplet landed on was drawn in addition to the tangential line as shown in Figure 7.4c. The CA was determined to be the internal angle from the tangent to the MWNTs surface/horizontal line between the two micro-walls.

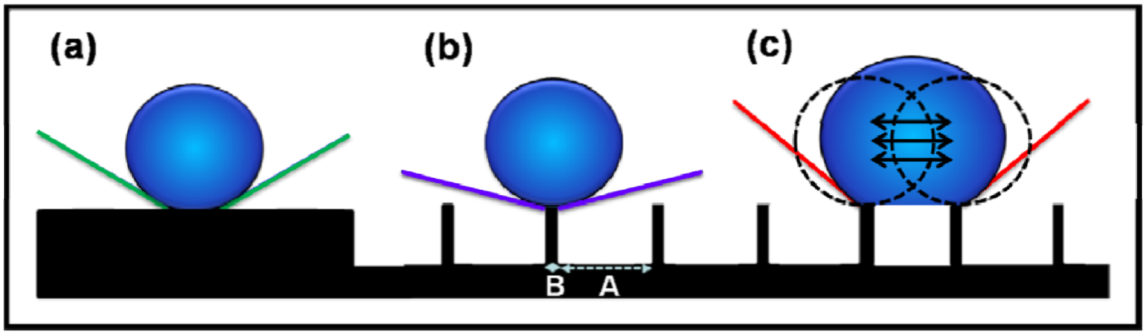

Figure 7.4. Schematic showing CA of a water droplet landing on (a) un-patterned MWNTs, (b) 1 micro-wall and (c) 2 micro-walls. (c) Shows possible distortions in the shape of the water droplet when it lands across 2 micro-walls as the droplet seeks to maintain a spherical shape over both micro-walls.

As the water droplet that was supported by 2 micro-walls undergoes evaporation, distortion to the shape of the droplet could be observed (Figure 7.5). Such phenomenon was similar to that observed from water droplets evaporating from surfaces of lotus leaves as reported by Cheng *et al.* [6], where the adhesive nature of the water droplet causes it to maintain the same base area while reduction in droplet volume occurred in the form of a decrease in the contact angle. Such an observation is consistent with that shown in Figure 7.5 (a-b) where a reduction in the measured CA, from 108.8^{o} to 87.4^{o} was observed as the water droplet evaporated. Furthermore the sudden decrease in CA agreed with the ellipsoidal cap model for evaporation that was proposed for water evaporation on a poly-methylmethacrylate polymer by Erbil and Meric [7].

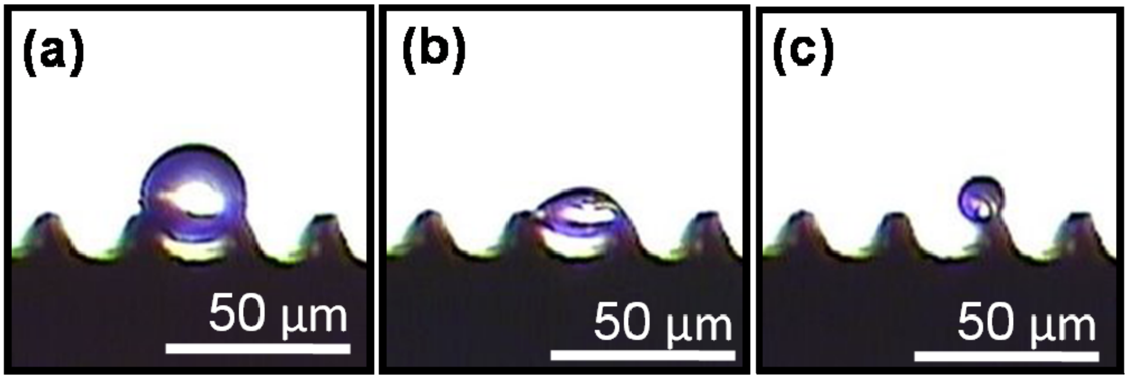

Figure 7.5. Cross sectional view showing variations in CA as water droplet stretching across 2 micro-walls undergoes evaporation. (a) Water droplet just landing on 2 micro-walls; (b) distortion to the shape of water droplet and hence CA as the droplet evaporates and (c) the same water droplet 'jumping' over to 1 micro-wall.

In addition to what was previously observed for the evaporation of water droplet from super-hydrophobic surfaces of lotus leaves, water droplets were found to possess the ability to 'jump' from 2 micro-walls onto 1 micro-wall as shown in Figure 7.5b and Figure 7.5c. The 'jumping' of the water droplet results in a spike in contact angle from 87.4° to 124.8°. In other words, such a phenomenon of water droplet 'jumping' from 2 micro-walls to 1 micro-wall would cause a percentage increase of 42.9% in the CA measured. This was attributed to surface tension effect over powering adhesive forces between the CNTs and the water droplet.

7.4 The Optimal Micro-wall Width when the Water Droplet Lands on 1 Micro-wall.

From the results presented in Figure 7.3, a higher CA was obtained when the water droplet lands on 1 micro-wall. Hence, systematic studies of the CA of the droplets landing on 1 micro-wall of different widths were carried out. Figure 7.6 showed the effect of variations in width of micro-wall on the CA of water droplets of similar sizes landing on 1 micro-wall. When the width of the micro-wall (Figure 7.6 (b-c)) was less than the contact length of un-patterned MWNT surface (Figure 7.6a), the contact spatial extent would be smaller. A higher contact angle was achieved, as there was less interaction between the surface and water molecules. If the width of the micro-wall (Figure 7.6d) was similar to/greater than the typical contact spatial extent for un-patterned MWNTs, the CA would be similar to or lesser than that of a droplet landing on an un-patterned MWNT surface considering standard deviation.

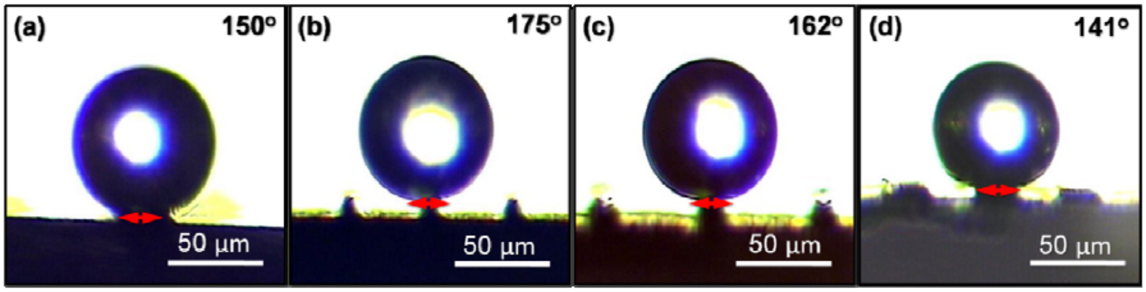

Figure 7.6. Water droplets of similar volume landing on (a) Un-patterned sample, micro-wall of widths (b) 7µm, (c) 13µm and (d) 21µm. The double headed arrow shown in (a), (b), (c) and (d) indicates the contact length for un-patterned surface. The measured CAs are shown in upper right corner of each image.

To verify the proposed explanation for the results shown in Figure 7.6, CA of water droplets of similar volume with different area of contact with the MWNTs were compared. To change the area of contact, micro-walls of different width (7, 13 and 21 µm) were pruned. As shown in Figure 7.7, the CA was largest when the water droplet landed on 1 micro-wall with a width of 7 µm. When a water droplet of a particular size landed on the surface of un-patterned MWNTs, it occupied a point of contact with diameter x. Given a water droplet of similar volume, reduction in the area on which it could land on, would cause the water droplet to behave like a perfect drop with a CA of value 180^{o}. Whereas, an increased in the area of contact, would stretch the droplet and lead to a reduction in CA measured as shown in the CA of water droplet measured on 13 and 21 μm micro-walls (Figure 7.7).

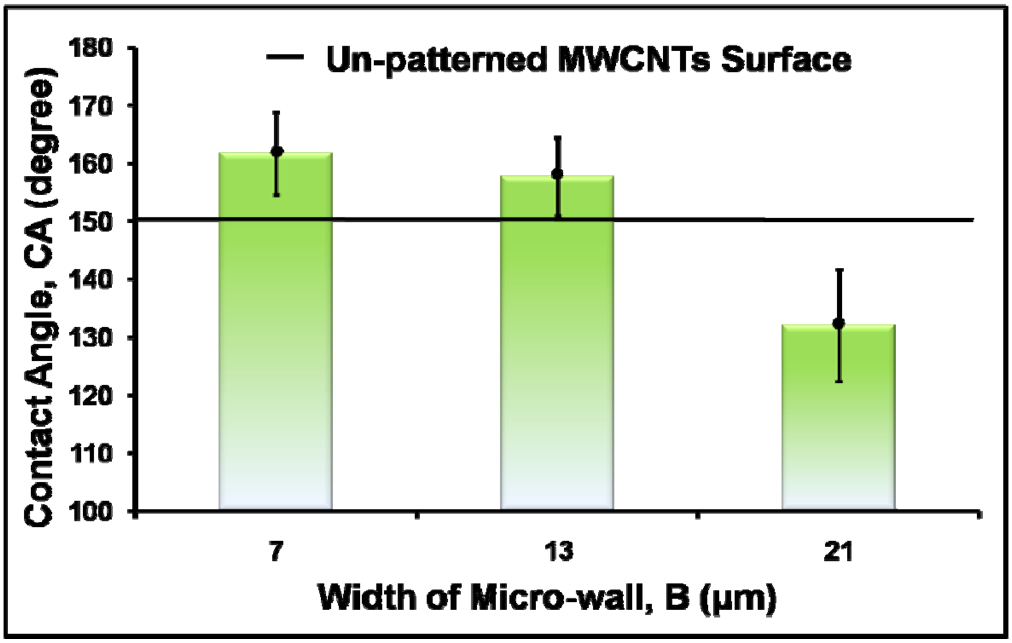

Figure 7.7. Comparison of contact angle when the droplet lands on 1 micro-wall for different dimensions. The horizontal line indicates the CA of un-patterned MWNTs.

7.5 Probability of Water Droplet Landing on 1 Micro-wall.

The effectiveness of the patterned MWNTs as a hydrophobic surface depended on both the CA of the water droplet and the probability of water droplet landing on 1 micro-wall, where the CA was greatest. Figure 7.8 showed that the percentage of water droplet landing on 1 micro-wall varies with the size of the channel width of the MWNTs sample for water droplets with average diameter of 100 ± 30 µm used in the experiments. This percentage was obtained through calculating the number of water droplet that landed on 1 micro-wall as a percentage over the total number of water droplets landing on 1 micro-wall, across 2 micro-walls or in between micro-walls. Even though the CA for MWNTs samples with micro-walls of width 7 µm was higher than micro-walls with a wdith of 13 µm, the probability of water droplet landing on 1 micro-wall was much lower. Therefore, we found that the most effective MWNT sample had a channel width of ~50 µm and 13 µm micro-wall with ~70% probability for a water droplet to land on 1 micro-wall. Micro-walls with width of 21 µm were not included in this study since the measured CA for this sample was lower than the un-patterned MWNTs.

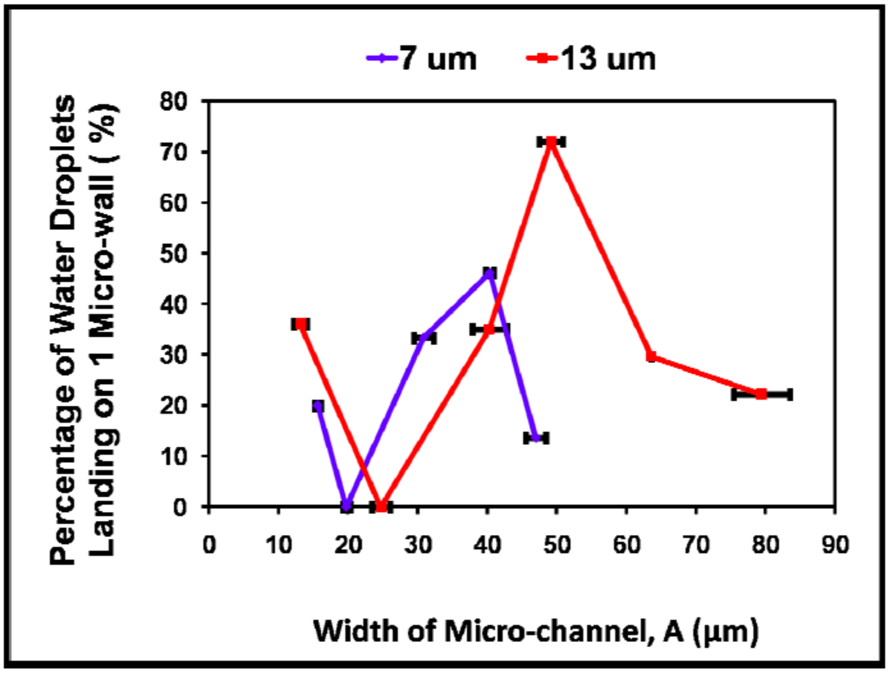

Figure 7.8. Percentage of water droplets landing on 1 micro-wall with respect to the width of the micro-wall, B.

Using the values obtained, the optimal S_f value, ratio of width of micro-walls to distance between them, was found to be ~ 0.26. This S_f value was greater than those proposed by Bhushan *et al.*[8] The difference could be attributed to several reasons. Firstly, MWNTs possessing intrinsic hydrophobic properties were used in our experiments as compared to PF_3 coated single-crystal Si. Secondly, the micro-walls created on the MWNTs were in the form of micro-ridges instead of cylindrical pillars created by Bhushan *et al.* Thirdly, the strands of interlacing MWNTs protruding out of both micro-walls and the channels created in our experiments provided additional roughness at the nanoscale as compared to flat surfaces on both asperities and valleys studied by Bhushan. Such combined effect of nano- and micro-scaled roughness on the hydrophobicity of surfaces were also reported by Zhang *et al.*[9] Due to the difference in the nature of materials used, the critical value proposed based on our study using MWNTs, could possibly serve as value-add for further developments in the creation of MWNT based water repelling surfaces and aquatic devices.

7.6 Conclusion

In conclusion, through micro-patterning of MWNTs, the hydrophobicity of the MWNTs could be increased. The MWNTs were found to become more hydrophobic when a water droplet landed on 1 micro-wall with a width of 7 μm. However, when a droplet bridged across two micro-walls, the surface became less hydrophobic. Thus to ensure that the water droplets mostly landed on one micro-wall, the most optimal super-hydrophobic MWNTs surface corresponded to parallel array of micro-walls with a width of 13 μm and a channel width of ~ 50 μm.

References

(1) Lim, K. Y.; Sow, C. H.; Lin, J. Y.; Cheong, F. C.; Shen, Z. X.; Thong, J. T. L.; Chin, K. C.; Wee, A. T. S. *Adv. Mater.* **2003,** 15.

(2) Zhu, Y. W.; Cheong, F. C.; Yu, T.; Xu, X. J.; Lim, C. T.; Thong, J. T. L.; Shen, Z. X.; Ong, C. K.; Liu, Y. J.; Wee, A. T. S.; Sow, C. H. *Carbon* **2005,** 43.

(3) Wang, Y. H.; Lin, J.; Huan, C. H. A.; Chen, G. S. *Appl. Phys. Lett.* **2001,** 79.

(4) Bell, M. S.; Teo, K. B. K.; Lacerda, R. G.; Milne, W. I.; Hash, D. B.; Meyyappan, M. *Pure and Applied Chemistry* **2006,** 78.

(5) Wenzel, R. N. *Ind. Eng. Chem.* **1936,** 28.

(6) Cheng, Y. T.; Rodak, D. E. *Appl. Phys. Lett.* **2005,** 86.

(7) Erbil, H. Y.; Meric, R. A. *J. Phys. Chem. B* **1997,** 101.

(8) Bhushan, B.; Nosonovsky, M.; Jung, Y. C. *Journal of the Royal Society Interface* **2007,** 4.

(9) Zhang, L.; Resasco, D. E. *Langmuir* **2009,** 25.

Chapter 8: Conclusion

We had set out to develop a technique that allows low temperature transfer of vertically aligned MWNTs onto a variety of flexible substrates. These transferred MWNTs were found to have cleaner surfaces with better alignment. They also exhibit good electrical contact between the MWNTs and the substrate, and had better field emission properties. A maximal current density of ~10^4 Acm^{-2} has been achieved from the CNT interconnects prepared with this technique. Because of the lower density and open-ended structures, improved field emission performance has been obtained from CNTs transferred on polymers, based on which flexible emitter devices can be fabricated. In addition, the surface of transferred CNTs becomes more hydrophilic, with an averaged contact angle of $93.4 \pm 5.8^\circ$, in contrast to the super-hydrophobic as-grown CNT surface (contact angle $151.6 \pm 5.5^\circ$). With versatile properties and flexible applications, the technique provides a simple and cost-effective way towards future nanodevices based on CNTs.

Substrates from which the initial batches of MWNTs were transferred from, were sent for another round of synthesis. These 2nd generations of MWNTs were also discovered to display ~ 2.6 times improvement in field enhancement factor and more uniform emission. Such significant improvements are attributed to new emission sites comprising sharp carbonaceous impurities, made up of both iron and silicon oxide, encompassing both tip and upper portion of the 2nd generation of MWNTs. This technique of re-growth MWNTs thus presents a viable route for the production of MWNTs with better field emission quality.

Using the transfer technique, studies on the effect of hydrostatic dilation stress to the formation of MWNT microstructures were investigated. By using PDMS to prevent solvents from being in contact with hydrophilic substrates and to imbibe into the MWNTs to miminise any bending of the MWNTs, no MWNT polygons were formed even with the introduction of artifical vacancies as initiators. With the presence of hydrostatic dilation stress as an important element in which the formation process of the MWNT polygons, three different capillarity assisted techniques, large scale formations of MWNT based micro-structures were created. Firstly, laser induced artificial vacancies in MWNT arrays served as initiation sites during water-driven formation of MWNT polygons network. The dependence of the structures formed on the size of the vacancies, the densities of the MWNTs and the surface properties of the MWNTs arrays were investigated. Secondly, organized MWNT pillars were crafted out of MWNT arrays and a small droplet of water was found to produce sufficient force to bring about deflections of the pillars towards each other, thereby allowing the formations of three-dimensional top-gathering MWNTs pillars. Lastly, a dip-dry method was introduced for large scale orienting and densification of MWNT micro-walls into micro-belts along the substrate. A 3.5 fold reduction in resistivity of the MWNT micro-walls was achieved. These techniques can serve as flexible and viable routes for the creations of large scale, highly packed aligned MWNTs for implementation in nanoscale electronic devices

Lastly, hydrophobicity of the MWNTs was improved through the creations of parallel array of micro-walls via a laser pruning technique. Changes to the hydrophobic nature of the patterned MWCNTs due to artificially induced roughness through variations in both the widths of the walls and the distance between adjacent walls, channel width, were investigated. The sample became more hydrophobic whenever water droplets landed on one micro-walls of 7 μm or 13 μm in widths. However, when a droplet bridges across two micro-walls, the surface became less hydrophobic. Optimal super-hydrophobic MWCNTs surface corresponded to parallel array of micro-walls with a width of 13 μm and a channel width of ~ 50 μm. Such findings could possibly serve as value-add for further developments in the creation of water repelling CNTs surfaces via micro-patterning.